Computational Models and Damper Concepts for Vibration Reduction of Turbomachinery Blisks

by

Andrea Lupini

A dissertation submitted in partial fulfillment
of the requirements for the degree of
Doctor of Philosophy
(Mechanical Engineering)
in The University of Michigan
2020

Doctoral Committee:

Professor Bogdan Epureanu, Chair
Professor Gregory Hulbert
Professor Nickolas Vlahopoulos
Professor Kon-Well Wang

Andrea Lupini

alupini@umich.edu

ORCID iD: 0000-0002-8293-2295

DEDICATION

To mom and dad

ACKNOWLEDGMENTS

It did indeed take a village to get to this moment. As I write these words, I realize that the impact of the community surrounding me cannot be easily contained in these few lines. Nonetheless, I want to spend a few words to express my gratitude and thank at least those who supported me in the journey leading up to this thesis.

First, I would like to express my gratitude to my advisor, Professor Bogdan Epureanu, for making this thesis possible and for providing invaluable guidance through the highs and lows of the research process. I also want to thank my committee members, Professor Gregory Hulbert, Professor Nickolas Vlahopoulos and Professor Kon-Well Wang, for gracefully accepting to serve on my doctoral committee and providing valuable suggestions and feedback to improve my research. The results presented in this work could not have been obtained if it weren't for the agencies that funded this research effort, so I would like to thank the U.S. Navy and the GUIde 5 Consortium for their generous support.

I also want to thank all the colleagues in the *Applied Nonlinear Dynamics of Multi-Scale Systems Lab* for always being there for me in various roles, as mentors, friends, and peers. Special thanks go to Dr. Mainak Mitra, for providing help and guidance as I transitioned between projects, and for all the fun (and sometimes relevant) discussions about nonlinear dynamics and blisks vibration. I also want to thank Sarah Callan and Justin Shim for the help they provided with the experimental set-up. Some of the results in this thesis would have not been possible without their help.

Even though not actively involved in this dissertation, I would like to thank Professor

Philip Cha, Professor Gianni Nicoletto, and Professor Patrick Little, for supporting me in my decision to pursue a doctorate degree. They truly have been mentors to me.

I would like to thank all my friends, near and far. From Italy to California, in person or via text, I have felt their love all along the way. Special thanks go to my Ann Arbor family, who made my time here truly special. I am extremely grateful to have such amazing friends.

Finally, I would like to thank my family. Mamma, Papà, Simone, and Fernanda, who are always there for me, who believe in me more than I do, and who always encourage me to aspire and strive for more. I owe all my accomplishments to them.

PREFACE

It is my hope that my twenty-four readers will forgive me if I burden them with additional text to read before the thesis is even started. However, for this thesis to be most fruitful to them, I deemed it worth it to spend a few words on the thesis origin and organization.

This thesis could be conveniently separated in two parts, one about reduced-order-modeling of bladed disks, and another one about the vibration reduction of such systems. Even though the results and topics covered in the two parts are from projects that differ in nature, they do tackle the same issues that plague turbomachinery components. While the first part focuses on tools to be used to achieve improvements in the design phase, the second part focuses on additional tools and devices that can be used to mitigate excessive vibrations once the blisk design is established. As a result, each chapter is written with the aim of being self-contained, similar to a standalone research article, containing abstract, introduction and conclusion. Thus, the reader interested in a specific topic may prefer to move directly to the chapter of interest, skipping the other ones. While the introductory material in each chapter could be somewhat redundant throughout the thesis, it will guarantee the best reader experience. Enjoy!

TABLE OF CONTENTS

LIST OF FIGURES

Figure

ABSTRACT

Integrally bladed rotors (IBRs), also known as blisks, are important turbomachinery components at the core of gas turbine engines. In operating conditions, IBRs must withstand large centrifugal forces, high temperatures, and blade vibrations caused by upstream flow perturbations. The combination of the cyclic symmetric design of blisks and their inherent mistuning, i.e. small deviations from the nominal properties and geometry, makes them prone to vibration localization, that can lead to vibration amplification of some of the blades in the system. Unlike traditional bladed disk assemblies, in which blades are connected to the disk portion using frictional joints, blisks are manufactured in one piece. The lack of frictional interfaces in blisks results in lower damping, which in turn causes even larger vibration amplitudes. The concurrent presence of high steady stresses and vibration, combined with the large numbers of cycles that blisks blades must withstand, can lead to blade failure due to high cycle fatigue. As a result, the study and reduction of blisk vibrations is of paramount importance to ensure the safety and reliability of such components. The study of blisk vibration is currently carried out using reduced order models (ROMs), due to the prohibitive computational cost associated with the repeated solution of large size finite element models. Vibration reduction is commonly pursued using ring dampers, which typically present low effectiveness.

A two-fold approach is used in this work to tackle the complex problem of vibration characterization and mitigation in IBRs. First, a set of efficient ROM tools is introduced to be used in the design phase. Then, novel damping mechanisms are proposed for vibration reduction in operating conditions.

A conditioning technique for projection-based ROMs is presented together with examples of applications. Due to the need to model the effects of repairs (blends) or geometric changes during design iterations, models often require the use of distinct meshes for the same component. A novel method is thus developed to overcome computational issues caused by the use of multiple meshes in ROMs for mistuned blisks. Both methods preserve the accuracy of the ROM and at the same time reduce the overall computational cost. In addition to this, a method is presented to efficiently capture the effects of prestress in geometrically mistuned blisks. Different cases and blend types are examined to prove the generality of the approach, showing excellent agreement with the full order model.

The last three chapters are entirely dedicated to novel ring dampers concepts, in which the core idea behind tuned vibration absorbers is leveraged to substantially increase damper effectiveness. This allows for higher levels of energy dissipation by frictional nonlinearities, making it possible for the damper to reduce vibrations even when placed in a region with little blisk-alone motion. First, a preliminary computational study is introduced to prove the validity of the concept. Then, a test rig is presented to experimentally demonstrate the effectiveness of the concept. Finally, a novel damper design is presented and studied using state-of-the-art computational tools.

CHAPTER 1

Introduction

In this chapter, an overview of the topics covered in this thesis is presented. After introducing the overarching motivation behind this work, a review of state-of-the-art literature is carried out to provide the reader with the necessary background and expose the literature gaps that will be addressed. Finally, the objectives of the thesis are presented.

1.1 Motivation

Integrally bladed rotors (IBRs), also known as blisks, are structures commonly used in gas turbine engines, and more generally in turbomachinery, due to improvements in performance and reduction in the number of components that they provide compared to traditional rotors [1]. The components number reduction is due to the fact that IBRs are manufactured in one piece, unlike traditional turbomachinery rotors, where the disk and blade portions are assembled via fir-tree or dovetail joints. IBRs are nominally cyclic symmetric, i.e. the full system can be obtained by repetition of a basis substructure around the symmetry axis [2, 3]. However, due to manufacturing tolerances, wear, and damages, the symmetry of the nominal structure is broken in real IBRs. Any deviation from nominal conditions is called mistuning. Unlike traditional rotors, in which blades can be easily replaced when damaged, IBRs need to be either repaired or replaced entirely. This poses a challenge for the maintenance of such

systems, as it is not economically feasible to replace the entire IBR, whose manufacturing is lengthy and costly. For this reason, repairs called blends are typically carried out to prevent the propagation of existing damages, e.g. cracks. The blending process consists of material removal in the damaged area to prevent crack propagation, thus avoiding potential component failure. In fact, turbomachinery components typically operate in very demanding operating conditions. The blades must withstand large static and dynamic stresses, due to centrifugal forces and aerodynamic loads caused by upstream flow perturbations, which can vary depending on the operating conditions. The presence of flow forcing is particularly dangerous because the combination of the cyclic symmetric design of blisks and their inherent mistuning makes them prone to vibration localization, which results in the amplification of blade vibration for some of the blades in the system [4, 5]. Furthermore, blisks present very low damping due to the absence of frictional contacts and joints, that are instead typically present in standard disks with inserted blades [3, 4]. This can result in large vibration amplitude in one or more blades, which combined with the high levels of stress that the material has to withstand can lead to high cycle fatigue and ultimately blade failure.

For this reason, it is extremely important to study the vibration characteristics of blisks taking into account the effects of mistuning, the presence of repairs, and the various operating conditions. This also includes the study of vibration damping mechanisms applied to blisks.

1.2 Background

The presence of mistuning, i.e. any deviation from nominal properties or geometry, in turbomachinery blisks is known to cause vibration amplification of some of the blades in the assembly [3, 4, 6]. As a result, high cycle fatigue (HCF) is a major concern for such structures [7], and a great deal of effort has been spent investigating blisk vibrations. Over the past decades, the increase in computational capabilities has led to an increased use of

simulation in design. The simplistic lumped mass models initially used to understand the overall dynamics of the system have been mostly replaced by large high-fidelity finite element (FE) models [3, 4]. The cyclic symmetry of blisks can be exploited to significantly reduce the computational cost associated with structural and vibrational analysis [2, 3], since a single sector, with appropriate boundary conditions, can be used to carry out the analysis in lieu of the full system. This technique, however, is unable to capture the presence of mistuning, which is known to significantly alter the dynamic behavior of bladed disks with its symmetry breaking effects. Thus, only full wheel analyses, i.e. involving a model that includes all sectors, can capture the mistuned response when using traditional FE models. To make things worse, due to the stochastic nature of mistuning, probabilistic analyses are required to evaluate the possible behavior of a blisk. It is not uncommon for some of these models to have millions of degrees of freedom (DOFs) per sector, which makes the solution of multiple forced response problems intractable using FE model. Due to the prohibitive size of full order FE models, the use of reduced order models (ROMs) is now very common in structural dynamics [8–13]. This is due to the need for faster but at the same time reliable and accurate models to predict the behavior of complex systems in a timely fashion. Several techniques have been developed over the years, both general and problem-specific.

Among the most common reduction techniques one can recall proper orthogonal decomposition [14], balanced truncation [15], balanced proper orthogonal decomposition [16], and Kyrilov subspace-based techniques [17]. Good overviews of some of the methods currently used can be found in [15, 18–20]. Several studies have been conducted over the years on the dynamical behavior of such ROMs, with a particular focus on the stability of the reduced order system [19, 21–23]. For example, when different sets of projection vectors are used, as it is commonly done in parametric ROMs, the projection vectors can potentially span the same subspace [20, 24, 25]. For this reason, conditioning is important, and several solutions have been proposed. In [9, 24–27], conditioning is applied to the transformation matrix

before projection, to make sure that the projection vectors are linearly independent. Such methods require manipulation of full size matrices and vectors, thus they are not computationally efficient. Several techniques have been proposed to alleviate this issue, e.g. rank-one update [28], and some approaches have been successfully applied to ROMs in the context of dynamic model reduction [29]. Other techniques have been developed to work directly in the ROM space, but they mainly focus on the stability of the system under the assumption of well-conditioned projection matrices. In [22], a Petrov-Galerkin projection method is considered, and a convex optimization problem is solved to modify the left reduced-order basis (ROB) and enforce system's stability. This is done implicitly, i.e. not operating directly on the ROB but on the ROM. One of the goals of the thesis is to tackle these numerical issues in a more numerically efficient way.

Researchers have extensively studied in the past the effects of mistuning on the dynamics of blisks using ROMs, focusing in particular on geometric mistuning [9, 11, 13]. An interesting type of geometric mistuning is the use of blends, i.e. repairs applied to damaged sectors via material removal, for the repair of cracked or damaged blisks. Such repairs need to be carefully designed so that they have minimal impact on the vibration of the original blisks. For this reason, ROMs have been created for the analysis and optimization of such repairs. The Mode-Accelerated X-Xr (MAX) method presented in [10] is particularly adapt to model such effects, and able to include the more common stiffness mistuning using component mode mistuning (CMM) [30]. However, among all the techniques that have been proposed for the study of the structural dynamics of geometrically mistuned blisks [8–13], only a few studies focus on the issues that may arise when using multiple meshes. When geometric changes are large, as is the case in the presence of blends, advanced mesh morphing techniques can be used to ensure that the FE model accurately represents the blended geometry and maintains mesh quality (e.g., it does not result in coarsely represented surfaces). Several studies involving mesh morphing can be found in turbomachinery [31–34]. The morphing process

must be carried out for each geometrically mistuned blade in the assembly, resulting in a system that potentially has as many different sector meshes as the number of sectors. When it comes to cyclic symmetric structures, such as the ones found in turbomachinery, many challenges arise, such as mode clocking, interface compatibility, and projection errors. The issue of mode clocking is discussed in detail in [9], where a solution to deal with small geometric mistuning is proposed. However, the small mistuning assumption does not hold for large blends. In that case, not only the clocking might affect the results, but also the mesh compatibility at the (disk) interface between sectors. This compatibility can be expressed as a set of constraints on node pairs requiring them to experience the same motion [12]. This becomes a significant challenge especially when acceleration modes are used, like in the case of the MAX method [10]. Thus, it is not efficient to use the methods presented in [9, 12]. A new method will be introduced in this thesis.

In addition to mesh morphing, other aspects must be considered, such as the fact that geometric mistuning can present a significant interaction with centrifugal loading and other sources of prestress. Turbomachinery components typically operate in very demanding conditions, and the operating condition at which the system is excited has a significant impact on the response. For example, rotational effects as well as aeroelastic effects have been shown to have an important role on the vibration characteristics of the system [5, 35–38]. The thermo-mechanical aspects of the problem could also be taken into account, as they are relevant to the product life cycle [39]. The introduction of centrifugal effects, a typical source of prestress, can be easily accommodated in ROMs. In [40, 41] the general problem of cyclic rotating structures is tackled using cyclic symmetry together with component modes synthesis [42]. Some of the effects arising when mistuning is combined with the effects of rotation are investigated in [43–45]. In [43] the effects of mistuning are studied using a set of basis vectors that adequately spans the interface motion between sectors. This method ensures the compatibility condition at the interface, but it also requires an extra set of modes

to be computed, which can be cumbersome. The method is extended to a range of variable rotation speeds using parametric techniques. In [44, 45] a study on cracks and coriolis effects in rotating disks is presented, without dealing with the compatibility condition at the interface that is of interest here. In [46] a study on the effect of prestress can be found, focusing in particular on the presence of contact forces, but without dealing with geometric mistuning. Results on the study of mutual influence between Coriolis forces and blade mistuning are also available [35], but no attention is given to how to treat noncyclic prestress. When it comes to model order reduction, another such solution is to use parametric ROMs [47], which are known to be effective. However, many parametric ROMs are not particularly efficient because they require the calculation of multiple sets of modes, and because of possible numerical instabilities of the transformation matrix [20, 47]. The effects of rotational speed can be captured as variations in the stiffness matrix, as suggested by previous studies for the blade part only [36]. The inefficiencies and deficiencies of current methods in the modeling and calculation of noncyclic prestress are tackled in this thesis.

The study and modeling of blisk vibration through the use of ROMs, as presented in this chapter, is a necessary step for the identification of potentially damaging resonances. Complementary to that is the reduction of vibration amplitude through the use of effective damping mechanisms. Several damping solutions have been employed in the past, among which we can recall the use of coatings [48, 49], order-tuned vibration absorbers [50] and impulse mistuning [51]. Another common approach is to use frictional nonlinearities to dissipate energy [52]. Examples include under-platform dampers [53–55], ring dampers [56, 57], and shrouds [26, 58], which add nonlinear damping to the system by means of frictional contacts. Great efforts have been made to design and study ring dampers [56, 57, 59, 59–64]. However, the effectiveness that ring dampers provide can be limited because they rely on the relative motion present between a damper and its groove, which can be very small when blade to disk coupling is low [62], or in blade dominated modes. The same concept can be

found in applications to gears [65–67], even in that case with low effectiveness [65]. Since their effectiveness is limited and only specific modes can be targeted, studies in the past have focused their interest in low frequency and low nodal diameters regions [59–61], because of the fact that higher frequencies and ND would typically present small disk motion, and thus little energy dissipation. One of the challenges associated with friction dampers is to ensure damper effectiveness across multiple operation regimes and frequency ranges. A concept that has been exploited in the past for the suppression of vibrations in civil and mechanical structures is the one of tuned vibration absorber [68–70].Several studies have been carried out in order to extend the concept to multiple tuned mass dampers [71] and multi-DOF systems [72]. This concept does not rely on nonlinearities, and does not require large motion at the attachment location in order for it to be effective. The effectiveness of this concept is based on energy transfer and frequency split that is achieved through tuning. The natural frequency split shifts the resonance of the host structure away from the area of interest, resulting in lower amplitude response. Turbomachinery blisks are subject to narrow band excitations with specific spatial patterns known as traveling-wave excitations [73]. This type of excitation makes tuned mass dampers (TMDs), or tuned vibration absorbers (TVAs), good candidates for vibration reduction in such structures. Several studies have been carried out in the past on TMDs in applications ranging from space structures [74] to missile launchers [75]. A general overview can also be found in [76]. Some studies focused on the use of Coulomb friction as a method to dissipate the energy that is transferred to the TMD [77, 78], and most of these studies have been carried out only computationally [77]. However, due to modeling challenges such as those in contact modeling, experimental validation is necessary. The study presented by Hartung et al. [78] introduced an experimental setup for the investigation of TMDs with contacts. The experiment is designed to replicate a 2-DOF lumped mass model, as the elasticity in the system only comes from connecting springs. That study, however, does not capture the effects of the position of the TMD in realistic 3D assemblies or the role

that geometry and mode shapes could play in the effectiveness of such TMD. In this thesis, several studies will be presented on a novel ring damper concept based on the concept of friction-enhanced TMD.

1.3 Objectives

The first goal of this thesis is to address the potential numerical issues in ROMs introduced in [9, 24–27]. In Chapter 2, a conditioning technique for projection-based ROMs for structural dynamics is presented. Due to the nature of such systems, only Galerkin methods are discussed, i.e. methods in which the left and the right transformation matrices are the same. However, the approach can be extended to Petrov-Galerkin ROMs as well, with only few changes to the proposed algorithms. The numerical issues potentially arising from the use of a nearly singular transformation matrix are examined, and a robust solution based on the ROM mass matrix is proposed.

Since only a few studies focus on the issues that may arise when using multiple meshes in ROMs for blisks structural dynamics, the topic is explored in Chapter 3. Issues such as mode clocking, interface compatibility, and projection errors are examined, and an efficient method able to tackle both interface compatibility and clocking issues for the calculation of pristine morphed normal modes is proposed.

Chapter 4 covers the efficient calculation of prestress effects in ROMs for geometrically mistuned blisks, focusing in particular on the method presented in [10]. None of the studies found in literature focus on the efficient extraction of the prestressed matrices for a mistuned system. In this section, the focus is set on the creation of a method that can be used in the creation of ROMs in all those cases where prestress can substantially interact with mistuning.

The second part of the dissertation is about novel damping mechanisms for IBRs. In Chapter 5 a novel damper concept that combines the working principles of vibration ab-

sorbers and ring dampers to overcome the limitations of traditional ring dampers is presented. A computational study is carried out to analyze and assess damper effectiveness.

Chapter 6 has two main goals. The first goal is to experimentally and computationally assess the effectiveness of the proposed friction-enhanced TMD concept using a simple test rig. The second goal is to experimentally validate a simulation tool based on the harmonic balance method that is currently used to model nonlinear vibrations in the presence of friction. The proposed setup is a simplified representation of a TMD hosted on the disk region, far away from the blade tip, where only small motions are present. The experimental results are used to validate the predictive ability of a high-fidelity finite-element model used in combination with a harmonic balance solver.

Finally, a realistic damper design based on the findings from the previous chapters is introduced in Chapter 7. The aim of this chapter is to further expand the understanding of novel damping mechanisms for blisks, focusing in particular on realistic ring damper designs based on the TVA concept. The blisk model used in this study was provided by The Ohio State University (OSU) Gas Turbine Laboratory (GTL). A damper based on the design presented herein is scheduled to be tested as a part of a study on mistuning and damping [79].

Part I

CHAPTER 2

A Conditioning Technique for Projection-Based Reduced Order Models

In this chapter, the numerical issues potentially arising from the use of a nearly singular transformation matrix are examined, and a robust solution based on the ROM mass matrix is proposed. The proposed conditioning approach can be viewed as an implicit manipulation of both the right and the left ROB. The manipulation is implicit because it is carried out on the ROM itself, without prior knowledge of the transformation matrix required. Since the proposed approach works after projection, it is referred to as *post-conditioning*. An insight into the physical meaning of the approach is presented, to highlight why the technique preserves the maximum amount of information included in the original transformation without sacrificing numerical stability and accuracy. The method is first tested on a simple system. Then, a more complex case of a ROM for an bladed disk (blisk) is presented to demonstrate how this strategy is versatile and applicable to a wide range of problems of various complexities.

2.1 Introduction

The use of reduced order models (ROMs) is now very common in structural dynamics. This is due to the need for faster but at the same time reliable and accurate models to predict the behavior of complex systems in a timely fashion. Several techniques have been developed over the years, both general and problem-specific. Among the most common reduction techniques one can recall proper orthogonal decomposition [14], balanced truncation [15], balanced proper orthogonal decomposition [16], and Kyrilov subspace-based techniques [17]. Good overviews of some of the methods currently used can be found in [15, 18–20]. Several studies have been conducted over the years on the dynamical behavior of such ROMs, with a particular focus on the stability of the reduced order system [19, 21–23]. It is worth mentioning that ROMs built using a Galerkin method are in general able to preserve the system stability for well-conditioned bases and positive definite matrices [23]. However, bases are not always well-conditioned from a numerical standpoint. For example, when different sets of projection vectors are used, as it is commonly done in parametric ROMs, the projection vectors can potentially span the same subspace [20, 24, 25]. A theoretically well-conditioned transformation matrix can become numerically ill-conditioned when its vectors are nearly linearly dependent. As it will be shown in the following sections, this can produce erroneous results in the ROM. For this reason, conditioning is important, and several solutions have been proposed.

In [9, 24–27], conditioning is applied to the transformation matrix before projection, to make sure that the projection vectors are linearly independent. This is typically done using a singular value decomposition (SVD) of the transformation matrix. The conditioned transformation matrix is obtained selecting a subset of left singular vectors corresponding to the largest singular values. In this paper such an approach is referred to as *pre-conditioning*. Such methods require manipulation of full size matrices and vectors, thus they are not

computationally efficient. Furthermore, such approaches are particularly cumbersome in applications such as parametric ROMs or adaptive ROMs, where the projection vectors can change as the system parameters or forcing changes, requiring multiple conditioning steps. Moreover, due to the large size of the problem, performing SVD might become cumbersome. Hence, several techniques have been proposed to alleviate this issue, e.g. rank-one update [28], and some approaches have been successfully applied to ROMs in the context of dynamic model reduction [29].

Other techniques have been developed to work directly in the ROM space, but they mainly focus on the stability of the system under the assumption of well-conditioned projection matrices. In [22], a Petrov-Galerking projection method is considered, and a convex optimization problem is solved to modify the left reduced-order basis (ROB) and enforce system's stability. This is done implicitly, i.e. not operating directly on the ROB but on the ROM, as it is done in this paper. Another strategy found in literature is to enforce stability by reassigning the unstable eigenvalues of the system through a black-box post-processing algorithm acting on the ROM [21]. The minimization of the objective function requires knowledge of the system response obtained from the full order model, that may not be available. Due to the need for a full order result for every case, the computational burden associated with this strategy is high when multiple ROMs must be created.

A significant effort can be found in mathematical literature to solve the general issue of numerically ill-conditioned problems. Examples can be found in papers involving the general case of solving ill-posed linear equations [80], or generalized eigenvalue problems [81, 82]. The use of such techniques is not recommended nor required here, due to the fact that the matrices involved in the ROM lack some of the fundamental properties of the original full order matrices like positive (semi)definiteness, and thus would produce inaccurate results.

In this paper, the focus is on projection-based ROMs for structural dynamics. Due to the nature of such systems, only Galerkin methods are discussed, i.e. methods in which the left

and the right transformation matrices are the same. However, the approach can be extended to Petrov-Galerkin ROMs as well, with only few changes to the proposed algorithms.

2.2 Background

In this section, the procedures carried out to build a ROM are reviewed, focusing on those steps that are more relevant to this study, i.e. the possible sources of numerical issues. Considering a second order structural undamped system with N degrees of freedom (DOFs) the equations of motion (EOMs) can be written as

$$\mathbf{M}\ddot{\mathbf{x}} + \mathbf{K}\mathbf{x} = \mathbf{f}, \tag{2.1}$$

where $\mathbf{M}$ is the mass matrix, $\mathbf{K}$ is the stiffness matrix, $\mathbf{f}$ is the vector of generalized forces acting on the structure, and $\mathbf{x}$ is the vector of generalized coordinates. The size of the problem in Eq. 2.1 is $N \times N$, where N can be very large, often of the order of hundreds of millions of DOFs. To reduce the size of the problem, it is convenient to assume that the vector $\mathbf{x}$ can be represented as a linear combination of a set of projection vectors as

$$\mathbf{x} = \mathbf{T}\mathbf{q}, \tag{2.2}$$

where $\mathbf{T}$ is the transformation matrix, whose columns are the projection vectors, and $\mathbf{q}$ is a reduced set of coordinates. By substituting Eq. 2.2 into Eq. 2.1 and pre-multiplying by $\mathbf{T}^T$ in a Galerkin fashion one obtains

$$\mathbf{T}^T\mathbf{M}\mathbf{T}\ddot{\mathbf{q}} + \mathbf{T}^T\mathbf{K}\mathbf{T}\mathbf{q} = \mathbf{T}^T\mathbf{f}, \tag{2.3}$$

which can also be written as

$$\mathbf{M}_{ROM}\ddot{\mathbf{q}} + \mathbf{K}_{ROM}\mathbf{q} = \mathbf{f}_{ROM}. \tag{2.4}$$

The order reduction comes from the fact that the transformation matrix $\mathbf{T}$ is of size $N \times m$, where $m \ll N$. The number of DOFs that are present in Eq. 2.4 after the transformation is thus m. Note that in general, the left ROB does not necessarily have to be equal to the right ROB, as is the case in multi-physical ROMs for example.

Let us now consider the nature of the matrices involved in Eqs. 2.1-2.4. For structural dynamics, matrices $\mathbf{M}$ and $\mathbf{K}$ are positive definite (PD) and positive semidefinite (PSD) respectively, and both are symmetric. When $\mathbf{T}$ is not singular, the resulting $\mathbf{M}_{ROM}$ and $\mathbf{K}_{ROM}$ matrices preserve these properties. Recalling the definition of positive definiteness, we can in fact write for a symmetric matrix $\mathbf{A}$

$$\mathbf{A}_{r\times r} \text{ is PD } \iff \quad \forall \mathbf{v} \in \Re^{\mathrm{r}} \quad \mathbf{v}^{\mathrm{T}}\mathbf{A}\mathbf{v} > 0 \quad \text{if } \mathbf{v} \neq \mathbf{0}. \tag{2.5}$$

Let us now consider the ROM matrices. $\mathbf{M}_{ROM}$ is PD if

$$\mathbf{v}^T\mathbf{M}_{ROM}\mathbf{v} > 0, \text{ i.e. } \mathbf{v}^{\mathrm{T}}\mathbf{T}^{\mathrm{T}}\mathbf{M}\mathbf{T}\mathbf{v} > 0. \tag{2.6}$$

Since the initial matrix $\mathbf{M}$ is PD, $\mathbf{M}_{ROM}$ can only become singular if the transformation matrix is singular, i.e.

$$\mathbf{M}_{ROM} \text{ is } PSD \iff \exists\ \mathbf{v} \in \Re^m \wedge \mathbf{v} \neq \mathbf{0} \quad \text{s.t.} \quad \mathbf{T}\mathbf{v} = \mathbf{0}. \tag{2.7}$$

Thus, if $\mathbf{T}$ is rank deficient, the resulting reduced order mass matrix loses its positive definiteness. This is the fundamental property, alongside with symmetry, that guarantees the

eigenvalues of the system to be real and non-negative. As a result, the matrix pencil in the ROM would lack the fundamental properties of the initial pencil, which are critical for predicting the behavior of the system. Characteristics such as system's stability or energy conservation depend on these properties. Since we wish Eq. 2.4 to hold and to be representative of the original system, the same conditions must be met by the reduced order matrices. Both $\mathbf{M}_{ROM}$ and $\mathbf{K}_{ROM}$ are symmetric by construction, but the positive definiteness depends on the transformation matrix. It is in principle possible to pre-condition the transformation matrix, but that approach is disadvantageous because the size of matrix $\mathbf{T}$ can be prohibitively large. Because of this, it is desirable to condition the ROM matrices after the transformation is applied, so that all the calculations are carried out on matrices with a reduced size.

2.3 *Post-conditioning* technique

In this section, a new conditioning strategy operating in the ROM space is presented. The working principle and the most important features are explained also.

2.3.1 Conditioning formulation

The conditioning technique is based on the reduced-order mass matrix because of its properties. In fact, while $\mathbf{K}$ could be singular, e.g. when the system has rigid body modes, $\mathbf{M}$ must be PD for structural systems. For this reason, it is possible to use the singular values of $\mathbf{M}_{ROM}$ for conditioning. The key idea is to eliminate the smallest singular values by means of a secondary projection. Using SVD, matrix $\mathbf{M}_{ROM}$ can be written as

$$\mathbf{M}_{ROM} = \mathbf{U}\mathbf{\Sigma}\mathbf{V}^T. \tag{2.8}$$

The diagonal matrix $\mathbf{\Sigma}$ can be used to estimate how numerically well-conditioned the reduced-order mass matrix is. Combining Eq. 2.4 and Eq. 2.8, the new EOMs become

$$\mathbf{U\Sigma V}^T\ddot{\mathbf{q}} + \mathbf{K}_{ROM}\mathbf{q} = \mathbf{f}_{ROM}. \tag{2.9}$$

The SVD matrices can be partitioned in a more insightful fashion as

$$\mathbf{M}_{ROM} = \mathbf{U\Sigma V}^T = [\tilde{\mathbf{U}}\ \mathbf{U}_\varepsilon] \begin{bmatrix} \tilde{\mathbf{\Sigma}} & \mathbf{0} \\ \mathbf{0} & \mathbf{\Sigma}_\varepsilon \end{bmatrix} \begin{bmatrix} \tilde{\mathbf{V}}^T \\ \mathbf{V}_\varepsilon^T \end{bmatrix}, \tag{2.10}$$

where $\tilde{}$ indicate quantities that are preserved, while the terms with subscript ε are small quantities that have to be discarded. The size of $\tilde{\mathbf{U}}$ and $\tilde{\mathbf{V}}$ is $m \times n$, with $n < m$, and n being the number of largest singular values retained. The quantities with subscript ε are the ones associated with the smaller singular values (close to zero).

A change of coordinates $\mathbf{q} = \tilde{\mathbf{V}}\boldsymbol{\eta}$ is introduced. One obtains:

$$\mathbf{U\Sigma V}^T\tilde{\mathbf{V}}\ddot{\boldsymbol{\eta}} + \mathbf{K}_{ROM}\tilde{\mathbf{V}}\boldsymbol{\eta} = \mathbf{f}_{ROM}. \tag{2.11}$$

Pre-multiplying Eq. 2.11 by $\tilde{\mathbf{U}}$ gives

$$\tilde{\mathbf{U}}^T\mathbf{U\Sigma V}^T\tilde{\mathbf{V}}\ddot{\boldsymbol{\eta}} + \tilde{\mathbf{U}}^T\mathbf{K}_{ROM}\tilde{\mathbf{V}}\boldsymbol{\eta} = \tilde{\mathbf{f}}_{ROM}, \tag{2.12}$$

where $\tilde{\mathbf{f}}_{ROM} = \tilde{\mathbf{U}}^T\mathbf{f}_{ROM}$. Recalling the partitioning of the matrices in Eq. 2.10, one obtains

$$\tilde{\mathbf{U}}^T[\tilde{\mathbf{U}}\ \mathbf{U}_\varepsilon] \begin{bmatrix} \tilde{\mathbf{\Sigma}} & \mathbf{0} \\ \mathbf{0} & \mathbf{\Sigma}_\varepsilon \end{bmatrix} \begin{bmatrix} \tilde{\mathbf{V}}^T \\ \mathbf{V}_\varepsilon^T \end{bmatrix} \tilde{\mathbf{V}}\ddot{\boldsymbol{\eta}} + \tilde{\mathbf{U}}^T\mathbf{K}_{ROM}\tilde{\mathbf{V}}\boldsymbol{\eta} = \tilde{\mathbf{f}}_{ROM}. \tag{2.13}$$

Recalling the orthogonality of the SVD matrices, Eq. 2.13 simplifies to

$$\tilde{\mathbf{\Sigma}}\ddot{\boldsymbol{\eta}} + \tilde{\mathbf{U}}^T\mathbf{K}_{ROM}\tilde{\mathbf{V}}\boldsymbol{\eta} = \tilde{\mathbf{f}}_{ROM}. \tag{2.14}$$

The EOM presented in Eq. 2.14 are well-conditioned because the values retained in $\tilde{\mathbf{\Sigma}}$ are not close to zero. Notice also that $\mathbf{U} = \mathbf{V}$ for the type of system considered because the mass matrix is symmetric and PD. Finally, Eq. 2.14 can be written as

$$\tilde{\mathbf{M}}\ddot{\boldsymbol{\eta}} + \tilde{\mathbf{K}}\boldsymbol{\eta} = \tilde{\mathbf{f}}_{ROM}, \tag{2.15}$$

where the conditioned mass and stiffness matrices are $n \times n$ matrices $\tilde{\mathbf{M}} = \tilde{\mathbf{\Sigma}}$ and $\tilde{\mathbf{K}} = \tilde{\mathbf{V}}^T\mathbf{K}_{ROM}\tilde{\mathbf{V}}$. This process simplifies and conditions Eq. 2.4 at the same time. The size of the new problem in Eq. 2.15 is in general smaller than the size of the initial ROM because $n < m$. The approach to choose the singular values to be retained is discussed in Sections 2.3.3 and 2.4.

2.3.2 Working principle and physical interpretation

Let us consider the SVD of matrix $\mathbf{M}_{ROM}$, partitioned as presented in Eq. 2.10. Since $\mathbf{\Sigma}_\varepsilon$ only contains the singular values that are close to zero, $\mathbf{V}_\varepsilon$ approximates the null space of $\mathbf{M}_{ROM}$. Thus, the null space is effectively eliminated and the secondary projection prevents the generalized coordinates $\mathbf{q}$ from spanning that part of the solution space. So doing, the nearly singular matrix $\mathbf{M}_{ROM}$ is transformed into a positive definite matrix $\tilde{\mathbf{\Sigma}}$. By expanding the terms in Eq. 2.15, it can be noticed that this is equivalent to applying a transformation matrix $\tilde{\mathbf{T}} = \mathbf{T}\tilde{\mathbf{V}}$ to the original full order model. In fact one can write

$$\mathbf{x} = \mathbf{T}\tilde{\mathbf{V}}\boldsymbol{\eta} = \tilde{\mathbf{T}}\boldsymbol{\eta}. \tag{2.16}$$

Matrix $\tilde{\mathbf{T}}$ is a linear combination of the original vectors in $\mathbf{T}$. This means that the new transformation still contains the physical motions that were contained in $\mathbf{T}$, but in a reduced form; it consists of an exhaustive and linearly independent set of vectors. While this is true theoretically, in numerical applications there is no universal distinction between very small and zero singular values. This means that a small fraction of the information could be lost. In Sections 2.5 and 2.6 we show that this loss of information has a negligible effect on the overall accuracy of the ROM.

In Section 2.3.1 the focus was only on the reduced order mass matrix $\mathbf{M}_{ROM}$. However, the numerical issues arising in the stiffness matrix $\mathbf{K}_{ROM}$ are solved also. The secondary projection implicitly conditions the transformation matrix, which is the same for both matrices $\mathbf{M}_{ROM}$ and $\mathbf{K}_{ROM}$, and thus removes the numerical issues from the matrix $\mathbf{K}_{ROM}$ as well.

2.3.3 Conditioning procedure

Next, an example is presented to demonstrate the proposed technique for a practical case. For the cases considered, the ROM matrices must be PD and PSD respectively. To ensure this, one chooses the partitioning $\tilde{\mathbf{\Sigma}}$ and $\mathbf{\Sigma}_{\varepsilon}$ that results in the matrices preserving their properties. This condition guarantees that the results are feasible and that the new ROM is a proper representation of the initial physical system. The conditioning process is explained in Algorithm 1. First, an SVD is carried out for $\mathbf{M}_{ROM}$. Then the number of singular values discarded is chosen according to a given threshold σ_{th}. The normalized singular values, i.e. the singular values divided by the maximum singular value σ_1, are compared to the threshold. Only the singular values such that $\dfrac{\sigma_i}{\sigma_1} > \sigma_{th}$ are preserved, i.e. their respective singular vectors are added to the transformation matrix. In practical applications the threshold is a small number chosen based on the characteristics of the system.

Algorithm 1 Conditioning procedure

Input: $\mathbf{M}_{ROM_{m\times m}}$, $\mathbf{K}_{ROM_{m\times m}}$, σ_{th}

$[\mathbf{U}, \mathbf{\Sigma}, \mathbf{V}^T] \longleftarrow \text{svd}(\mathbf{M}_{ROM})$;

$\mathbf{V} = \{\mathbf{v}_1, \mathbf{v}_2, \ldots, \mathbf{v}_m\}$;

$\mathbf{\Sigma} = diag(\sigma_1, \sigma_2, \ldots, \sigma_m)$, $\sigma_i > \sigma_j \; \forall \; i < j$;

for $i = 1$ to m **do**

  if $\dfrac{\sigma_i}{\sigma_1} \leq \sigma_{th}$ **then**

    break

  end

  $\tilde{\mathbf{V}} \longleftarrow \{\mathbf{v}_1, \mathbf{v}_2, \ldots, \mathbf{v}_i\}$;

  $\tilde{\mathbf{\Sigma}} \longleftarrow diag(\sigma_1, \sigma_2, \ldots, \sigma_i)$;

end

$\tilde{\mathbf{K}} \longleftarrow \tilde{\mathbf{V}}^T \mathbf{K}_{ROM} \tilde{\mathbf{V}}$;

$\tilde{\mathbf{M}} \longleftarrow \tilde{\mathbf{\Sigma}}$;

return $\tilde{\mathbf{M}}$, $\tilde{\mathbf{K}}$, $\tilde{\mathbf{V}}$

Through the procedure presented in Algorithm 1 it is possible to preserve the relevant information included in the transformation matrix $\mathbf{T}$, which is captured by $\tilde{\mathbf{V}}$. Please note that the truncation of the projection might result in some loss of information, depending on the threshold chosen. To quantify the information loss, a set of error metrics is proposed in the next section. They can be used for the formulation of a similar algorithm based on the values of the proposed error metrics. Furthermore, they can guide the choice of the threshold value, which is typically larger than machine precision but small enough to ensure that the error metric is small.

2.4 Error metrics

In this section, numerical issues potentially associated with the proposed approach are presented, and a solution is proposed. Often times, the transformation chosen is theoretically well-conditioned. However, different vectors of the ROB are close to being linearly dependent, as it will be shown in Sections 2.5 and 2.6. In such cases, the challenge is numerical, and the threshold for conditioning different cases is not as clear. The singular values to be discarded might not be zero, but they may be very small. The equations resulting from a numerically ill-conditioned transformation are meaningful most of the time, but affected by numerical issues. Consequently, an error is committed in the secondary transformation matrix presented in Section 2.3.1. In this section an error metric is introduced to quantify information loss.

Let us consider the secondary transformation presented in Section 2.3.1. If all vectors from $\mathbf{V}$ are retained, it is possible to rewrite the transformation as

$$\mathbf{q} = [\tilde{\mathbf{V}} \ \mathbf{V}_\varepsilon] \begin{Bmatrix} \boldsymbol{\eta} \\ \boldsymbol{\eta}_\varepsilon \end{Bmatrix}. \tag{2.17}$$

After applying the transformation and simplifying, the EOM becomes

$$\begin{bmatrix} \tilde{\boldsymbol{\Sigma}} & \mathbf{0} \\ \mathbf{0} & \boldsymbol{\Sigma}_\varepsilon \end{bmatrix} \begin{Bmatrix} \ddot{\boldsymbol{\eta}} \\ \ddot{\boldsymbol{\eta}}_\varepsilon \end{Bmatrix} + \begin{bmatrix} \mathbf{K}_{\tilde{U}\tilde{V}} & \mathbf{K}_{\tilde{U}V_\varepsilon} \\ \mathbf{K}_{U_\varepsilon\tilde{V}} & \mathbf{K}_{U_\varepsilon V_\varepsilon} \end{bmatrix} \begin{Bmatrix} \boldsymbol{\eta} \\ \boldsymbol{\eta}_\varepsilon \end{Bmatrix} = \begin{bmatrix} \tilde{\mathbf{f}}_{ROM} \\ \mathbf{f}_{ROM\varepsilon} \end{bmatrix}, \tag{2.18}$$

where $\mathbf{K}_{AB} = \mathbf{A}^T\mathbf{T}^T\mathbf{K}\mathbf{T}\mathbf{B}$, with $\mathbf{A}$ and $\mathbf{B}$ being $\tilde{\mathbf{U}}$, $\mathbf{U}_\varepsilon$, $\tilde{\mathbf{U}}$ or $\mathbf{V}_\varepsilon$. Equation 2.18 is equivalent to Eq. 2.14 when all the vectors are retained in $\tilde{\mathbf{V}}$. From a different perspective, the first row of Eq. 2.18 is equivalent to Eq. 2.14 under the assumption that

$$\mathbf{K}_{\tilde{U}V_\varepsilon}\boldsymbol{\eta}_\varepsilon \cong \mathbf{0}. \tag{2.19}$$

The *post-conditioning* approach presented in Section 2.3.1 leads to Eq. 2.14, which can be solved for $\boldsymbol{\eta}$. The value of $\boldsymbol{\eta}$ can then be used to evaluate $\boldsymbol{\eta}_\varepsilon$ by imposing Eq. 2.18 to hold. The first row of Eq. 2.18 evaluated for $\boldsymbol{\eta}$ obtained from Eq. 2.15 becomes simply Eq. 2.19. Thus, Eq. 2.18 becomes

$$\begin{cases} \mathbf{K}_{\tilde{U}V_\varepsilon}\boldsymbol{\eta}_\varepsilon = \mathbf{0} \\ \boldsymbol{\Sigma}_\varepsilon\ddot{\boldsymbol{\eta}}_\varepsilon + \mathbf{K}_{U_\varepsilon\tilde{V}}\boldsymbol{\eta} + \mathbf{K}_{U_\varepsilon V_\varepsilon}\boldsymbol{\eta}_\varepsilon = \mathbf{f}_{ROM\varepsilon} \end{cases} . \tag{2.20}$$

Once $\boldsymbol{\eta}_\varepsilon$ is obtained, it can be used to estimate the error committed truncating the secondary transformation. Two approaches are considered, static and dynamic. Both approaches use Eq. 2.20 to determine $\boldsymbol{\eta}_\varepsilon$.

2.4.1 Static approach

A first approach to solve Eq. 2.20 is to neglect $\boldsymbol{\Sigma}_\varepsilon$. This is a reasonable approximation given the fact that the terms in the matrix $\boldsymbol{\Sigma}_\varepsilon$ are very small. This approach provides a static error because $\boldsymbol{\eta}_\varepsilon$ is obtained by neglecting the contribution of the dynamic term in Eq. 2.20 to obtain

$$\begin{cases} \mathbf{K}_{\tilde{U}V_\varepsilon}\boldsymbol{\eta}_\varepsilon = \mathbf{0} \\ \mathbf{K}_{U_\varepsilon\tilde{V}}\boldsymbol{\eta} + \mathbf{K}_{U_\varepsilon V_\varepsilon}\boldsymbol{\eta}_\varepsilon = \mathbf{f}_{ROM\varepsilon} \end{cases} . \tag{2.21}$$

The value of $\boldsymbol{\eta}_\varepsilon$ can be expressed as

$$\boldsymbol{\eta}_\varepsilon = \begin{bmatrix} \mathbf{K}_{\tilde{U}V_\varepsilon} \\ \mathbf{K}_{U_\varepsilon V_\varepsilon} \end{bmatrix}^\dagger \begin{bmatrix} \mathbf{0} \\ -\mathbf{K}_{U_\varepsilon\tilde{V}}\boldsymbol{\eta} + \mathbf{f}_{ROM\varepsilon} \end{bmatrix}, \tag{2.22}$$

where † represents the pseudoinverse of the matrix. The value of $\boldsymbol{\eta}$ could be arbitrarily chosen. In particular, $\boldsymbol{\eta}$ can be any one of the mode shapes obtained from the eigenvalue

problem associated with Eq. 2.15, namely

$$-\omega_i^2 \tilde{\mathbf{M}} \boldsymbol{\eta}_i + \tilde{\mathbf{K}} \boldsymbol{\eta}_i = 0, \tag{2.23}$$

where ω_i are the eigenfrequencies and $\boldsymbol{\eta}_i$ are the modes. A value $\boldsymbol{\eta}_{\varepsilon i}$ can be obtained for each $\boldsymbol{\eta}_i$ using Eq. 2.22.

2.4.2 Dynamic approach

A second approach is to include the dynamic term involving the generalized coordinates $\boldsymbol{\eta}_\varepsilon$ in Eq. 2.20. Equation 2.20 can be solved using a standard ODE solver for a given $\boldsymbol{\eta}(t)$. As an alternative, a frequency domain solution can be found for each of the modes $\boldsymbol{\eta}_i$ obtained from a modal analysis applied to Eq. 2.15. In that case, Eq. 2.20 becomes

$$\begin{cases} \mathbf{K}_{\tilde{U}V_\varepsilon} \boldsymbol{\eta}_{\varepsilon_i} = \mathbf{0} \\ -\omega_i^2 \boldsymbol{\Sigma}_\varepsilon \boldsymbol{\eta}_{\varepsilon_i} + \mathbf{K}_{U_\varepsilon \tilde{V}} \boldsymbol{\eta}_i + \mathbf{K}_{U_\varepsilon V_\varepsilon} \boldsymbol{\eta}_{\varepsilon_i} = \mathbf{f}_{ROM\,\varepsilon} \end{cases}, \tag{2.24}$$

which gives

$$\boldsymbol{\eta}_{\varepsilon_i} = \begin{bmatrix} \mathbf{K}_{\tilde{U}V_\varepsilon} \\ -\omega_i^2 \boldsymbol{\Sigma}_\varepsilon + \mathbf{K}_{U_\varepsilon V_\varepsilon} \end{bmatrix}^\dagger \begin{bmatrix} \mathbf{0} \\ -\mathbf{K}_{U_\varepsilon \tilde{V}} \boldsymbol{\eta}_i + \mathbf{f}_{ROM\,\varepsilon} \end{bmatrix}. \tag{2.25}$$

2.4.3 Error metric evaluation

As explained at the beginning of Section 2.4, it is necessary to obtain $\boldsymbol{\eta}_\varepsilon$ in order to estimate the error. This can be done using the techniques presented in Sections 2.4.1 and 2.4.2. Typically, these calculations are carried out for multiple vectors. The use of multiple vectors is recommended so that the entire range of motion is included in the analysis. In this section it is assumed that the n modal vectors obtained through Eq. 2.23 are used. Once

all $\boldsymbol{\eta}_i$ and $\boldsymbol{\eta}_{\varepsilon_i}$ are obtained, the error metric e can be calculated as

$$e = \frac{\sum_{i=1}^{n} \frac{1}{2} \boldsymbol{\eta}_{\varepsilon_i}^T \mathbf{K}_{U_\varepsilon V_\varepsilon} \boldsymbol{\eta}_{\varepsilon_i}}{\sum_{j=1}^{n} \frac{1}{2} \boldsymbol{\eta}_j^T \mathbf{K}_{\tilde{U}\tilde{V}} \boldsymbol{\eta}_j}. \tag{2.26}$$

For the specific case examined in Eq. 2.1, recall that the matrices $\mathbf{U}$ and $\mathbf{V}$ are the same, and thus with the appropriate change of coordinates, the ratio presented above reduces to

$$e = \frac{\sum_{i=1}^{n} \frac{1}{2} \mathbf{x}_{\varepsilon_i}^T \mathbf{K} \mathbf{x}_{\varepsilon_i}}{\sum_{j=1}^{n} \frac{1}{2} \mathbf{x}_j^T \mathbf{K} \mathbf{x}_j}, \tag{2.27}$$

where $\mathbf{x}_{\varepsilon_i} = \mathbf{T}\mathbf{V}_\varepsilon \boldsymbol{\eta}_{\varepsilon_i} = \mathbf{T}_\varepsilon \boldsymbol{\eta}_{\varepsilon_i}$ is the physical displacement associated with the generalized coordinates that have been neglected, and $\mathbf{x}_j = \mathbf{T}\tilde{\mathbf{V}}\boldsymbol{\eta}_j = \tilde{\mathbf{T}}\boldsymbol{\eta}_j$ is the physical displacement associated with the generalized coordinates that have been kept. Thus, the numerator represents the strain energy that was neglected, and the denominator represents the strain energy preserved in the model. The value of $\mathbf{x}_\varepsilon$ and the corresponding strain energy are expected to be negligible. This is because $\mathbf{V}_\varepsilon$ lies in the kernel of $\mathbf{T}$. The metric in Eq. 2.26 is insightful because it relates quantities in the ROM space to physical quantities, without the need to expand to physical coordinates.

2.5 Example of the conditioning strategy

To demonstrate the conditioning strategy, a simple structure is considered next. The system presented in Figure 2.1 consists of a chain of coupled oscillators. Please note that the first and the last oscillators are connected to each other. The number of oscillators, and thus the number of DOFs is $N = 100$.

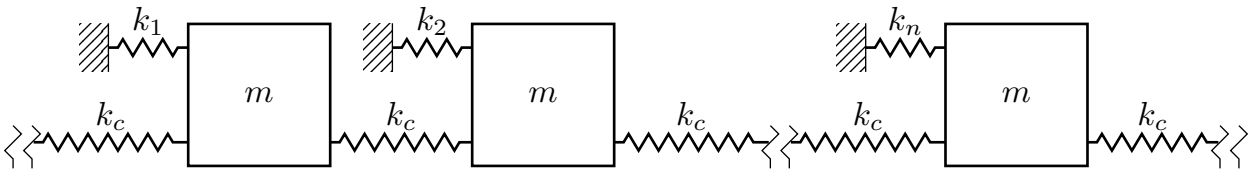

Figure 2.1: Schematic of a system of coupled oscillators

The equation of motion for the i^{th} oscillator is given by

$$m\ddot{x}_i + k_i x_i + k_c(2x_i - x_{i+1} - x_{i-1}) = f_i, \tag{2.28}$$

where m is the mass of the oscillator, k_i and k_c are the spring stiffnesses, f_i is the forcing term applied to the i^{th} oscillator, and x_i the respective displacement. The equations of motion can be formulated in matrix form, as shown in Eq. 2.1. In that case it is possible to write $\mathbf{M} = m\mathbf{I}$, with $\mathbf{I}$ being the $N \times N$ identity matrix, and

$$\mathbf{K} = \begin{bmatrix} k_1 + 2k_c & -k_c & 0 & \cdots & 0 & -k_c \\ -k_c & k_2 + 2k_c & -k_c & & & 0 \\ 0 & \ddots & \ddots & \ddots & & \vdots \\ \vdots & & \ddots & \ddots & \ddots & 0 \\ 0 & & & -k_c & k_{N-1} + 2k_c & -k_c \\ -k_c & 0 & \cdots & 0 & -k_c & k_N + 2k_c \end{bmatrix}. \tag{2.29}$$

The system under investigation has two sets of stiffness values, depending on the position of the springs. The first 50 oscillators have 20% larger stiffness, thus we can write $k_i = 1.2 \cdot k_0$ if $1 < i < 50$ and $k_i = k_0$ when $51 < i < 100$. The EOMs can be nondimensionalized by dividing through by k_o and introducing the ratio $R = k_c/k_o$. Thus, the normalized stiffness

matrix $\tilde{\mathbf{K}}$ becomes

$$\tilde{\mathbf{K}} = \frac{1}{k_0}\mathbf{K} = \begin{bmatrix} 1.2+2R & -R & 0 & \cdots & 0 & -R \\ -R & 1.2+2R & -R & & & 0 \\ 0 & \ddots & \ddots & \ddots & & \vdots \\ \vdots & & \ddots & \ddots & \ddots & 0 \\ 0 & & & -R & 1+2R & -R \\ -R & 0 & \cdots & 0 & -R & 1+2R \end{bmatrix}. \tag{2.30}$$

Consider that this system is mistuned, i.e. contains small stiffness variations in its springs. Thus, the i^{th} oscillator is connected to a spring with a stiffness $\hat{k}_i = k_i + \delta_i$, where δ_i are normally distributed random variables representing stiffness variations. Thus, the normalized mistuned stiffness matrix becomes

$$\bar{\mathbf{K}} = \begin{bmatrix} (1.2+\delta_1)+2R & -R & 0 & \cdots & 0 & -R \\ -R & (1.2+\delta_2)+2R & -R & & & 0 \\ 0 & \ddots & \ddots & \ddots & & \vdots \\ \vdots & & \ddots & \ddots & \ddots & 0 \\ 0 & & & -R & (1+\delta_{N-1})+2R & -R \\ -R & 0 & \cdots & 0 & -R & (1+\delta_N)+2R \end{bmatrix}. \tag{2.31}$$

By introducing the dimensionless natural frequency $\bar{\omega} = \omega\sqrt{\frac{m}{k_o}}$, and recalling the structure of the matrix $\mathbf{M}$, the dimensionless eigenvalue problem for the mistuned system becomes

$$\bar{\mathbf{K}}\mathbf{x} = \bar{\omega}^2\mathbf{x}. \tag{2.32}$$

A ROM to study the mistuned system is created. The first 100 nondimensionalized eigenvalues for the mistuned system under investigation are presented in Figure 2.2a. They

are obtained using normally distributed δ_i having mean $\mu = 0$ and standard deviation $\sigma = 0.01$, with coupling parameter $R = 0.1$. They are used as a reference to compare the accuracy of the ROMs.

To prove the effectiveness of the *post-conditioning* technique, a numerically ill-behaved transformation is created for the projection by an approach often used when constructing parametric ROMs [24]. In that approach, the ROB is constructed by calculating modes of the system at various parameter values, and adding them to the set of projection vectors. To examine the effects of such an approach, consider that the mistuned response is expressed as a linear combination of several sets of tuned and mistuned eigenvectors. The mistuned eigenvalues and eigenvectors are obtained by separately applying three known mistuning patterns, which are different from the mistuning pattern present in the system. The eigenvectors having lowest natural frequencies are chosen. The transformation used to obtain the ROM can thus be written as

$$\mathbf{x} = \mathbf{T}\boldsymbol{\eta} = \begin{bmatrix} \boldsymbol{\Phi}_0 & \boldsymbol{\Phi}_1 & \boldsymbol{\Phi}_2 & \boldsymbol{\Phi}_3 \end{bmatrix} \boldsymbol{\eta}, \tag{2.33}$$

where $\mathbf{x}$ is the vector of physical displacements, $\boldsymbol{\Phi}_0$ is the set of tuned vectors and $\boldsymbol{\Phi}_1$, $\boldsymbol{\Phi}_2$ and $\boldsymbol{\Phi}_3$ are the mistuned projection vectors obtained for each of the three known mistuning pattern. Every set of modes includes 20 vectors This results in a ROM of the form of Eq. 2.4, of size $m = 80$. Recall that these projection vectors result in a transformation matrix that is numerically ill-conditioned and requires conditioning.

Figure 2.2b shows the eigenvalues of the unconditioned ROM. It is important to notice that the ROM returns negative eigenvalues, and that the eigenvalues of the unconditioned ROM can be complex or unbounded, even if the initial system was undamped. This is due to the fact that the transformation matrix is not full rank, and thus the ROM matrices are ill-conditioned. Due to the fact that only the 20 lowest normal modes were included in the

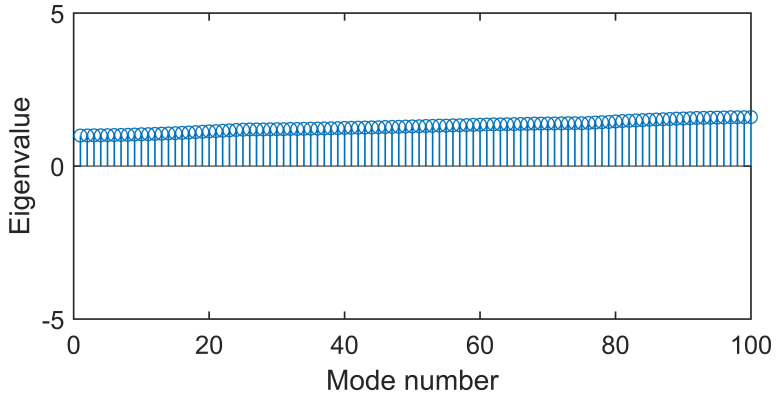

(a) Eigenvalues of the full order model

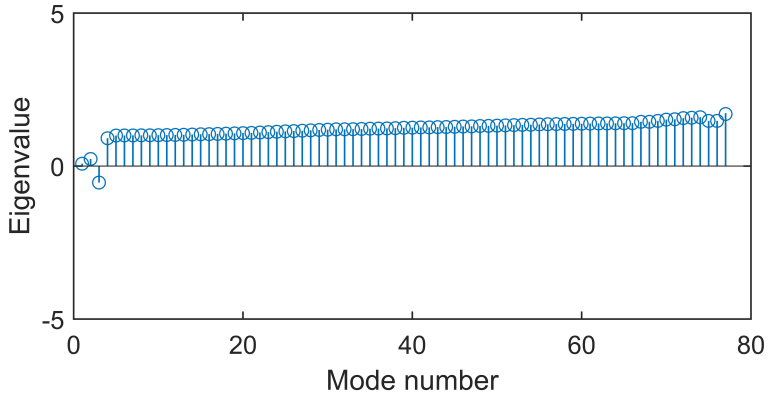

(b) Eigenvalues of the unconditioned ROM

Figure 2.2: Nondimensionalized eigenvalues of the system

transformation, we can expect accurate results only for the first 20 eigenvalues, while the others are inaccurate due to the lack of corresponding modal information. The results are compared using the eigenvalue error between the eigenvalues λ_{ROM} of the ROM and λ_{FOM} of the full order model, defined as

$$\lambda_{err} = \frac{|\lambda_{ROM} - \lambda_{FOM}|}{\lambda_{FOM}}. \tag{2.34}$$

From Figure 2.3a it can be noticed that there is a large error between full order model and unconditioned ROM due to the presence of spurious eigenvalues. When *post-conditioning* is applied to the ROM the results shown in Figure 2.3b are obtained. The threshold for the

singular values used in the application of Algorithm 1 was chosen to be $\sigma_{th} = 10^{-15}$. It is important to notice that the conditioned ROM (CROM) returns only positive eigenvalues. Furthermore, the error between the first 20 eigenvalues of the full order model and the CROM is of the order of 10^{-9}. Thus, we can conclude that the information retained in the CROM is the one needed to capture the system behavior. The modal assurance criterion (MAC) [83] can be used to evaluate if the modes extracted resemble the ones of the full order model. Figure 2.4 shows the MAC plot obtained for ROM and CROM, with the modes ordered according to their eigenvalues. Only MAC values larger than 0.85 are plotted. It is possible to notice that the CROM provides the correct modes in the correct order, while the unconditioned ROM provides them in arbitrary order, with many spurious modes present. Note that in general it is impossible to know the modes of the system a priori. Thus, the conditioning strategy presented is important.

2.5.1 Free Response

To prove that the CROM can be effectively used to predict the dynamics of the system, the free response is analyzed as well. The results of three models are shown and compared, namely the full order model, the ROM, and the CROM. The results are obtained in the time domain, and the resulting ordinary differential equations are solved numerically. The full order results are used as a baseline to evaluate the accuracy of the other two. The initial condition is chosen using a random combination of the first 50 modes included in the transformation and null initial velocity. Figure 2.5 presents the results for the first two oscillators. No difference can be noticed between the CROM and the FOM. In fact, it can be noticed from Figure 2.5 that the full order model and the CROM solutions perfectly overlap, whereas the difference with the unconditioned ROM increases over time. This proves that the ROM matrices are ill-conditioned and require conditioning.

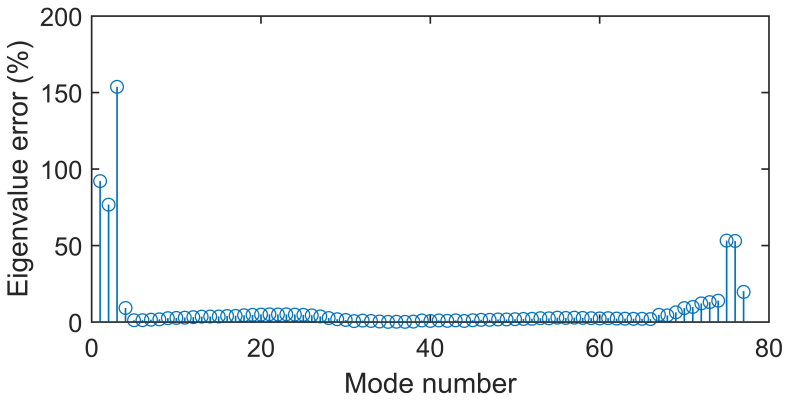

(a) Unconditioned case

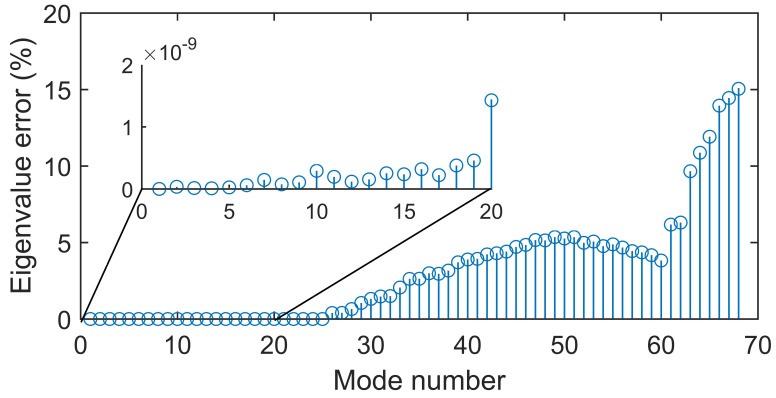

(b) *Post-conditioned* case

Figure 2.3: Eigenvalue errors for the conditioned and unconditioned ROM

2.5.2 Error metrics evaluation

To evaluate the loss of information due to the secondary projection, one can use the error metrics presented in Section 2.4. For the case considered here, the size of the ROM was reduced from $m = 80$ to $n = 68$, i.e. the algorithm discarded twelve singular values and their respective vectors. Using the static approach where $\boldsymbol{\eta}_{\varepsilon_i}$ is based on Eq. 2.22 presented in Section 2.4.1, we obtain the error $e_s = 2.62 \cdot 10^{-7}$. If we use the dynamic approach where $\boldsymbol{\eta}_{\varepsilon_i}$ is defined in Eq. 2.25 from Section 2.4.2, the error becomes $e_d = 6.38 \cdot 10^{-7}$. As expected, both metrics return a very small error. From a practical standpoint this means that there is no information loss.

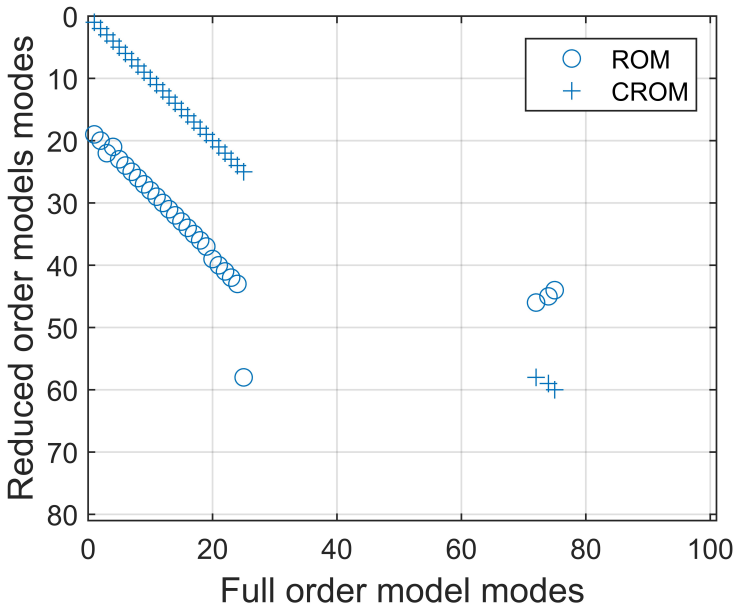

Figure 2.4: MAC plot for CROM and ROM showing only the modes having MAC > 0.85

2.6 ROM of a blended blisk

Let us now consider a more complex case of a ROM for a bladed disk. This structure has cyclic symmetry, a feature that is often used to substantially reduce the computational burden [2]. However, when slight modifications such as stiffness mistuning or blended blades are present, the symmetry is destroyed, resulting in a substantially different response [4]. In those cases other techniques, such as Craig-Bampton component mode synthesis, are usually employed to create ROMs. In this section, the case of a bladed disk with two blended blades such as the one shown in Figure 2.6 is considered. The initial EOMs are in the same form as Eq. 2.1, and the approach used here for the ROM creation is the one proposed by Gan et al. [10]. In this approach the concept of modal constraint modes (MCMs) is introduced. This concept is somewhat similar to the wave-based substructuring presented in [27]. It poses potential problems from a numerical perspective, because MCMs are not guaranteed to be linearly independent, and thus can potentially create an ill-conditioned transformation

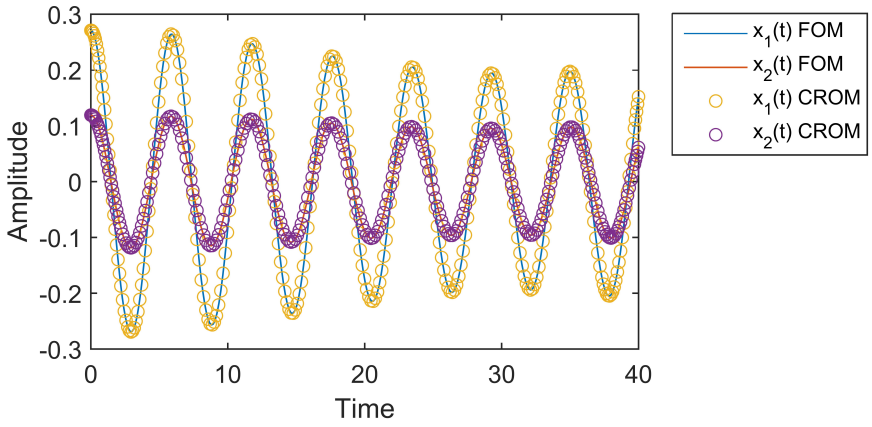

(a) CROM results compared to full order model (FOM) results

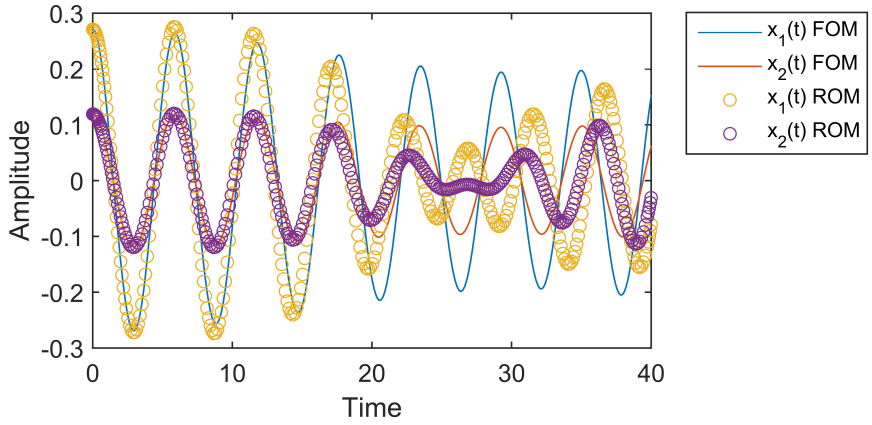

(b) ROM results compared to full order model (FOM) results

Figure 2.5: Free response of the system

matrix. In addition, blend acceleration modes (BAMs) are introduced in the method to accelerate convergence. This poses another challenge due to the very localized motion and different scaling that these vectors have. The modal content introduced with MCMs can also overlap with BAMs and thus introduce an additional problem. The ROM used in this case is substantially more complicated than the one presented in Section 2.5, but it can be summarized as

$$\mathbf{T} = \begin{bmatrix} \boldsymbol{\Phi}_{MCM} & \boldsymbol{\Phi}_{BAM} & \boldsymbol{\Phi} \end{bmatrix}, \tag{2.35}$$

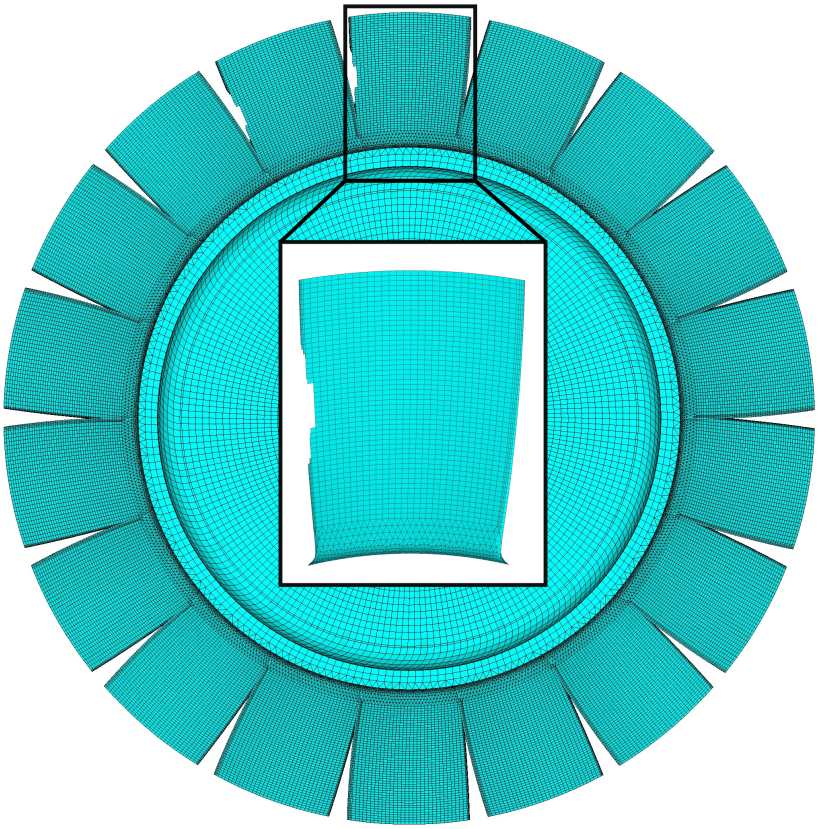

Figure 2.6: Blisk with two blends

where $\mathbf{\Phi}_{MCM}$ represents the MCMs vectors, $\mathbf{\Phi}_{BAM}$ the BAMs vectors, and $\mathbf{\Phi}$ the normal modes.

The full size model of the blisk has $522,666$ nodes, resulting in $1,567,998$ DOFs. The model size can be reduced to 550 by means of substructuring and projection, considering 316 normal modes, 30 BAMs and 204 MCMs. The method is validated by comparing the ROM natural frequencies to the ones obtained using the FOM, using the formulation of Eq. 2.34 for the error calculation.

Before examining the results, it is important to study the ROM mass matrix. The singular values of the mass matrix are shown in Figure 2.7. Two things can be noticed. First, the singular values are spread over a large range of values. Second, some of the singular values

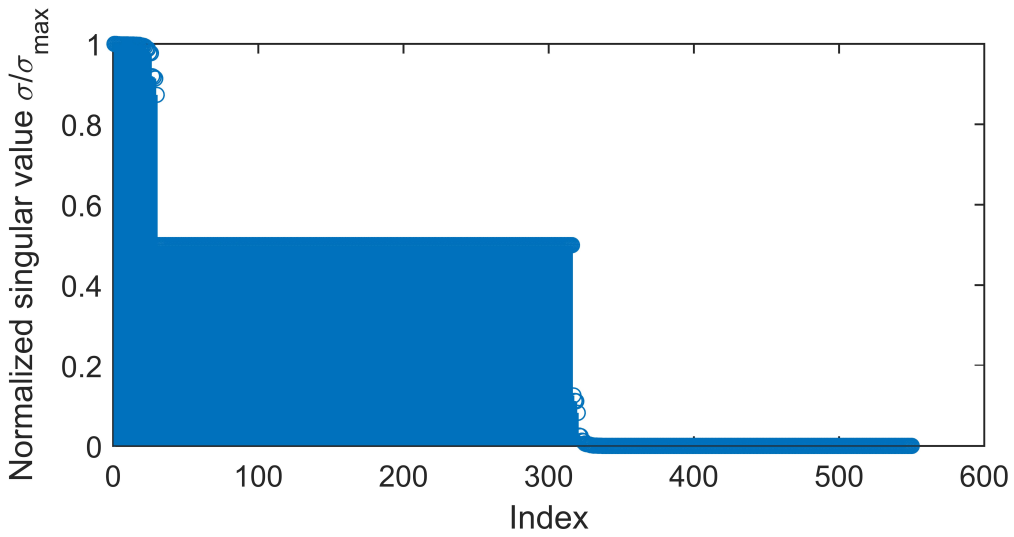

Figure 2.7: Normalized singular values of the ROM mass matrix

are extremely small. The smallest singular value is in fact $\frac{\sigma_{min}}{\sigma_{max}} = 2.5 \cdot 10^{-18}$, and many others are in machine precision. As explained in Section 2.3, ill-conditioned transformation matrices cause the mass matrix to become nearly singular, as shown in this case.

If all the modes are included in the transformation $\mathbf{T}$ without any form of conditioning, the results presented in Figure 2.8a are obtained. It is possible to notice that the error in the predicted natural frequencies is extremely large. Furthermore, some of the eigenvalues are complex. Using the *post-conditioning* algorithm presented in Section 2.3.3, the results shown in Figure 2.8b are obtained. They show an almost perfect match with the full order model.

To ensure that the error comes from the ROM approximation and not from the conditioning algorithm, the results were compared with the ones obtained using *pre-conditioning*. The pre-conditioned results are shown in Figure 2.8c. The differences between the two sets of results are almost negligible, proving that *post-conditioning* can be used in lieu of *pre-conditioning*. The difference between the results from the two conditioned ROMs stems from the fact that the projection vectors are conditioned according to different norms, and thus the modal information retained is slightly different.

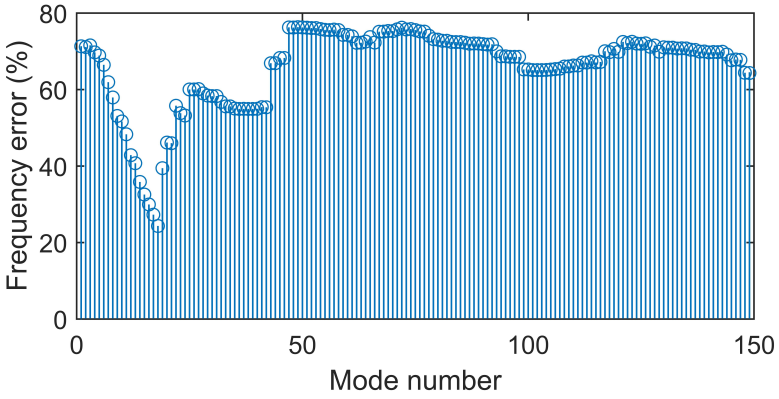

(a) Unconditioned ROM

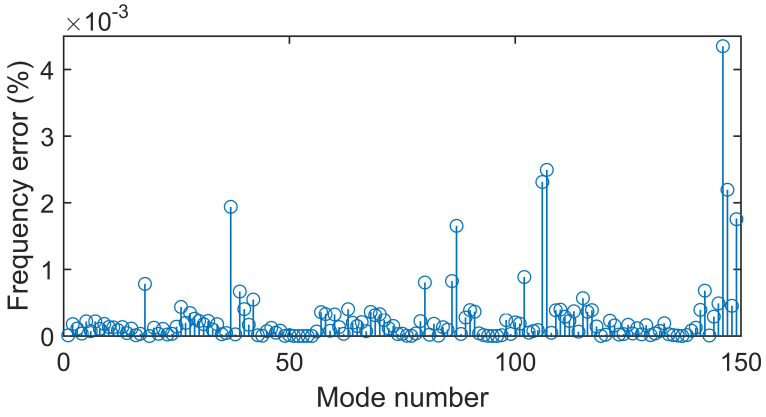

(b) *Post-conditioned* ROM

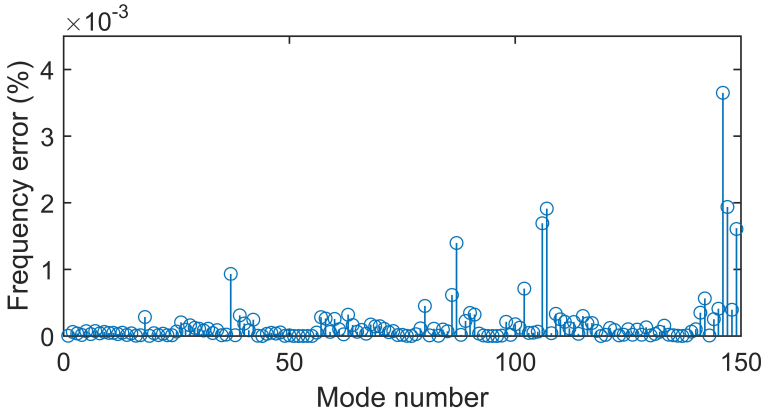

(c) *Pre-conditioned* ROM

Figure 2.8: Natural frequency errors with respect to the full order model

2.6.1 Error metrics evaluation

To examine the validity of the *pre-conditioning* approach, the metrics from Section 2.4 are used. The size of the ROM changed in this case from $m = 550$ for the unconditioned case to $n = 402$ for the conditioned case. The singular values discarded were 148, more than the case discussed in Section 2.5 due to the larger size of the ROM and due to the ill-behaved nature of the transformation matrix. Using the error calculation strategy referred to as *static* in Section 2.4.1, we obtain an error $e_s = 9.98 \cdot 10^{-13}$. Using the *dynamic* metric from Section 2.4.2 we obtain an error $e_d = 5.24 \cdot 10^{-13}$.

2.7 Computational savings

One of the main advantages of the method proposed here is that the most computationally expensive step, in this case the SVD, is carried out in the ROM space. Compared to *pre-conditioning*, the cost of the projection $\mathbf{T}^T\mathbf{M}\mathbf{T}$ can be higher, due to the fact that none of the vectors are discarded before the multiplication. However, the time and memory required for the SVD are substantially reduced. In order to compare the performances of the two approaches, the steps necessary to form and condition a ROM are carried out for both *pre-conditioning* and *post-conditioning*. They can be represented as follows

$$\begin{cases} \textit{Pre-conditioning} & \mathbf{T} = \mathbf{U}\mathbf{\Sigma}\mathbf{V}^T \rightarrow \tilde{\mathbf{T}} = \tilde{\mathbf{U}} \rightarrow \mathbf{M}_{ROM} = \tilde{\mathbf{T}}^T\mathbf{M}\tilde{\mathbf{T}} \\ \textit{Post-conditioning} & \mathbf{M}_{ROM} = \mathbf{T}^T\mathbf{M}\mathbf{T} \rightarrow \mathbf{M}_{ROM} = \mathbf{U}\mathbf{\Sigma}\mathbf{V}^T \rightarrow \tilde{\mathbf{\Sigma}} \end{cases}$$

where the stiffness matrix multiplications are done the same way, and are omitted for the sake of brevity, but they are still taken into account in the calculations. In both cases, the size of the initial transformation matrix is $N \times m$, and the final ROM size is $n \times n$, where $n < m$.

The computational time reduction achieved for the conditioning procedure is presented

in Figure 2.9 as a function of the number N of physical DOFs. Calculations are carried out for a given combination of m and n, in this case 600 and 540 respectively. It is possible to notice that the computational gains increase for larger N. The efficiency of the approach depends on the number of linearly dependent vectors, reaching its peak when only few of them must be discarded.

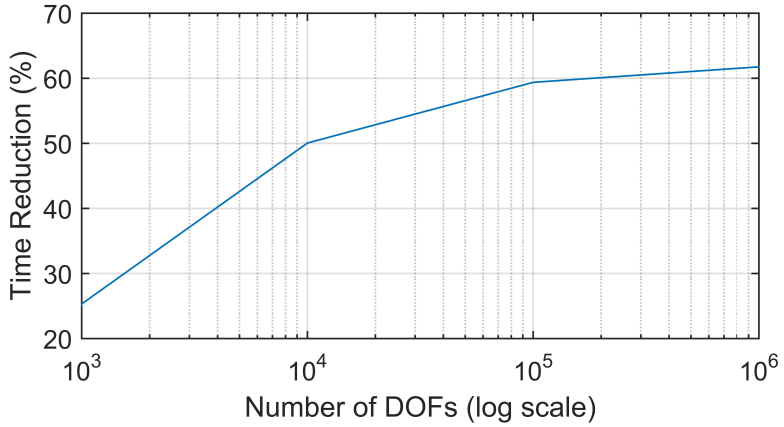

Figure 2.9: Computational savings obtained using *post-conditioning* for a case with $m = 600$ and $n = 540$

2.8 Conclusions

A *post-conditioning* approach to condition projection-based reduced order models was developed. The SVD of the reduced mass matrix is used as a conditioning tool. This technique works in the ROM space with the aim of reducing the computational cost compared to methods that condition the transformation matrix, i.e. *pre-conditioning* methods. The singular values of the reduced mass matrix are used to identify the set of vectors to be retained, which are then implicitly chosen by means of a secondary projection based on the right singular vectors. The secondary projection removes the null-space of the transformation matrix, and does so implicitly. By doing so, the singularity of the matrices is eliminated. Thanks to the nature of the SVD matrices, the conditioning multiplications lead to a particularly

simple form of the ROM, in which the conditioned mass matrix is already diagonal, further simplifying the calculations. Error metrics are introduced to evaluate the error committed by using the secondary projection. Both the method and the error metrics have been tested and validated using a chain of oscillators as well as ROM for a bladed disk (blisk) model. The proposed method presents a number of advantages:

1. The method directly acts in the ROM space, and so there is no need to condition a priori the projection matrix, resulting in faster calculations.

2. No explicit knowledge of the transformation matrix is required. Thus, the method can be easily applied to already existing models by adding a simple *post-conditioning* step.

3. The method can be applied to a variety of ROMs, built using any arbitrary choice of reduced order bases. Most structural dynamical systems may be treated using this approach.

4. The method preserves the physical meaning of the transformation matrix, and the meaning of the equations of motion also. This feature allows for simplifications in the ROM creation when specific types of vectors are used (e.g., normal modes).

Even though the formulation presented targeted Galerkin ROMs, this conditioning idea can be extended to the general case in which Petrov-Galerkin projection is used. Further work can also be done to extend this formulation to the more general case of nonlinear dynamical systems.

CHAPTER 3

On the Use of Mesh Morphing Techniques in Reduced Order Models for the Structural Dynamics of Geometrically Mistuned Blisks

A technique is proposed to overcome computational issues caused by the use of multiple meshes in reduced order models (ROMs) for the structural dynamics of mistuned blisks. Due to the need for repairs (blends) or geometric changes during design iterations, models often require the use of distinct meshes for the same component. Most ROMs for such cases start from pristine modal information, which must be obtained for every mesh involved. Due to the nature of normal modes in cyclic structures, a first challenge arises with respect to their correct clocking, or alignment. Modes have arbitrary clocking for cyclic symmetric systems, and hence modes are potentially different for different meshes. In addition to this, imperfect clocking and cyclic interface compatibility can strongly affect the accuracy of the predicted response. This paper presents a method to preserve the accuracy of ROMs and at the same time reduce the computational overhead associated with the presence of multiple morphed meshes. Numerical issues associated with the presence of multiple meshes and sets of modes are investigated.

3.1 Introduction

Over the past decades, the increase in computational capabilities has led to an increased use of simulation in design. The use of different meshes or of mesh morphing techniques is very common in the design process. Mesh morphing in structural dynamics is particularly useful thanks to its ability to transform existing meshes without requiring a completely new mesh every time the design is changed. Thus, evaluating and optimizing multiple designs can be accomplished with savings in both computational time and cost. Several studies have been focusing on the development of mesh morphing techniques [84–89], and examples of their use can be found across all engineering disciplines. In particular, mesh morphing techniques are commonly used in shape parametrization and design optimization studies [85, 90–99]. Typical applications can be found in automotive studies [86, 100, 101], as well as aerodynamics [92, 99] and turbomachinery [31–34]. The level of detail of computer models increased with the improvement of computational capabilities, resulting in prohibitive computational cost for their solution. For this reason, the use of reduced-order models (ROMs) is very popular. Several techniques have been developed, including POD-based methods [102, 103] and discrete empirical interpolation [104] in fluid dynamics, fluid-structural systems [105], and general partial differential equations [106, 107]. Applications can also be found in the study of microelectromechanical systems (MEMS) devices [108–110] and turbomachinery, where projection-based ROMs are commonly used [8–13]. The concurrent use of ROMs and mesh morphing can be found in design analyses where the full order solution is too expensive computationally, and it is cumbersome to re-generate new meshes for all design iterations. Thanks to the popularity of these two techniques, it is common to find the joint use of ROMs and mesh morphing or shape parametrization [93, 99, 111].

When it comes to cyclic symmetric structures, such as the ones found in turbomachinery, other challenges arise. The dynamics of cyclic structures can be substantially altered by the

presence of mistuning [4], i.e. any noncyclic deviation from the nominal system. Perfect symmetry is unattainable in real structures, and hence mistuning is always present. Thus, cyclic predictions are not always accurate, and full-wheel analyses must be carried out. This leads to a substantial increase in the required computational cost associated with the solution of the full order model (FOM). For this reason, the use of ROMs is important. When geometric changes are large, as is the case in the presence of blends (e.g., repairs applied to some of the sectors), advanced mesh morphing techniques can be used to ensure that the finite element (FE) model accurately represents the blended geometry and maintains mesh quality (e.g., it does not result in coarsely represented surfaces). The morphing process must be carried out for each geometrically mistuned blade in the assembly, resulting in a system that potentially has as many different sector meshes as the number of sectors. Several techniques have been proposed for the study of the structural dynamics of geometrically mistuned blisks [8–13] and for the solution of the numerical issues associated with such ROMs [112]. However, only a few studies focus on the issues that may arise when using multiple meshes, such as mode clocking, interface compatibility, and projection errors. The issue of mode clocking is discussed in detail in [9], where a solution to deal with small geometric mistuning is proposed. However, the small mistuning assumption does not hold for large blends, such as the one shown in Fig. 3.1, where it can be seen that the morphed and the pristine unmorphed sectors have substantially different FE node numbers and topologies. In that case, not only the clocking might affect the results, but also the mesh compatibility at the (disk) interface between sectors. This compatibility can be expressed as a set of constraints on node pairs requiring them to experience the same motion [12]. This becomes a significant challenge especially when acceleration modes are used, like in the case of the MAX method [10]. Furthermore, the method used in [10] involves the calculation of multiple sets of pristine modes, which requires significant computational time. Another drawback of the methods mentioned above is that they only deal with meshes having the same number of nodes. This

is not always the case, as mesh refinement might be necessary in regions that are highly morphed. Thus, it is not efficient to use the methods presented in [9, 12]. A method able to tackle both interface compatibility and clocking issues for the calculation of pristine morphed normal modes is proposed in this paper. Consider an initial (pristine) mesh which has been morphed in various ways to model various blending geometries. The proposed approach is able to avoid the need to solve eigenvalue problems of high computational cost in the process of calculating normal modes for each new/morphed mesh. Instead, the technique proposed exploits the fact that most of the nodes of the new meshes maintain their original (pristine) physical location in the blisk. This is also true of the interface nodes. These nodes cannot be moved because mesh compatibility has to be enforced between morphed and unmorphed parts of the model. Thus, modal information is already available for those nodes, and need not be re-calculated. For the set of nodes that do not have a one-to-one mapping to the original ones, the modal displacement is obtained by solving a forced response problem that only affects that set of nodes. As a result, the computational cost is substantially reduced, while correct clocking and compatibility are implicitly enforced. The new method outperforms others in the literature in terms of speed and memory requirements, as it reduces both the number of computations required and the problem dimensionality. The method is validated by comparing ROM results with full order model results.

3.2 Background

The equations of motion (EOMs) for the structural dynamics of a mechanical structure can be written as

$$\hat{\mathbf{M}}\ddot{\mathbf{x}} + \hat{\mathbf{K}}\mathbf{x} = \mathbf{F}, \tag{3.1}$$

where $\hat{\mathbf{M}}$ is the mass matrix, $\hat{\mathbf{K}}$ is the stiffness matrix, $\mathbf{x}$ is the vector of physical degrees of freedom (DOFs), and $\mathbf{F}$ is the vector of external forces. In this paper, we focus on nominally cyclic symmetric structures like blisks, which are composed of several sectors that can have different morphed meshes. The presence of multiple meshes or mistuning makes the system lose cyclic symmetry properties. As a result, particular care must be taken when handling system modes and matrices. Let us consider the case of a cyclic symmetric system having identical meshes in all the sectors. Due to the symmetry of the system, it is computationally efficient and convenient to express global quantities like mass and stiffness matrices using single sector quantities. In particular, the mass and stiffness matrices $\mathbf{M}$ and $\mathbf{K}$ of the entire pristine structure can be conveniently written in block diagonal form, as

$$\mathbf{M} = \begin{bmatrix} \mathbf{M}^j & & \\ & \ddots & \\ & & \mathbf{M}^j \end{bmatrix}, \quad \mathbf{K} = \begin{bmatrix} \mathbf{K}^j & & \\ & \ddots & \\ & & \mathbf{K}^j \end{bmatrix} \tag{3.2}$$

where $\mathbf{M}^j$ and $\mathbf{M}^j$ represent the mass and stiffness matrices of the pristine sector, obtained with free-interface boundary conditions at the interfaces between sectors, and duplicate nodes at those interfaces. A pristine sector is a sector of the nominal physical structure. A pristine sector can be discretized with different meshes, as shown in Figure 3.1a and Figure 3.1c. Thus, there can be multiple pristine morphed meshes, and multiple pristine modes. They all represent the same physical structure and the same physical modes, but using different meshes. Superscript j indicates the mesh index. All sector level matrices are identical when all sectors have the same mesh. Mesh $j = 0$ is the one that has not been morphed, and it is used as baseline. Mesh $j = 0$ is referred to as the un-morphed mesh. For a mistuned system, or a system with distinct meshes in every sector, the mass and stiffness matrices of

the blisk can be written as

$$\hat{\mathbf{M}} = \begin{bmatrix} {}_1\mathbf{M}^{m(1)} & & \\ & \ddots & \\ & & {}_N\mathbf{M}^{m(N)} \end{bmatrix}, \quad \mathbf{K} = \begin{bmatrix} \mathbf{K}^j & & \\ & \ddots & \\ & & {}_N\mathbf{K}^{m(N)} \end{bmatrix} \tag{3.3}$$

where ${}_i\mathbf{M}^{m(i)}$ and ${}_i\mathbf{K}^{m(i)}$ represent the sector level mass and stiffness matrices of the i^{th} sector, calculated on the $m(i)^{\text{th}}$ mesh. The mapping function $m(i)$ maps the sector index i to the corresponding mesh. Please note that a pristine system having multiple meshes (distinct in distinct sectors) is not cyclic computationally because the system matrices do not have a block circulant structure [113]. When a structure has cyclic symmetry with mesh j in all its sectors, its modes can be grouped according to their nodal diameters, and the response of the entire system can be obtained using a single sector [2]. In particular, modes appear as a single mode, or as a pair of orthogonal modes depending on the nodal diameter. To express them in terms of single sector quantities, modes $\mathbf{\Phi}^j$, $\bar{\mathbf{\Phi}}^j$ of the entire structure can be partitioned as

$$\mathbf{\Phi}^j = \begin{bmatrix} {}_1\mathbf{\Phi}^j \\ \vdots \\ {}_N\mathbf{\Phi}^j \end{bmatrix}, \quad \bar{\mathbf{\Phi}}^j = \begin{bmatrix} {}_1\bar{\mathbf{\Phi}}^j \\ \vdots \\ {}_N\bar{\mathbf{\Phi}}^j \end{bmatrix} \tag{3.4}$$

where ${}_i\mathbf{\Phi}^j$ and ${}_i\bar{\mathbf{\Phi}}^j$ represent the portion of the modes corresponding to the i^{th} sector for mesh j. Let us now consider the case of a pristine blisk having different meshes in different sectors. Such a system can be described using matrices $\hat{\mathbf{M}}$ and $\hat{\mathbf{K}}$ from Eqn. 3.2. The modes

of such a system can be written as

$$\hat{\mathbf{\Phi}} = \begin{bmatrix} {}_1\hat{\mathbf{\Phi}}^{m(1)} \\ \vdots \\ {}_N\hat{\mathbf{\Phi}}^{m(N)} \end{bmatrix}, \quad \hat{\bar{\mathbf{\Phi}}} = \begin{bmatrix} {}_1\hat{\bar{\mathbf{\Phi}}}^{m(1)} \\ \vdots \\ {}_N\hat{\bar{\mathbf{\Phi}}}^{m(N)} \end{bmatrix} \tag{3.5}$$

where ${}_i\hat{\mathbf{\Phi}}^{m(i)}$ and ${}_i\hat{\bar{\mathbf{\Phi}}}^{m(i)}$ are the i^{th} sector portion of the modes, obtained using the $m(i)^{\text{th}}$ mesh. The modes $\hat{\mathbf{\Phi}}$ and $\hat{\bar{\mathbf{\Phi}}}$ differ from the ones introduced in Eqn. 3.4 because they are composed of sector modes coming from different meshes. Please note that if the meshes are converged and pristine, then matrices $\hat{\mathbf{\Phi}}$ and $\mathbf{\Phi}^j$ represent the same physical modes, but sampled at different locations.

A ROM can be built by projecting Eqn. 3.1 onto a reduced order basis $\mathbf{T}$. This can be achieved introducing the change of coordinates

$$\mathbf{x} = \mathbf{T}\mathbf{q}, \tag{3.6}$$

where $\mathbf{q}$ is the vector containing the new set of generalized coordinates, and $\mathbf{T}$ is the reduced order basis. The new EOMs are obtained by introducing the change of coordinates and pre-multiplying by $\mathbf{T}^T$ as

$$\mathbf{T}^T\hat{\mathbf{M}}\mathbf{T}\ddot{\mathbf{q}} + \mathbf{T}^T\hat{\mathbf{K}}\mathbf{T}\mathbf{q} = \mathbf{T}^T\mathbf{F}, \tag{3.7}$$

which can be rewritten as

$$\hat{\mu}\ddot{\mathbf{q}} + \hat{\mathbf{k}}\mathbf{q} = \mathbf{f}, \tag{3.8}$$

where $\hat{\mu}$, $\hat{k}$ and f are the reduced order mass and stiffness matrices, and force vector. Writing the equations in the form presented in Eqns. 3.2-3.5 allows us to use single sector calculations

when the EOMs are projected onto the reduced order space, resulting in faster calculations.

In this paper, the focus is on geometrically mistuned blisks, and in particular on those presenting blends. For this reason, the reduction method presented in [10] is used. The details of the method are omitted here for the sake of brevity (they can be found in [10]). The overall structure of the transformation matrix can be expressed as

$$\mathbf{T} = [\mathbf{\Phi}\ \mathbf{\Psi}\ \mathbf{\Phi}_{BAM}] \tag{3.9}$$

where $\mathbf{\Phi}$ represents a set of pristine normal modes, $\mathbf{\Psi}$ represents constraint modes, and $\mathbf{\Phi}_{BAM}$ represents blend acceleration modes (BAMs), which are typically very localized modes used to accelerate convergence. The MAX method is able to deal with large blends like the one shown in Figure 3.1b. When multiple blends, and thus multiple meshes, are used, the method requires the calculation of multiple sets of pristine modes. Hence, pristine modes need to be recalculated.

3.3 Methodology

Matrices ${}_i\hat{\mathbf{\Phi}}^j$ and ${}_i\hat{\bar{\mathbf{\Phi}}}^j$ in Eqn. 3.4 can be obtained for each sector i with mesh j as a linear combination of two matrices of basis vectors ${}^n\mathbf{u}^j$ and ${}^n\bar{\mathbf{u}}^j$ as [9]

$${}^n_i\mathbf{\Phi}^j = {}^n\,\mathbf{u}^j \cos\left(\frac{2\pi n}{N}(i-1)\right) - {}^n\,\bar{\mathbf{u}}^j \sin\left(\frac{2\pi n}{N}(i-1)\right) \tag{3.10}$$

$${}^n_i\bar{\mathbf{\Phi}}^j = {}^n\,\mathbf{u}^j \sin\left(\frac{2\pi n}{N}(i-1)\right) + {}^n\,\bar{\mathbf{u}}^j \cos\left(\frac{2\pi n}{N}(i-1)\right) \tag{3.11}$$

where n denotes the nodal diameter. Matrices ${}^n_i\mathbf{\Phi}^j$ and ${}^n_i\bar{\mathbf{\Phi}}^j$ are columns of matrices ${}_i\mathbf{\Phi}^j$ and ${}_i\bar{\mathbf{\Phi}}^j$. Please note that ${}^n\mathbf{u}^j$ and ${}^n\bar{\mathbf{u}}^j$ are single sector quantities that differ for each mode pair, each nodal diameter, and each mesh. Due to the symmetry of the system, a clocked

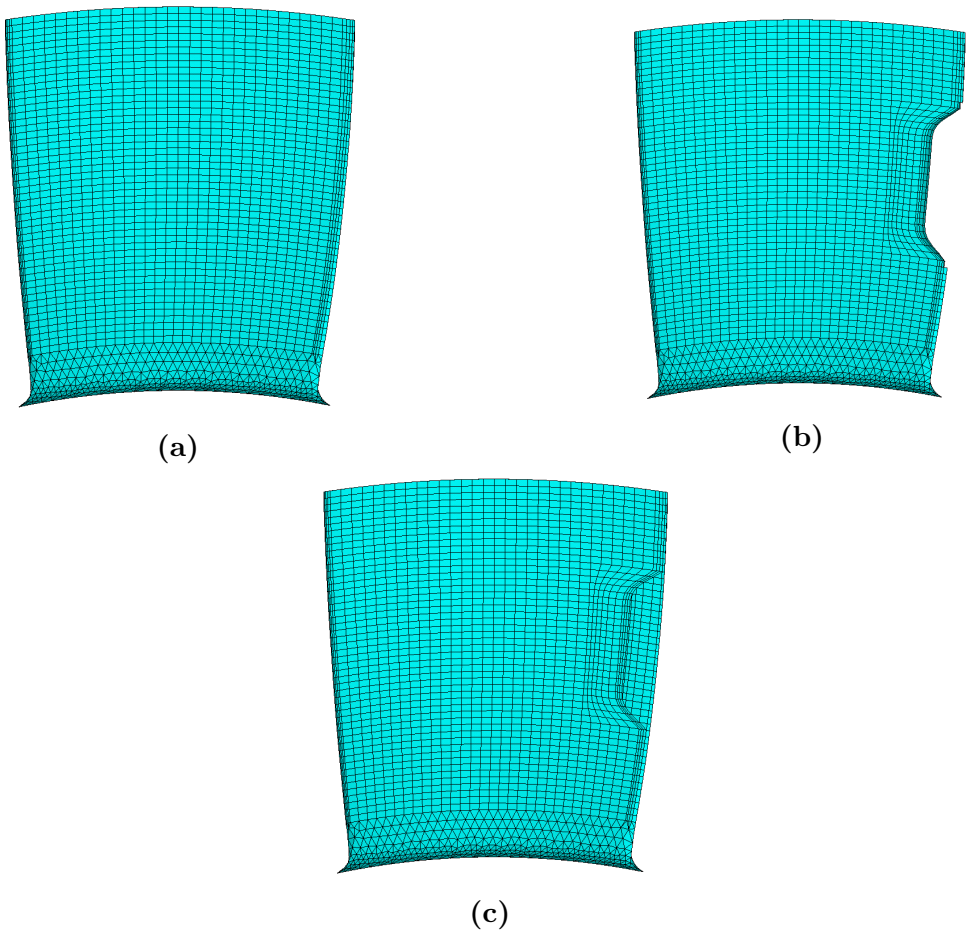

Figure 3.1: Blade meshes: a) Pristine un-morphed mesh. b) Blended mesh. c) Pristine morphed mesh.

(spatially rotated) version of an original mode pair is still a mode. Thus, cyclic modes computed independently for different meshes can present different clocking, as presented in Figure 3.2.

When multiple meshes are used, each mesh is typically associated with a set of modes, which could be clocked differently. To use such modes in the same model, consistency must be enforced, both in terms of interface compatibility and clocking. The challenge of mode clocking can be solved using an approach similar to [9]. Clocking issues can be addressed by rotating the (misaligned) basis vectors ${}^{n}\tilde{\mathbf{u}}^{j}$ and ${}^{n}\tilde{\bar{\mathbf{u}}}^{j}$ as to align them to the reference vectors, ${}^{n}\mathbf{u}^{0}$ and ${}^{n}\bar{\mathbf{u}}^{0}$ (computed for the reference mesh $j = 0$) to obtain an aligned basis ${}^{n}\mathbf{u}^{j}$ and

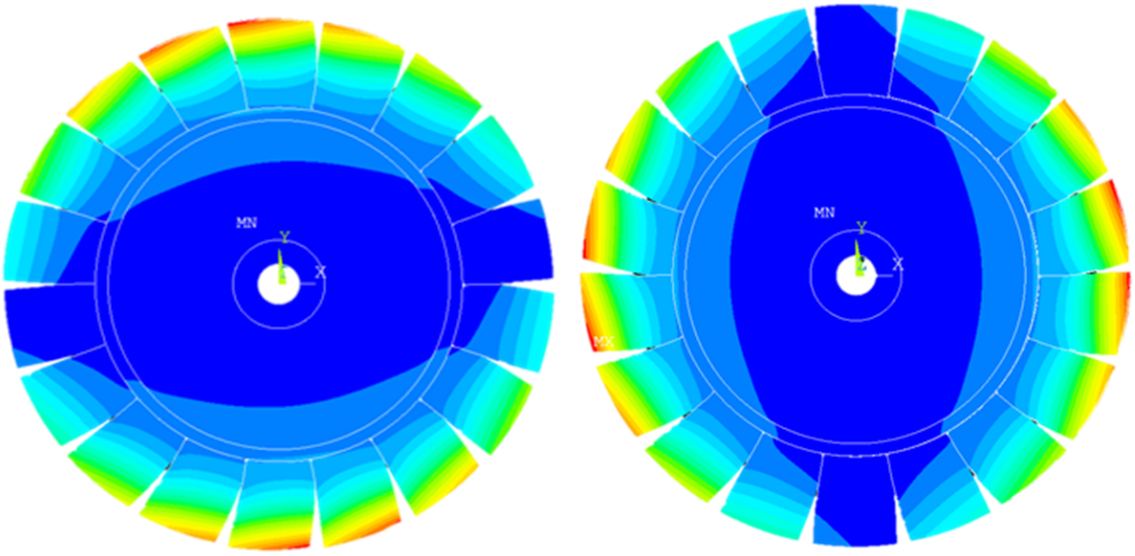

Figure 3.2: Modes of the same blisk computed on different meshes that show different clocking

${}^{n}\bar{\mathbf{u}}^{j}$. Call ${}^{n}\Phi^{j}$ the rotation angle between the two sets of vectors, which is different for each mode pair, each nodal diameter, and each mesh. The aligned vectors ${}^{n}\mathbf{u}^{j}$ and ${}^{n}\bar{\mathbf{u}}^{j}$ can be found as

$$ {}^{n}_{i}\mathbf{u}^{j} = {}^{n}\,\tilde{\mathbf{u}}^{j}\cos\left(\frac{2\pi n}{N}(i-1)\right) - {}^{n}\,\tilde{\tilde{\mathbf{u}}}^{j}\sin\left(\frac{2\pi n}{N}(i-1)\right) \tag{3.12} $$

$$ {}^{n}_{i}\bar{\mathbf{u}}^{j} = {}^{n}\,\tilde{\mathbf{u}}^{j}\sin\left(\frac{2\pi n}{N}(i-1)\right) + {}^{n}\,\tilde{\tilde{\mathbf{u}}}^{j}\cos\left(\frac{2\pi n}{N}(i-1)\right) \tag{3.13} $$

The correct rotation to be applied can be found by maximizing the projection of the misaligned vectors onto the reference vectors as

$$ \arg\max_{{}^{n}\Phi^{j}} \frac{{}^{n}\bar{\mathbf{u}}^{0} \cdot {}^{n}\,\bar{\mathbf{u}}^{j}}{|{}^{n}\bar{\mathbf{u}}^{0}||{}^{n}\bar{\mathbf{u}}^{j}|} \tag{3.14} $$

Every mode pair included in ${}^{n}\tilde{\mathbf{u}}^{j}$ and ${}^{n}\tilde{\tilde{\mathbf{u}}}^{j}$ must be rotated by the appropriate angle. The alignment can be carried out using only one vector from the pair. The other vector in the

pair is rotated by the same angle (with an adjustment factor of 1). In the results, this process is referred to as mode clocking. After clocking, the normal modes from different meshes are aligned, as shown in Figure 3.3.

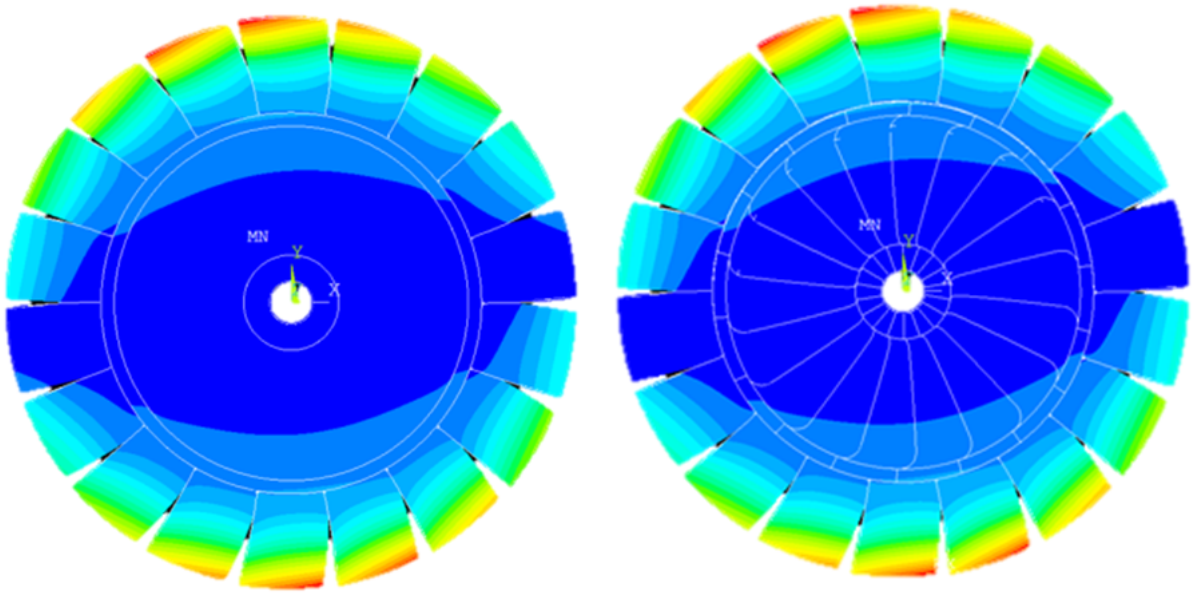

Figure 3.3: Modes of the same blisk computed on different meshes that had different clocking (as shown in Figure 3.2) but they were re-aligned

The mode clocking method can be further refined by noticing that the modal projection can be carried out on a subset of nodes. If the subset with the largest motion is chosen, the dimensionality of the vector calculations in Eqns. 3.13 is reduced without sacrificing accuracy. For example, alignment can be done neglecting the disk nodes, which usually experience much lower levels of motion compared to the blades. Incidentally, this mapping is also useful when the node numbers are different and some of the nodes are not co-located in different meshes. Nonetheless, the entire set of sector nodes is used in the results presented herein to ensure maximum accuracy. The most significant drawback of the method presented in [9] is that it only clocks the modes without ensuring correct scaling and interface compatibility. In fact, the method does not change the maximum amplitude of the mode, which

could be slightly different for each mesh, or the motion at the interface. To overcome this challenge, one can enforce the interface motion to be equal for nodes on matching surfaces at the interfaces between sectors, as suggested in [12], under the assumption that the differences in motion at the boundaries are small. Such interface nodes are shown in Figure 3.4. To preserve physical significance, the two sets of nodes on both sides of the interface must experience the same motion. Typically, interface compatibility is ensured by enforcing that the basis vectors applied to different sectors (which can be modes), present the same motion at the cyclic interface. This is automatically ensured for the vectors presented in Eqn. 3.4, but not for the ones presented in Eqn. 3.5. Modes in Eqn. 3.5 are obtained by stitching together sector-level pieces of modes calculated using different meshes in Eqns. 3.11.

Let us consider the following partition of the modes of the i^{th} sector on mesh $m(i)$ (expressed with duplicate nodes on the interfaces between sectors)

$$ {}_i\hat{\mathbf{\Phi}}^{m(i)} = \begin{bmatrix} {}^{\alpha}_{i}\hat{\mathbf{\Phi}}^{m(i)} \\ {}^{\beta}_{i}\hat{\mathbf{\Phi}}^{m(i)} \\ {}^{\gamma}_{i}\hat{\mathbf{\Phi}}^{m(i)} \end{bmatrix} \tag{3.15} $$

where the partition β represents internal nodes, while partitions α and γ represent nodes adjacent to the neighboring sectors (one on set of nodes for each side of the sector). The boundary α is adjacent to the sector having lower index, while γ is adjacent to the sector having higher index. Interface compatibility can be enforced by imposing

$$ {}^{\gamma}_{i}\hat{\mathbf{\Phi}}^{m(i)} =^{\alpha}_{i+1} \hat{\mathbf{\Phi}}^{m(i)} \tag{3.16} $$

for all sectors. This method of ensuring common displacements at the interface is referred to as interface compatibility. This method is applicable if mistuning is small, but it might not hold for larger structural variations, resulting in significant strains at the interface region.

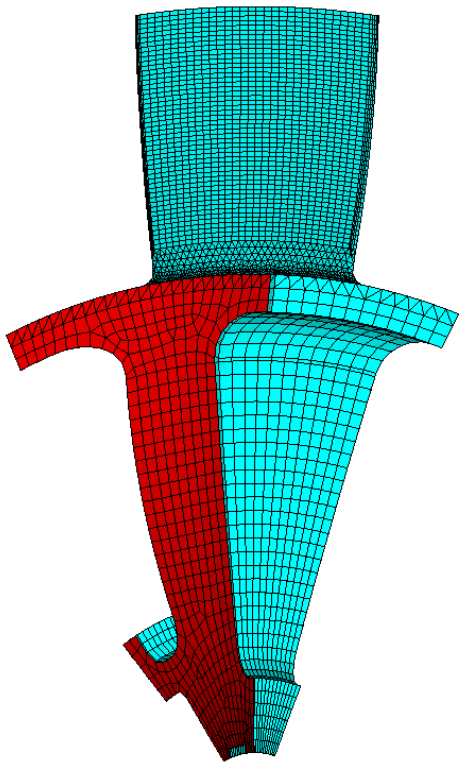

Figure 3.4: Interface nodes between sectors, highlighted

3.3.1 Pristine morphed mode extraction

The approach proposed in this paper to compute pristine morphed modes is based on the solution of a forced response problem instead of an eigen-analysis. In particular, the nodes with a one-to-one mapping on the original mesh are treated as boundary nodes forcing the structure motion. These nodes are forced to move along the un-morphed normal modes. The response is calculated for the remaining nodes. The calculation is carried out only on the morphed nodes, which in practical cases are much fewer than the total number of nodes of the entire sector, thus saving a substantial amount of computational time. The issue of scaling and cyclic interface matching is solved implicitly because the motion at the interface and at the matching nodes is imposed in the forced response calculation using the un-morphed normal modes. First, the morphed mesh is mapped onto the baseline mesh, as shown in Figure 3.5c. In this step in the algorithm, all the nodes being co-located (overlapping between

different meshes) are mapped. The nodes closer to the morphed region typically do not have a one-to-one mapping. Thus, the modal information must be recalculated for that region. The modes of the morphed mesh must be calculated to be consistent with the un-morphed modes. They should be clocked in the same way, have identical scaling, and be compatible at the cyclic interfaces. Furthermore, they should yield the same natural frequencies when used with their pristine morphed meshes. Instead of recalculating the normal modes for each mesh, it is more convenient to compute them directly based on baseline modal information. Let us consider the EOMs for a pristine free-interface single sector with mesh j, i.e. the pristine sector without constraints on the motion at the cyclic boundaries.

These EOMs can be expressed as

$$\mathbf{M}^j\ddot{\mathbf{x}}^j + \mathbf{K}^j\mathbf{x}^j = \mathbf{f}^j, \tag{3.17}$$

where $\mathbf{f}^j$ is a forcing vector applied to the sector. The vector of (response) physical degrees of freedom $\mathbf{x}^j$ can be partitioned as

$$\mathbf{x}^j = \begin{bmatrix} \mathbf{x}_O^j \\ \mathbf{x}_D^j \end{bmatrix} \tag{3.18}$$

where $\mathbf{x}_O^j$ is the vector containing the DOFs corresponding to the nodes of the morphed mesh that are overlapping the un-morphed ones, i.e. have a one-to-one mapping to the un-morphed baseline mesh $j = 0$, like the ones shown in Figure 3.5c. The vector $\mathbf{x}_D^j$ contains the remaining DOFs from the morphed region, where the nodes are distinct from the un-morphed ones.

In the overlapping area, represented by $\mathbf{x}_O^j$, the modal motion obtained from the baseline calculation can be imposed. We can thus enforce $\mathbf{x}_j^j = \mathbf{x}_O^0$. The displacement of those nodes is the same no matter what mesh is used as long as the mesh is converged in the sense that

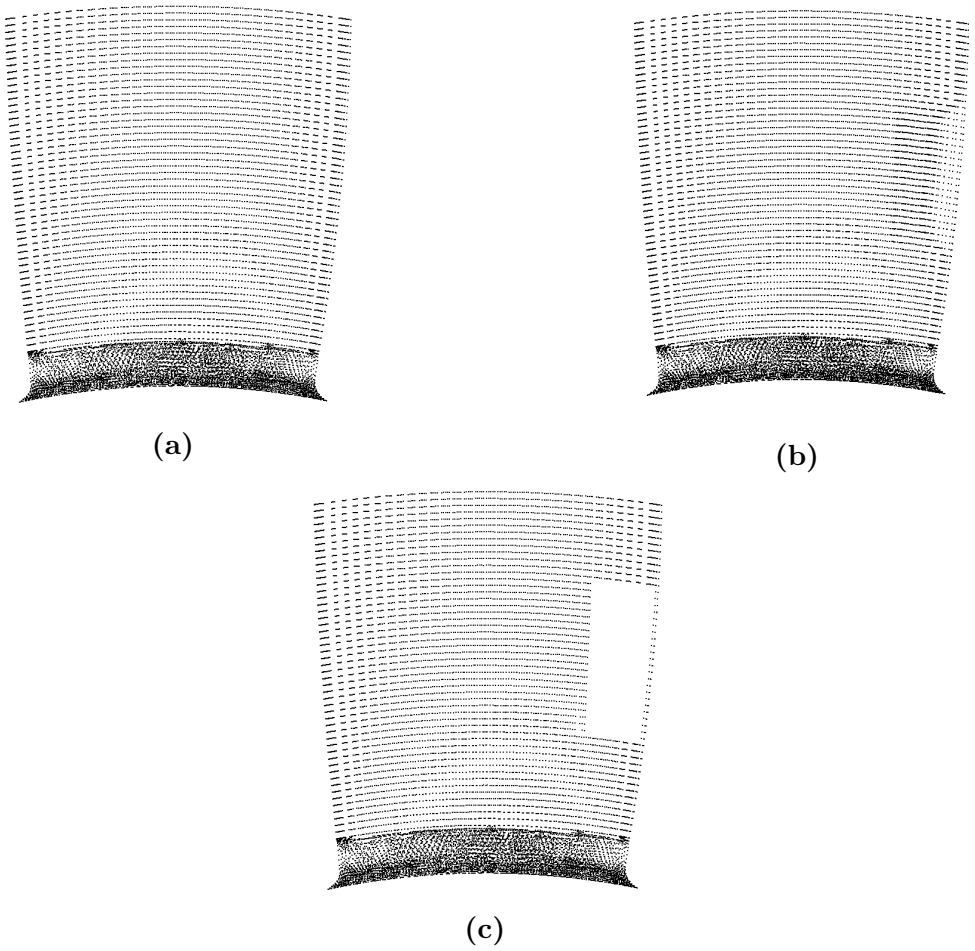

Figure 3.5: Mesh nodes for different meshes. a) Pristine un-morphed. b) Pristine morphed. c) Nodes that map (are the same) between the pristine morphed and the un-morphed meshes

the numerical discretized mode represents the physical mode. If the motion of the nodes identified as $\mathbf{x}_O^j$ is imposed as a boundary condition, we can then solve for the remaining DOFs contained in $\mathbf{x}_D^j$. For that purpose, matrices $\mathbf{M}^j$ and $\mathbf{K}^j$ can be partitioned as

$$\mathbf{M}^j = \begin{bmatrix} \mathbf{M}_{OO}^j & \mathbf{M}_{OD}^j \\ \mathbf{M}_{DO}^j & \mathbf{M}_{DD}^j \end{bmatrix}, \quad \mathbf{K}^j = \begin{bmatrix} \mathbf{K}_{OO}^j & \mathbf{K}_{OD}^j \\ \mathbf{K}_{DO}^j & \mathbf{K}_{DD}^j \end{bmatrix} \tag{3.19}$$

The EOMs in Eqn. 3.17 can be rewritten as

$$\mathbf{M}^j = \begin{bmatrix} \mathbf{M}^j_{OO} & \mathbf{M}^j_{OD} \\ \mathbf{M}^j_{DO} & \mathbf{M}^j_{DD} \end{bmatrix} \begin{bmatrix} \ddot{\mathbf{x}}^0_O \\ \ddot{\mathbf{x}}^j_D \end{bmatrix} + \begin{bmatrix} \mathbf{K}^j_{OO} & \mathbf{K}^j_{OD} \\ \mathbf{K}^j_{DO} & \mathbf{K}^j_{DD} \end{bmatrix} \begin{bmatrix} \mathbf{x}^0_O \\ \mathbf{x}^j_D \end{bmatrix} = \begin{bmatrix} \mathbf{f}^j_O \\ \mathbf{f}^j_D \end{bmatrix} \tag{3.20}$$

Note that vector $\mathbf{f}^j$ is zero at all nodes that are not mapped (free nodes, namely $\mathbf{f}^j_D = 0$), and generally non-zero at all other nodes (constrained nodes). The motion of the DOFs included in $\mathbf{x}^j_O$ is imposed and known (from the un-morphed mesh modes). Only one row of Eqn. 3.20 must be solved. Thus, Eqn. 3.20 can be rewritten as

$$\mathbf{M}^j_{DD}\ddot{\mathbf{x}}^j_D + \mathbf{K}^j_{DD}\mathbf{x}^j_D = \mathbf{f}_{\mathbf{M}}{}^j + \mathbf{f}_{\mathbf{K}}{}^j, \tag{3.21}$$

where $\mathbf{f}_{\mathbf{M}}{}^j$ and $\mathbf{f}_{\mathbf{K}}{}^j$ are the forcing terms coming from the contributions of the mass and stiffness terms due to the imposed time-dependent displacement at all mapped nodes. These forces can be expressed as

$$\mathbf{f}_{\mathbf{M}}{}^j = -\mathbf{M}^j_{DO}\ddot{\mathbf{x}}^0_O, \quad \mathbf{f}_{\mathbf{K}}{}^j = -\mathbf{K}^j_{DO}\ddot{\mathbf{x}}^0_O \tag{3.22}$$

Assuming harmonic motion at the natural frequency of the un-morphed modes, Eqn. 3.21 becomes

$$-\omega^2\mathbf{M}^j_{DD}\mathbf{x}^j_D + \mathbf{K}^j_{DD}\mathbf{x}^j_D = \omega^2\mathbf{M}^j_{DO}\mathbf{x}^0_O - \mathbf{K}^j_{DO}\mathbf{x}^0_O \tag{3.23}$$

Since the terms in Eqn. 3.23 are not time-dependent, the equation can be readily solved for $\mathbf{x}^j_D$ as

$$\mathbf{x}^j_D = (-\omega^2\mathbf{M}^j_{DD} + \mathbf{K}^j_{DD})^{-1}(\omega^2\mathbf{M}^j_{DO}\mathbf{x}^0_O - \mathbf{K}^j_{DO}\mathbf{x}^0_O) \tag{3.24}$$

Since $\mathbf{x}^0_O$ and ω^2 are derived from the un-morphed calculations, they will remain the same

for all morphed meshes, while $\mathbf{x}_D^j$ is re-calculated for each morphed mesh. This procedure is presented in Eqn. 3.24 for every mode pair and for every sector. However, this can be accomplished using sector level calculations so that the calculation does not need to be done for each and all sectors, but only for a single sector. This is done by applying Eqn. 3.24 to the mode pair basis ${}^n\mathbf{u}^j$ and ${}^n\bar{\mathbf{u}}^j$ for all nodal diameters n which can then be expanded to obtain the morphed modes $\mathbf{\Phi}^j$ and $\bar{\mathbf{\Phi}}^j$ in all sectors. Thus, the mode pairs are partitioned for each mesh as

$$z^n\mathbf{u}^j = \begin{bmatrix} {}^n\mathbf{u}_O^j \\ {}^n\mathbf{u}_D^j \end{bmatrix}, \quad {}^n\bar{\mathbf{u}}^j = \begin{bmatrix} {}^n\bar{\mathbf{u}}_O^j \\ {}^n\bar{\mathbf{u}}_D^j \end{bmatrix} \tag{3.25}$$

where ${}^n\mathbf{u}_D^j$ and ${}^n\bar{\mathbf{u}}_D^j$ are calculated for every different morphed mesh, while ${}^n\mathbf{u}_O^j$ is enforced to be equal to ${}^n\mathbf{u}_O^0$ (for un-morphed mesh) and ${}^n\bar{\mathbf{u}}_O^j$ is enforced to be equal to ${}^n\bar{\mathbf{u}}_O^0$. Thus, ${}_i\mathbf{\Phi}^j$ and ${}_i\bar{\mathbf{\Phi}}^j$ can be used instead of ${}_i\hat{\mathbf{\Phi}}^{m(i)}$ and ${}_i\hat{\bar{\mathbf{\Phi}}}^{m(i)}$ for the creation of $\hat{\mathbf{\Phi}}$ and $\hat{\bar{\mathbf{\Phi}}}$ without the need to clock them or to ensure interface compatibility, because both issues have been implicitly solved through the proposed mode extraction method. In summary, the key idea of this approach is to use the overlapping nodes, shown in Figure 3.5c, to drive the motion of the other nodes at the natural frequency of the modes, and obtain the remaining part of the modes. This method is based upon a simple physical assumption: coincident nodes should have the same motion for a given mode even for different meshes, which holds when meshes are converged. Furthermore, since the natural frequencies of the pristine morphed system are the same as the un-morphed system, the forced response problem is solved at the natural frequency of the un-morphed mode. Note that the proposed strategy ensures that the nodes at the cyclic boundaries move together. Also, from a computational cost standpoint, this technique represents a large gain, because morphing usually affects only a small portion of the entire mesh. The size of the forced response problem to be solved is thus small compared to the size of the entire sector.

3.3.2 Simplification of the projection

In the ROM creation, it is usually possible to simplify the calculations by invoking some of the properties of the basis vectors. For example, the method presented in [10] exploits the fact that when the pristine mass and stiffness matrices are projected onto normalized pristine modes, the projection assumes a very simple form. For a system having a single blend (i.e., a blend in a single sector), the ROM matrices calculated using [10] can be written as

$$\hat{\boldsymbol{\mu}} = \begin{bmatrix} \hat{\boldsymbol{\mu}}_1 & \hat{\boldsymbol{\mu}}_2 \\ \hat{\boldsymbol{\mu}}_2^T & \mathbf{I} \end{bmatrix}, \quad \hat{\mathbf{k}} = \begin{bmatrix} \hat{\mathbf{k}}_1 & \hat{\mathbf{k}}_2 \\ \hat{\mathbf{k}}_2^T & \boldsymbol{\Lambda} \end{bmatrix} \tag{3.26}$$

where $\mathbf{I}$ is the identity matrix, and $\boldsymbol{\Lambda}$ is the (diagonal) eigenvalue matrix, which contains the squared natural frequencies ω^2 of the blisk. The properties of the ROM matrices can be explained using the properties of the basis vectors in Eqn. 3.9. Recall that the modes of the system are orthogonal. Hence, for any pristine cyclic symmetric system one can write

$$\boldsymbol{\Phi}^{j^T}\mathbf{M}\boldsymbol{\Phi}^j = \sum_{i=1}^{N} {}_i\boldsymbol{\Phi}^{j^T}\mathbf{M}^j{}_i\boldsymbol{\Phi}^j = \mathbf{I} \tag{3.27}$$

$$\boldsymbol{\Phi}^{j^T}\mathbf{K}\boldsymbol{\Phi}^j = \sum_{i=1}^{N} {}_i\boldsymbol{\Phi}^{j^T}\mathbf{K}^j{}_i\boldsymbol{\Phi}^j = \boldsymbol{\Lambda} \tag{3.28}$$

While Eqn. 3.28 holds with high accuracy for a system having a single mesh, it might not hold when modes computed for multiple meshes are used. Let us consider the case in which multiple pristine meshes are present. Consider that one mesh is the un-morphed one, and several others are morphed in different ways. Recall also that the modes contain duplicate nodes at the interfaces between sectors. This duplication allows one to use Eqn. 3.3 to

describe the system matrices easily. Thus, one can write

$$\hat{\mathbf{\Phi}}^T \hat{\mathbf{M}} \hat{\mathbf{\Phi}} = \sum_{i=1}^{N} {}_i\hat{\mathbf{\Phi}}^{m(i)^T} \hat{\mathbf{M}}^{m(i)} {}_i\hat{\mathbf{\Phi}}^{m(i)} \tag{3.29}$$

The sum above should theoretically yield the identity matrix. However, even though all sectors are pristine, the sum could differ when different meshes are present in different sectors. That is because the FE representation is only an approximation of the physical blisk. This can result in the overall sum slightly deviating from the identity matrix. Thus, the identity matrix is not the most accurate to use in the ROM matrices in Eqn. 3.26. However, the entire projection does not need to be recalculated every time the mesh is changed. The new projection can be corrected. For example, let us consider for clarity a pristine system having a single pristine morphed blade (blade index $i = 1$, mesh type $j = 1$) while all the other blades are un-morphed, like the blisk shown in Figure 3.6. For the system with un-morphed meshes in all sectors, the following holds with high accuracy

$$\sum_{i=1}^{N} {}_i\mathbf{\Phi}^j \hat{\mathbf{M}}^j {}_i\mathbf{\Phi}^j = \mathbf{I} \tag{3.30}$$

For the system with a single morphed blade of blade index $i = 1$, the projection onto modes can be written as

$$\mathbf{\Phi}^T \hat{\mathbf{M}} \mathbf{\Phi} = \sum_{i=2}^{N} {}_i\mathbf{\Phi}^{0^T} \mathbf{M}^0 {}_i\mathbf{\Phi}^0 + {}_1\hat{\mathbf{\Phi}}^{1^T} \mathbf{M}^1 {}_1\hat{\mathbf{\Phi}}^1 \tag{3.31}$$

where $\mathbf{M}^0$ represents the mass matrix for the pristine un-morphed mesh, ${}_1\mathbf{M}^1$ represents the mass matrix for the pristine morphed mesh, and ${}_1\hat{\mathbf{\Phi}}^1$, ${}_i\hat{\mathbf{\Phi}}^0$ represent the modes of the pristine morphed and un-morphed mesh. Using Eqn. 3.30 with $j = 0$, Eqn. 3.31 can be

re-written as

$$\mathbf{\Phi}^T\hat{\mathbf{M}}\mathbf{\Phi} = \mathbf{I} + {}_1\hat{\mathbf{\Phi}}^{1^T}\mathbf{M}^1{}_1\hat{\mathbf{\Phi}}^1 - {}_1\hat{\mathbf{\Phi}}^{0^T}\mathbf{M}^0{}_1\hat{\mathbf{\Phi}}^0 \tag{3.32}$$

By using Eqn. 3.32 in lieu of the full wheel projection the corrected ROM matrices can be calculated

$$\hat{\boldsymbol{\mu}} = \begin{bmatrix} \hat{\boldsymbol{\mu}}_1 & \hat{\boldsymbol{\mu}}_2 \\ \hat{\boldsymbol{\mu}}_2^T & \mathbf{I} + {}_1\hat{\mathbf{\Phi}}^{1^T}\mathbf{M}^1{}_1\hat{\mathbf{\Phi}}^1 - {}_1\hat{\mathbf{\Phi}}^{0^T}\mathbf{M}^0{}_1\hat{\mathbf{\Phi}}^0 \end{bmatrix}, \quad \hat{\mathbf{k}} = \begin{bmatrix} \hat{\mathbf{k}}_1 & \hat{\mathbf{k}}_2 \\ \hat{\mathbf{k}}_2^T & \mathbf{\Lambda} + {}_1\hat{\mathbf{\Phi}}^{1^T}\mathbf{K}^1{}_1\hat{\mathbf{\Phi}}^1 - {}_1\hat{\mathbf{\Phi}}^{0^T}\mathbf{K}^0{}_1\hat{\mathbf{\Phi}}^0 \end{bmatrix} \tag{3.33}$$

The corrections in Eqn. 3.33 are computationally inexpensive because the size of the matrices is small. The sector level matrices $\mathbf{K}^0$ and $\mathbf{K}^1$ are N times smaller than the full wheel matrix $\hat{\mathbf{K}}$. Thus, when an un-morphed sector is substituted with a morphed one, we can simply correct the projected matrices using Eqn. 3.33.

3.4 Results and Discussion

A numerical study is carried out to demonstrate the proposed approach for the blisk shown in Figure 3.7. The full model of this academic blisk has 516,733 nodes, and 1,550,199 DOFs. Two of the blades are blended, and one of them is morphed also. The pristine meshes of both morphed and un-morphed blades are shown in Figure 3.1. The MAX method is used as a benchmark to explore how mesh morphing can affect the accuracy of the ROM and to investigate the effectiveness of the new solution proposed. The results are presented both with and without blend acceleration modes (BAMs). The natural frequencies of the ROM are compared to those of the full order model, with the error e being defined as

$$e = \frac{|\omega_{ROM} - \omega_{FOM}|}{\omega_{FOM}} \tag{3.34}$$

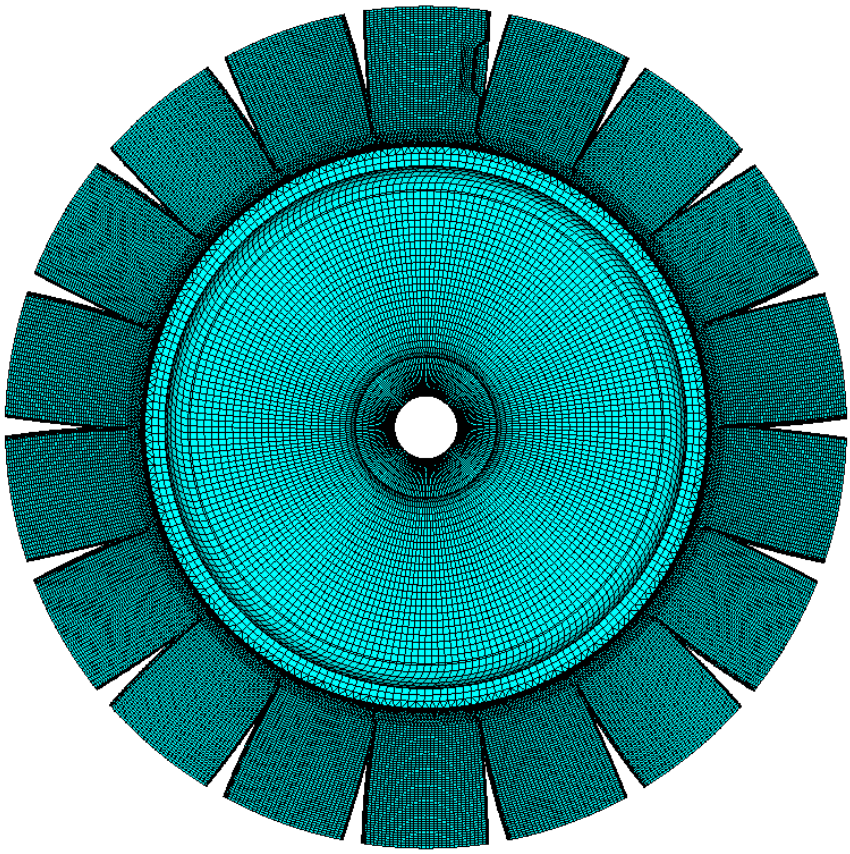

Figure 3.6: Pristine blisk with a morphed pristine mesh in one sector (sector 1)

where ω_{ROM} and ω_{FOM} are the natural frequencies obtained using the ROM and the full order model. In this section, results with modes properly aligned/clocked are presented. Modes aligned incorrectly are not examined.

Results obtained using interface compatibility techniques are presented in Figure 3.8. When the modes are not strictly enforced to satisfy the compatibility condition at the interfaces between sectors, the results are inaccurate if acceleration modes are used, as shown in Figure 3.8a. This means that the interface compatibility is not properly ensured through just mode alignment/clocking. In fact, the presence of additional basis vectors should improve the convergence when the correct matrices for the structure are used, but in this case they worsen it.

Since the formulation used to create the ROM is based on Eqn. 3.3, enforcing interface

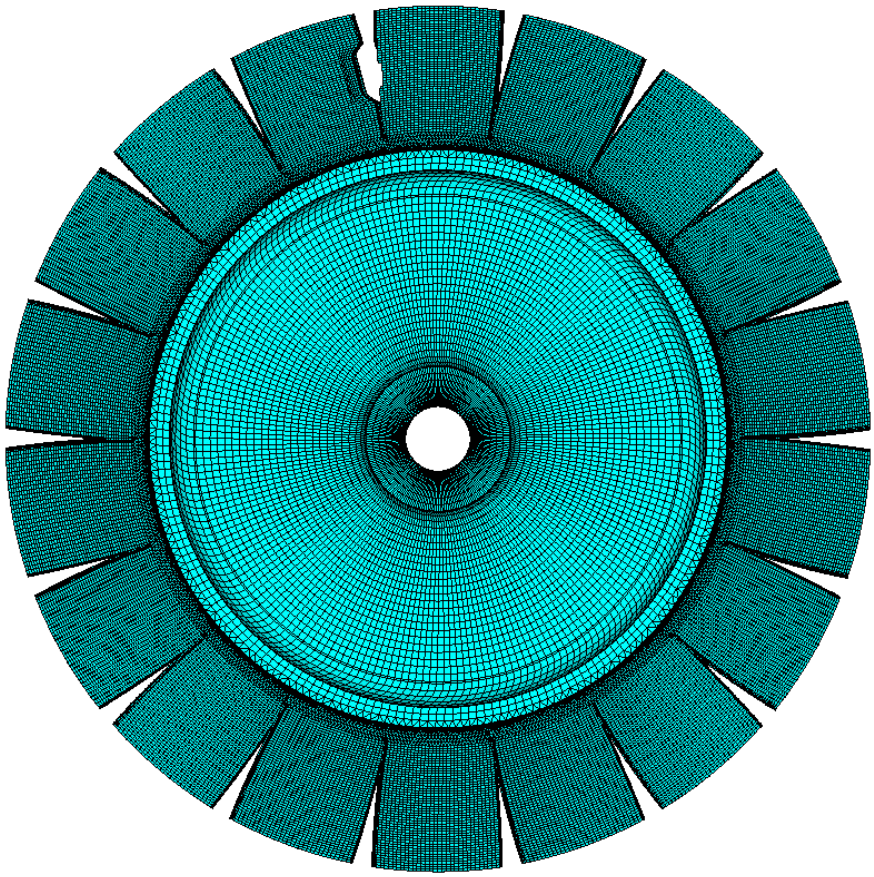

Figure 3.7: Mistuned blisk with two blended blades, one of which is both blended and its mesh morphed

compatibility through the projection modes is crucial to capture the full wheel matrices correctly. Thus, it is important to ensure compatibility very accurately. If node pair compatibility at interfaces is imposed after alignment/clocking, as shown in Figure 3.8b, there is a general improvement in accuracy, in particular with acceleration modes. However, the accuracy without the acceleration modes remains compromised. This occurs because the assumption of identical motion at the interface after alignment/clocking does not hold for highly morphed meshes. When the meshes are substantially different, their modes can have different scaling or different interface motion, which cannot be corrected effectively in a post-processing analysis. The physics of the problem must be invoked in the mode extraction phase to ensure compatibility and feasibility.

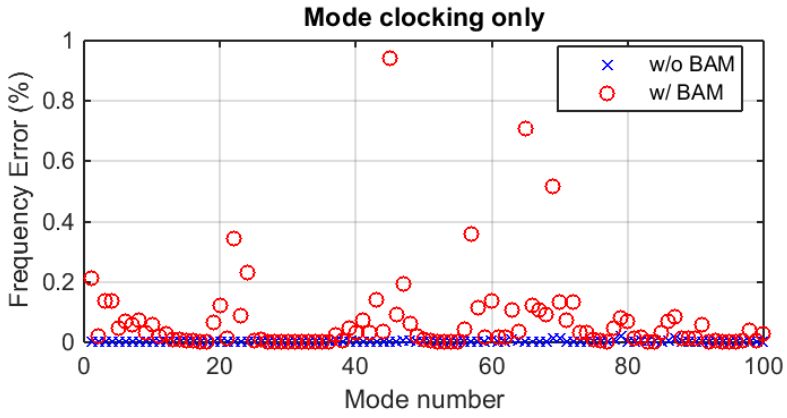

(a)

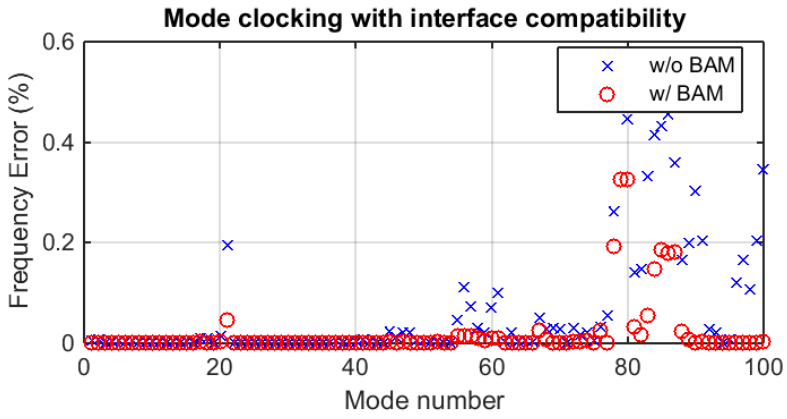

(b)

Figure 3.8: ROM vs FOM natural frequency comparison obtained using standard mode alignment/clocking and interface compatibility

In contrast, the results shown in Figure 3.9 were obtained using the new method for alignment/clocking and mode calculation on different meshes. It can immediately be noticed that there is a substantial accuracy improvement both with and without BAMs. The new method calculates sector and interface motion at the same time, implicitly ensuring interface compatibility. Furthermore, the scaling of the modes is the same.

As explained in the previous section, the introduction of a new mesh makes it necessary to correct the normal modes projection used in the ROM construction. The results obtained without the correction of the projection are presented in Figure 3.10. The approach to align/clock the modes and to ensure interface compatibility was used to obtain the solution

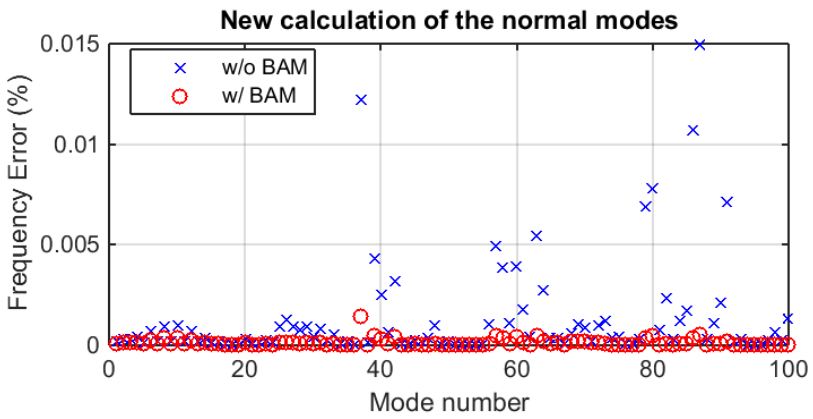

Figure 3.9: ROM vs FOM natural frequency comparison obtained using the new modal extraction method and correction applied to ROM matrices using Eqn. 3.33

shown in Figure 3.10a, while the new mode extraction method was used for the results shown in Figure 3.10b. In both cases the errors are very large, and numerical errors occur, especially when BAMs are used. That is because the ROM matrices were not adjusted. The correction in these matrices leads to the results in Figure 3.8b and Figure 3.9.

3.5 Conclusions

A novel method able to account for the presence of multiple meshes within reduced order models (ROMs) for cyclic structures was presented. The purpose of this method is to calculate the normal modes of the pristine morphed meshes and to investigate the effects that the use of multiple meshes have on the ROM. The method is based on the solution of a forced response problem, and it acts on a reduced subset of nodes, corresponding to the morphed area. The formulation is simple and cost effective, without sacrificing accuracy. Furthermore, numerical issues associated with ROM creation when multiple meshes are used were considered, and a solution was proposed. The method was applied to the case of an academic blisk for validation, and it outperformed the methods that are currently available. The results highlighted that the accuracy of the method presented here is superior to the one offered by previous alignment/clocking approaches. In addition, numerical issues

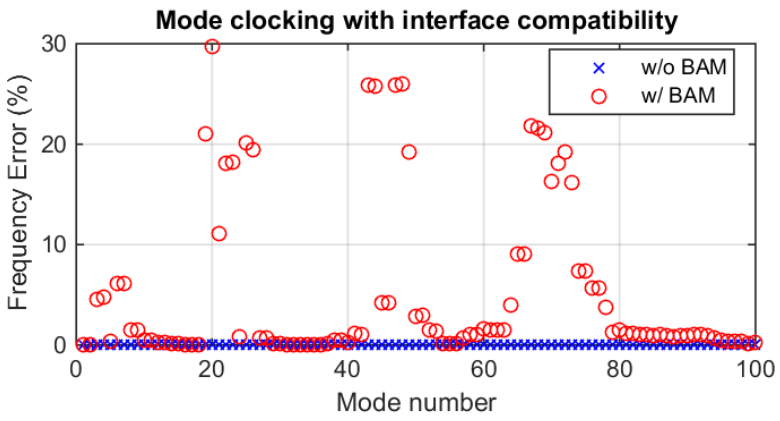

(a)

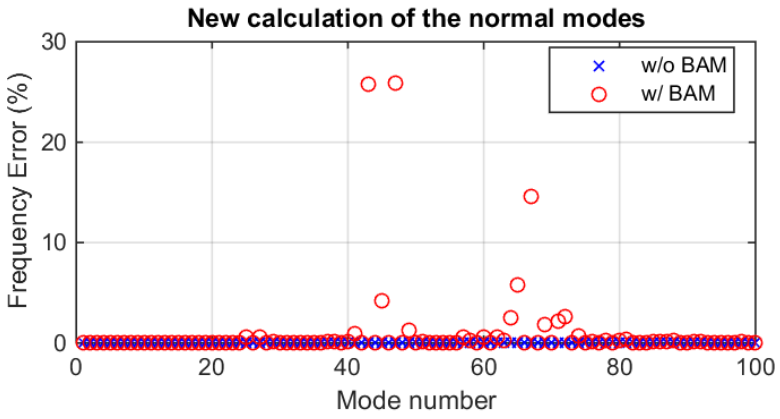

(b)

Figure 3.10: ROM vs FOM natural frequency comparison obtained without correcting the ROM matrices (i.e. without re-projection of the normal modes) for the approach based on mode clocking and interface compatibility as well as for the new calculation of the normal modes

associated with the ROM creation due to the presence of multiple meshes were solved by means of a simple correction of the ROM matrices. The method could be used to reduce the computational cost in the calculation of mistuned normal modes also. In fact, when small geometric mistuning is present, the forced response could appropriately capture the mistuned modes, further reducing the computational time and cost.

CHAPTER 4

MAX+ Modeling of Integrally Bladed Rotors

Integrally bladed rotors (IBRs) are critical components of turbomachinery in the aerospace industry. The use of IBRs has been increasing recently because they provide enhanced performance and reduced weight. One of the most significant challenges posed by IBRs is their low level of damping. The low damping leads to unwanted vibrations that increase the risk of high-cycle fatigue. In addition, IBRs are typically mistuned in real applications, i.e. they present deviations from the nominal geometry due to manufacturing tolerances, damages or wear even though they are designed to be nominally cyclic structures. Mistuning can lead to vibration localization, which further increases the risk of high cycle fatigue. Thus, the geometric design of IBRs is very important. In addition, foreign object damage can affect IBR blades during operation. Distinct from bladed disks with inserted blades, IBRs cannot have their blades replaced because IBRs are manufactured in one piece. As a result, other repair strategies must be used. IBR blades can be repaired by blending, i.e. by removing material in the damaged region to modify the local geometry as to create a smooth surface able to lower stress concentrations while also preserving satisfactory aerodynamic, structural, and vibration characteristics. Such repairs introduce large mistuning in IBRs, which can increase vibration levels. For this reason, it is necessary to optimize blend shapes and locations and to assess their impact on IBR structural dynamics. Finite element (FE) models are tradi-

tionally used to study the structural dynamics of IBRs. It is common for industrial models to have several millions of degrees of freedom per sector, making it challenging to obtain results in a timely fashion. Furthermore, the stochastic nature of mistuning requires the use of Monte Carlo simulations to evaluate the expected vibration amplitudes. For this reason, reduced-order models have been used in lieu of FE models to reduce the computational cost of such analyses. A Mode-Accelerated X-Xr (MAX) method was proposed by the authors to study the effects of such blends. In this work, enhancements to the MAX method are presented to accommodate the combined presence of blends and that of other effects, such as blade frequency mistuning and prestress due to centrifugal forces. The use of multiple FE meshes in a single model is also addressed, making it possible to accommodate the use of morphed meshes to better capture the geometry of blended sectors. This enhanced MAX method, referred to as MAX+, is presented. MAX+ is validated by comparing its predictions to high-fidelity FE models, and it is shown to be efficient and effective for simulating blended IBRs in both bench and rotating conditions. Furthermore, the MAX+ approach can be used for the optimization of blend shapes, locations, and patterns when multiple blends are present.

4.1 Introduction

Integrally bladed rotors (IBRs), also known as blisks, are structures commonly used in gas turbine engines. These components are nominally cyclic symmetric, a feature that can be exploited to significantly reduce the computational cost associated with structural and vibration analysis [2]. However, due to manufacturing tolerances, wear, and damages, the symmetry of the nominal structure is not found in real IBRs. Any deviation from nominal conditions is referred to as mistuning. Due to the presence of mistuning, predictions based on cyclic models are not accurate because localization phenomena can appear, resulting in

substantial variations in the forced response [4]. Furthermore, IBRs have very low damping due to the absence of frictional contacts and joints. This can result in large vibration amplitudes in one or more blades, which can lead to high cycle fatigue and ultimately blade failure especially because vibrations are combined with high levels of static stress due to centrifugal forces and blade aerodynamic loading. For this reason, it is extremely important to study the vibration characteristics of IBRs taking into account the effects of mistuning. IBRs are commonly studied using highly refined finite element (FE) models, which can provide an excellent level of detail but also a significant computational cost. Due to the stochastic nature of mistuning, it is necessary to perform Monte Carlo simulations to explore the entire range of expected responses [4]. This is unfeasible when large FE models are used. Thus, other modeling techniques are commonly used to reduce the computational cost. The use of reduced order models (ROMs) for the extraction of modal and structural information is common practice both in industry and academia. Researchers have extensively studied in the past the effects of mistuning on the dynamics of IBRs using ROMs [4]. Many of these studies focus in particular on geometric mistuning [9, 11, 13]. An interesting type of geometric mistuning is that created by blends [10], i.e. material removal, for the repair of cracked or damaged IBRs. Such repairs need to be carefully designed so that they have minimal impact on the vibration of the repaired IBRs. For this reason, ROMs [10, 114] have been created for the analysis and optimization of such repairs. The Mode-Accelerated X-Xr (MAX) method presented in [10] is particularly adapt to model such effects. MAX accounts for blade frequency mistuning (caused by stiffness or mass mistuning in the blade) using component mode mistuning (CMM) [30]. However, other aspects need to be considered, such as the fact that geometric mistuning can present a significant interaction with centrifugal loading and other sources of prestress. Turbomachinery components typically operate in very demanding conditions. As such, blades must withstand significant static and dynamic stresses, due to both aerodynamic loads and centrifugal forces, which can vary depending

on the operating conditions. The operating conditions at which the system is excited have a significant impact on the response. For example, rotational effects as well as aeroelastic effects have been shown to have an important role on the vibration characteristics of the system [5, 35–38]. In rotating conditions, the blades experience significant spin softening and stress stiffening, which ultimately change the natural frequencies and modal characteristics. The thermo-mechanical aspects of the system can play a significant role in the IBR life cycle also [39]. The effects of the non-time-varying components of all these phenomena on the IBR can be described using prestress. The introduction of centrifugal effects, a typical source of prestress, can be accommodated in ROMs. The general problem of cyclic rotating structures is tackled in [40, 41] using cyclic symmetry together with component modes synthesis [42]. Non-rotating mode shapes are used to project the equations of motions onto a reduced set of coordinates. Some of the effects that arise when mistuning is combined with the effects of rotation are investigated in [43–45]. In [43] the effects of mistuning are studied using a set of basis vectors that adequately spans the interface motion between sectors. That method ensures the compatibility condition at the interface, but it also requires an extra set of modes to be computed. The method was extended also to a range of variable rotation speeds using parametric techniques. In [44, 45] a study on cracks and Coriolis effects in rotating disks is presented, without dealing with the compatibility condition at the interface that is of interest here. In [46] a study on the effect of prestress can be found, focusing in particular on the presence of contact forces, but without dealing with geometric mistuning. The effects of rotational speed can be captured as variations in the stiffness matrix, as suggested by previous studies for the blade part only [36]. When it comes to model order reduction, another such solution is to use parametric ROMs [47, 112]. However, many parametric ROMs are not the most efficient for IBRs because they require the calculation of multiple sets of modes, and because of possible numerical instabilities of the transformation matrix [20, 47, 112]. Even more importantly, the calculation of prestress

effects on the stiffness matrix of a mistuned IBR requires full wheel analyses, which are often computationally cumbersome. None of the studies cited above focuses on the efficient extraction of the prestressed matrices for a mistuned system, and little attention is given in the literature to modeling of non-cyclic prestress. The use of FE mesh morphing has become common because it allows for easy changes in the shape of FE models without requiring a new meshing step. This is particularly useful for IBRs with one blended blade, where the blend only affects a small portion of the entire full wheel model. Several studies have been conducted on this topic to understand the implications of FE mesh morphing on ROMs created using the MAX method [114].

In this paper, the focus is on the creation of a comprehensive method that can be used in the creation of ROMs where blended IBRs need to be analyzed and optimized in the concurrent presence of mistuning and prestress. MAX+ is the result of the integration of previous work from the authors, in particular the MAX method [10], a numerical conditioning technique [112] and a study on the use of mesh morphing in ROMs [114]. In addition, we present a technique able to capture prestress effects that can be implemented in MAX+. This approach only requires single sector calculations for the extraction of the free-interface sector-level tuned and mistuned matrices at different rotational speeds. The prestress is calculated for every type of mistuned blade at the sector level, thus capturing mistuning effects that could potentially be greatly magnified by the action of centrifugal or steady aeroelastic forces, without the need of a full wheel analysis. The MAX method is used to treat the effects of large blends, and it is extended by introducing prestress effects on the matrices and by treating rotational effects as small mistuning. For further computational savings, MAX+ can be used together with parameterization of the stiffness variation [37] to obtain mistuned results more readily. Numerical results are presented to demonstrate the effectiveness of the approach.

4.2 Background

IBRs are structures that are nominally cyclic symmetric, i.e. they are composed of identical sectors that are repeated in space by rotation around a common axis. Figure 4.1 presents an example of such a structure.

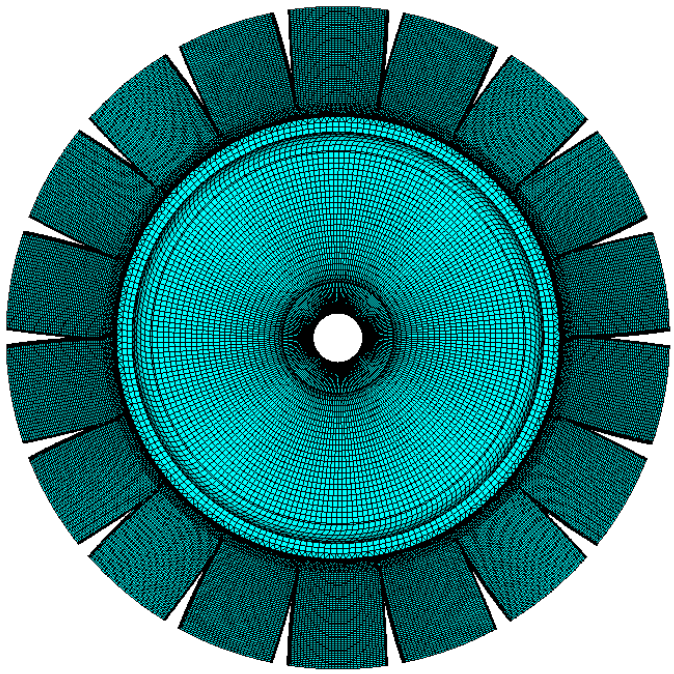

Figure 4.1: Perfectly symmetric and tuned IBR

The mass and stiffness matrices of an entire cyclic structure assume circulant form [113]. However, for the creation of ROMs it is typically more convenient to manipulate sector level quantities. The free-boundary sector level matrices can be used to describe the system. This requires that the degrees of freedom (DOFs) at the interface between sectors be duplicated, and that interface compatibility be enforced. An IBR sector is shown in Figure 4.2, with one of the cyclic interfaces highlighted. A more detailed explanation of the concept of cyclic interfaces is provided in Section 4.3.3.

Using a decoupled approach like the one presented in [9], it is possible to write the system

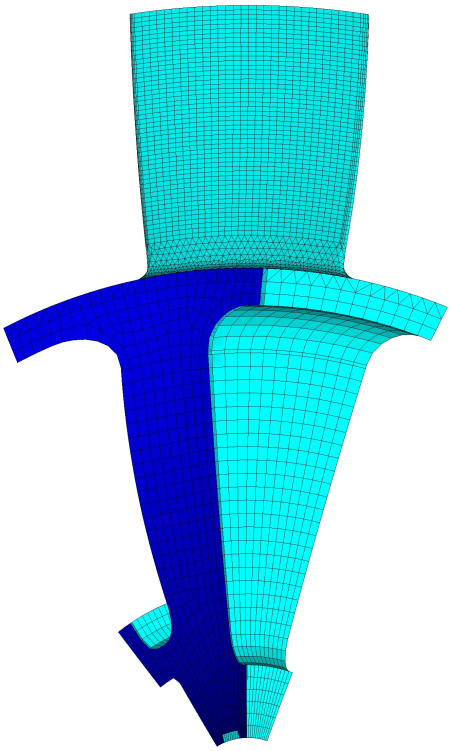

Figure 4.2: *Pristine* sector with cyclic interface highlighted in blue

level mass and stiffness matrices as block diagonal, where the diagonal elements are the free-interface matrices of each sector. The coupling is enforced through compatibility equations on the boundary nodes. For a tuned system, the system level matrices can be expressed using a Kronecker product where only sector level quantities are introduced. For example, the mass matrix $\tilde{\mathbf{M}}$ of the entire pristine structure can be written as

$$\tilde{\mathbf{M}} = \mathbf{I} \otimes \mathbf{M} = \begin{bmatrix} \mathbf{M} & & \\ & \ddots & \\ & & \mathbf{M} \end{bmatrix}, \tag{4.1}$$

where the matrix $\mathbf{M}$ represents the free-interface level matrix. In a mistuned system, like the one presented in Figure 4.3, the sectors are in general different, and thus the Kronecker product cannot be used anymore. The full wheel matrix of a mistuned system becomes more

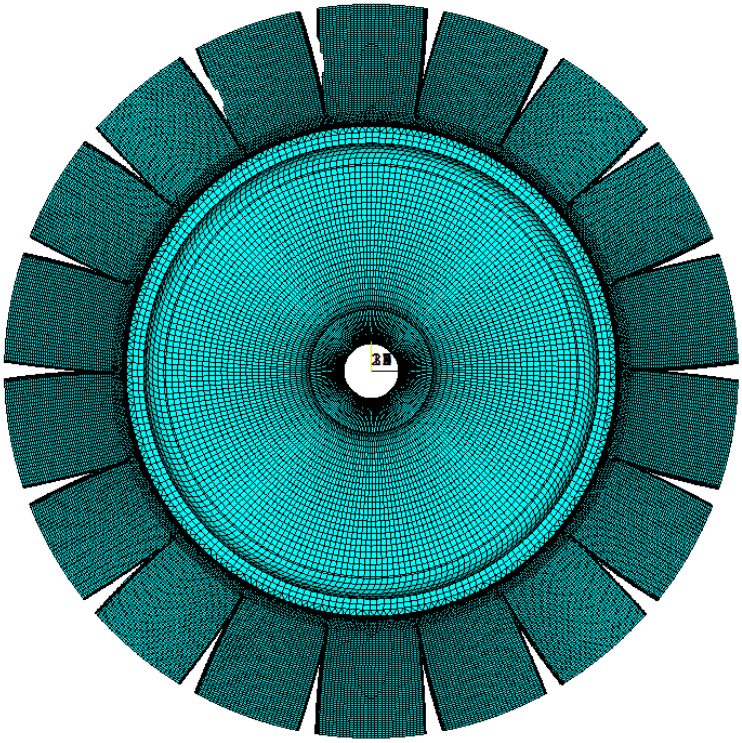

Figure 4.3: Geometrically mistuned IBR

generally

$$\tilde{\mathbf{M}} = \begin{bmatrix} \mathbf{M}_1 & & \\ & \ddots & \\ & & \mathbf{M}_N \end{bmatrix}, \tag{4.2}$$

where the matrices $\mathbf{M}_i$ of each of the N sectors could potentially be different.

To better explore the impact of this on the ROM creation it is important to recall the concept of *pristine* and *mistuned* sectors. *Pristine* sectors present nominal geometry and properties. This can also include systems subject to prestress that preserve cyclic symmetry. *Mistuned* sectors show instead any deviation from the cyclically symmetric ones. For example, let us consider an IBR composed of pristine sectors. After centrifugal loads are applied, it is still composed of pristine sectors. That is not the case for an IBR showing mistuning

in one of its blades. A single mistuned sector is sufficient to convert all pristine sectors into mistuned sectors when prestress is applied. The prestress applied is non-cyclic. Thus, the resulting equilibrium is mistuned in all sectors as well.

Typically, only few sectors are mistuned. Let us now assume that only the first sector is mistuned, with a mistuned mass matrix $\mathbf{M}_m$, while all the other sectors are pristine, with mass matrix $\mathbf{M}$. Equation 4.2 simplifies to

$$\hat{\mathbf{M}} = \begin{bmatrix} \mathbf{M}_m & & & \\ & \mathbf{M} & & \\ & & \ddots & \\ & & & \mathbf{M} \end{bmatrix}. \tag{4.3}$$

The sector level matrices, as well as the mode shapes of the system can be readily obtained using commercial FE software. Note that in the absence of prestress even the mistuned sector matrices can be obtained using a single sector calculation, as there is no equilibrium compatibility required.

4.3 Methods

4.3.1 Reduced order model creation

Let us consider the general case of a mistuned IBR (a tuned IBR can be seen as a particular case with zero mistuning). The equation of motion for the structural dynamics of the IBR can be written as

$$\hat{\mathbf{M}}\ddot{\mathbf{x}} + \hat{\mathbf{K}}\mathbf{x} = \mathbf{f}, \tag{4.4}$$

where $\hat{\mathbf{M}}$ is the mass matrix, $\hat{\mathbf{K}}$ is the stiffness matrix, and $\mathbf{x}$ and $\mathbf{f}$ are the vectors of generalized coordinates and forces respectively for the entire IBR. A ROM can be created by introducing the change of coordinates $\mathbf{x} = \mathbf{Tq}$,where $\mathbf{T}$ is the transformation matrix and

$\mathbf{q}$ is the vector of generalized coordinates. The system level matrices $\hat{\mathbf{M}}$ and $\hat{\mathbf{K}}$ presented in Eq. 4.4 can be prohibitively large to store and to use. For this reason it is often more convenient to use sector level matrices for the calculation of the ROM. The formulation presented in Eq. 4.2 requires coupling between the sectors. This coupling is provided through the basis vectors included in the transformation matrix $\mathbf{T}$. Using sector level quantities instead of system level ones results in significant savings of computational time and memory. In this case, the system level multiplication with the transformation matrix results in a sum over the sectors of sector level information as in

$$\mathbf{T}^T\hat{\mathbf{M}}\mathbf{T} = \sum_{i=1}^{N} \mathbf{T}_i^T\mathbf{M}_i\mathbf{T}_i, \tag{4.5}$$

where $\mathbf{T}_i$ is the partition of the transformation matrix corresponding to the i^{th} sector. The MAX transformation matrix matrix can be written as [10]

$$\mathbf{T} = \begin{bmatrix} \mathbf{\Phi}_{MCM} & \mathbf{\Phi}_{BAM} & \mathbf{\Phi} \end{bmatrix}, \tag{4.6}$$

where, $\mathbf{\Phi}_{MCM}$ represents the constrained modes, $\mathbf{\Phi}_{BAM}$ the acceleration modes, and $\mathbf{\Phi}$ the normal modes. If the number of sectors is large, then it is important to implement this calculation efficiently in the ROM creation process. In MAX+, the transformation matrix includes tuned normal modes, and as a result the properties of cyclic structure can be invoked. Using a technique similar to the one proposed in [13], it is possible to greatly reduce the number of operations to be carried out. Let us now consider the multiplication of the system level matrices with the normal modes. Equation 4.5 can be expressed as

$$\mathbf{\Phi}^T\hat{\mathbf{M}}\mathbf{\Phi} = \sum_{i=1}^{N} \mathbf{\Phi}_i^T\mathbf{M}_i\mathbf{\Phi}_i. \tag{4.7}$$

The tuned normal modes at the system level can be expressed as a linear combination of the vectors $\mathbf{u}$ and $\bar{\mathbf{u}}$ as [9]

$$\mathbf{\Phi}_i = \mathbf{u}\mathbf{f}_{\mathbf{Ai}} + \bar{\mathbf{u}}\mathbf{f}_{\mathbf{Bi}}, \tag{4.8}$$

where $\mathbf{f_A}$ and $\mathbf{f_B}$ are the coefficients of the real Fourier matrix. Introducing this notation and plugging back into Eq. 4.8 it can immediately be noticed that only the coefficients change over different sectors, the other quantities remain the same. This feature makes this calculation feasible for highly refined industrial FE models, where the number of DOFs often exceeds several million per sector and the number of blades can be very large.

4.3.2 Interaction of mistuning and prestress

The focus of this paper is set on the part of MAX+ able to capture prestress effects, i.e. effects that encompass steady state variations in the stiffness and/or the mass matrices. Even though the mass matrix is typically not affected, it could experience small variations if a nonlinear analysis is carried out to obtain the new static equilibrium. The examples presented here refer to centrifugal loads, but the prestress term could come from other sources, such as steady thermal and aeroelastic loads. In particular, this study is concerned with the interaction between mistuning and prestress effects, with a particular focus on geometric mistuning. The presence of a blend is used as an example of geometric mistuning.

Let us now consider the case of the perfectly symmetric IBR shown in Figure 4.1. When in rotating conditions, all sectors experience the same forcing, as shown in Figure 4.4, and thus the equilibrium position still preserves its symmetry. As a result, cyclic symmetry analysis can be employed to solve for the equilibrium and extract the sector level matrices in rotating conditions. The system matrices can still be conveniently written in the same

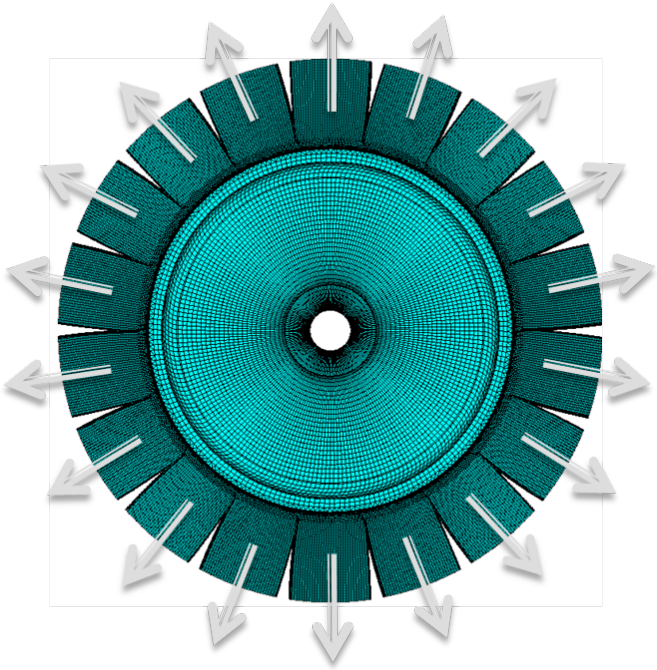

Figure 4.4: Pristine system subject to preload

form as Eq. 4.1. In particular, the stiffness matrix can be written as

$$\tilde{\mathbf{K}}_\Omega = \mathbf{I} \otimes \mathbf{K}_\Omega = \begin{bmatrix} \mathbf{K}_\Omega & & \\ & \ddots & \\ & & \mathbf{K}_\Omega \end{bmatrix}, \tag{4.9}$$

where the subscript Ω is added to represent the presence of prestress. However, these assumptions are not valid when geometric mistuning is present, like in the case shown in Figure 4.5. In that case, the sectors experience different forces, as shown in Figure 4.5, resulting in a final equilibrium position that is not cyclic symmetric. The difference between *pristine* and *mistuned* sectors of a mistuned IBR ceases to exist when prestress is applied, as all the sectors become *mistuned* to a certain extent.

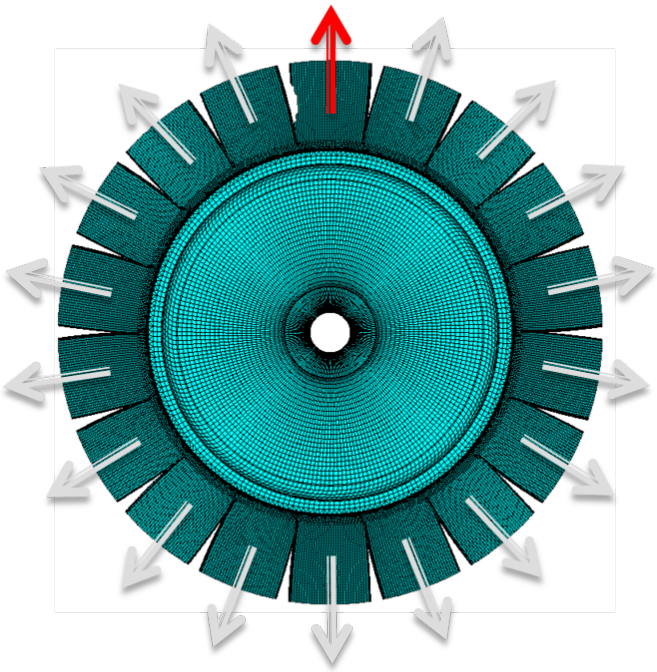

Figure 4.5: Mistuned system subject to preload

The change in stiffness due to prestress can be expressed as

$$\delta\tilde{\mathbf{K}}_{\Omega} = \begin{bmatrix} \delta\mathbf{K}_1 & & \\ & \ddots & \\ & & \delta\mathbf{K}_N \end{bmatrix}, \tag{4.10}$$

where $\delta\mathbf{K}_i$ is the prestress contribution to the i^{th} sector. A mistuned IBR composed of both *pristine* and *mistuned* sectors in static conditions becomes instead composed of only *mistuned* sectors when subject to prestress. Thus, the concept of *pristine* sector disappears when any form of mistuning and preload are concurrently present. In fact, especially in proximity of the mistuned sector, a significant deviation from cyclic symmetry can be observed. In this paper, a calculation strategy for the extraction of the sector level matrices is presented to re-establish the concept of *pristine* sector, with the aim of reducing the computational cost

with little accuracy loss.

4.3.3 Calculation of the prestressed matrices

When a mistuned IBR like the one shown in Figure 4.5 is subject to a preload, a full wheel analysis is required for the extraction of the new system matrices. This requires significant computational effort and eliminates properties that are very useful for the ROM creation, such as the existence of *pristine* sectors. In the method proposed here, the full wheel static equilibrium is substituted with single sector calculations. This is based on the assumption that *pristine* sectors remain *pristine*.

First, the static equilibrium for the pristine sector is obtained using cyclic symmetry analysis. Then, the resulting displacements at the cyclic interface highlighted in Figure 4.2 are imposed as boundary conditions for the *mistuned* case. The prestress loads are then applied to the sector and the equilibrium for the *mistuned* sector calculated. All these analyses are performed using single sector calculations. The underlying assumption is that the deviation from the cyclic prestress is localized in the blend or blade region, which is far from the cyclic interface. Thus, a negligible error is committed by imposing an approximated boundary condition at the cyclic interface.

4.3.4 Metrics and limitation

The effectiveness of the method is based upon the assumption that there exists a region far enough from the geometrically mistuned area where the deviation from cyclic results is negligible. The presence of such a region is strongly dependent on both *pristine* and *mistuned* geometries, as well as the rotational speed or prestress level. In fact, the magnitude of the error will depend on all these factors.

An error metric is introduced to evaluate the magnitude of the error. This metric is able to quantify the deviation between single sector and full wheel results in the sectors adjacent

to the blended one. A full wheel calculation must be carried out only once for a given mistuning type (e.g., type of blend), typically at the highest level of prestress expected. If the error is considered acceptable, it is then possible to use the matrices extracted in the ROM. First, the *pristine* prestressed full wheel stiffness matrix $\tilde{\mathbf{K}}$ is obtained. Then, one of the sectors is substituted with the *mistuned* sector under investigation to obtain the *mistuned* prestressed full wheel stiffness matrix $\hat{\mathbf{K}}$. Once the full wheel matrices are obtained, the prestress deviation matrix $\mathbf{K}_{var}$ can be formulated as follows

$$\mathbf{K}_{var} = |\hat{\mathbf{K}} - \tilde{\mathbf{K}}|. \tag{4.11}$$

For convenience, the results can be visualized by assigning a measure of the variation in the stiffness matrix entries to every DOF. Recalling that the deviation matrix and the vector of DOFs are defined as $\mathbf{K}_{var} = \left(k_{var_{ij}}\right)$, $\tilde{\mathbf{K}} = \left(\tilde{k}_{ij}\right)$ and $\mathbf{x} = (x_i)$ respectively, one can write

$$x_i = \frac{\sum_{j=1}^{N} k_{var_{ij}}}{\sum_{j=1}^{N} |\tilde{k}_{ij}|}. \tag{4.12}$$

This approach quantifies the impact that a *mistuned* sector has on a neighboring *pristine* sector.

4.4 Results and Discussion

Let us consider the IBR shown in Figure 4.6. The first sector presents a large blend. The MAX method [10] is used to create a ROM. The natural frequencies of the ROM are compared to the ones obtained using the full-order model to validate the method. For each mode, the error is defined as

$$e = \frac{|\omega_{ROM} - \omega_0|}{\omega_0}, \tag{4.13}$$

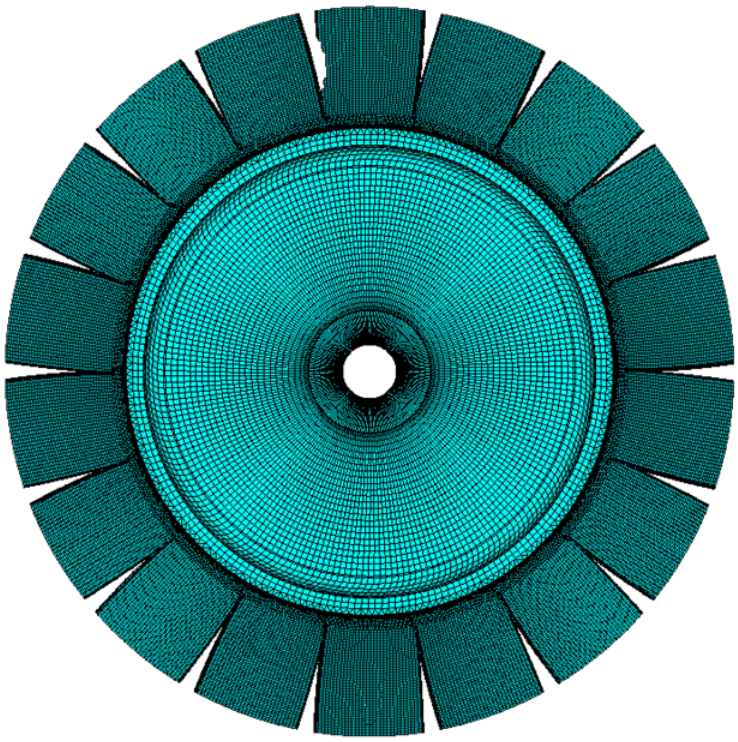

Figure 4.6: Validation IBR having one blended blade

where ω_0 represents the frequency obtained using the full-order model, and ω_{ROM} represents the frequency calculated using the ROM.

A baseline set of results can be obtained using a full order model for the IBR shown in Figure 4.6 and used for validation. Results obtained using the ROM in non-rotating conditions are presented in Figure 4.7a. Note that the two sets of results are in good agreement, showing an almost negligible error. Establishing a baseline is important because the accuracy of the ROM in rotating conditions is expected to decrease due to the simplifications made during ROM creation. The error will depend on the blend size and type, and on the magnitude of the prestress. In all the results here presented, the transformation matrix from the MAX method is modified to include the normal modes in prestressed conditions.

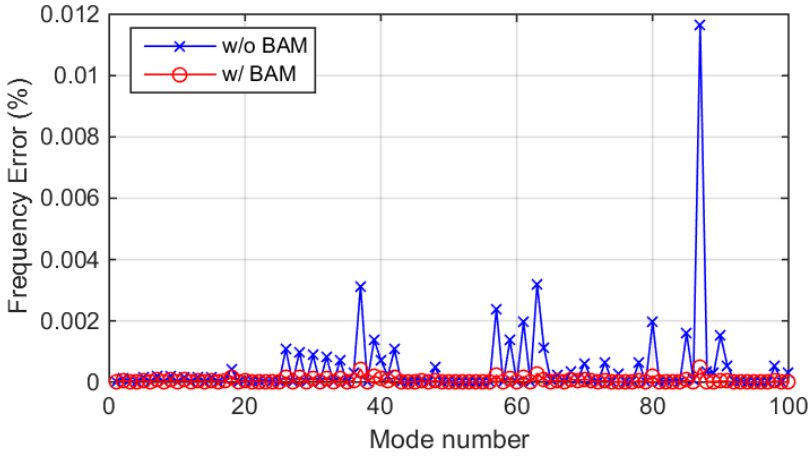

(a) Baseline MAX results without prestress

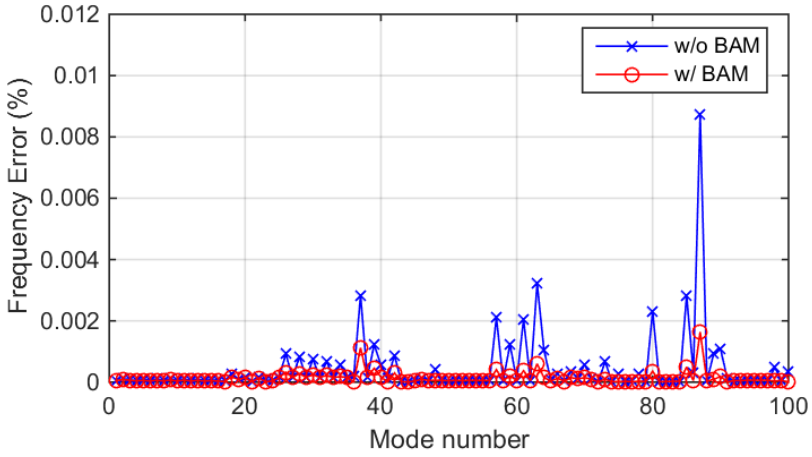

(b) MAX+ results in rotating conditions at 10000 RPM

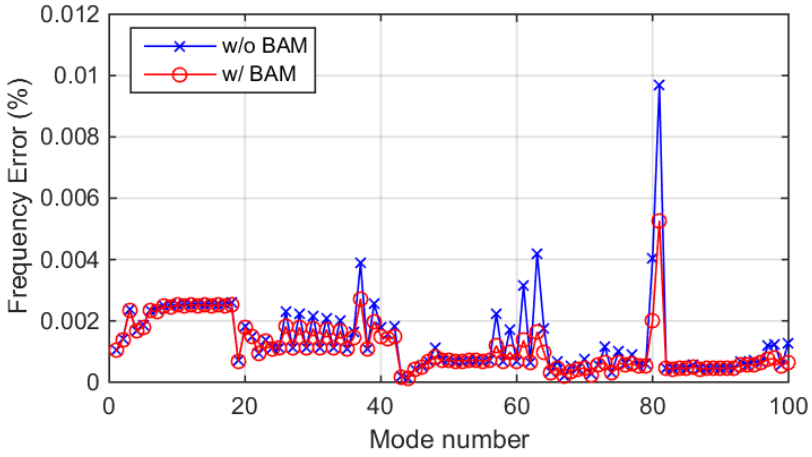

(c) MAX+ results in rotating conditions at 20000 RPM

Figure 4.7: Validation results obtained in different prestress conditions

Figure 4.7b shows the frequency error for the case of an IBR spinning at 10000 RPM. Note that the accuracy loss compared to the baseline results is negligible. The accuracy loss becomes noticeable in the case of a rotor spinning at 20000 RPM, as can be seen in Figure 4.7c. In particular, it is important to note that the blend acceleration modes (BAMs) coming from the MAX method are not able to reduce the error. This is because the mass and stiffness matrices are the sources of error. Nonetheless, MAX+ prediction error is still small.

The error due to the use of single sector calculations can be visualized using the metric presented in Section 4.3.4. Figure 4.8 shows a visualization of the stiffness variation matrix $\mathbf{K}_{var}$ for the 20000 RPM case. Figure 4.8a show that the largest variation is localized in the blended sector. This is expected, and it is appropriate to obtain a deviation in the area adjacent to the blend. Particularly relevant is Figure 4.8b, which shows the error that is committed by neglecting the stiffness variation in the neighboring sectors, which are assumed to remain *pristine* instead. In this case, the maximum deviation is 0.007%. Please note that a small error is also committed in the blended sector due to the application of approximate boundary conditions. This error is not represented here because it is not captured by this metric.

The case of the IBRs with two blends on neighboring blades [112] shown in Figure 4.3 is examined next. The presence of two neighboring blends is more challenging to capture because they can mutually influence each other when prestress is applied. The results obtained in rotating conditions at 10000 RPM are shown in Figure 4.9b, while the baseline results obtained in absence of prestress are shown in Figure 4.9a. Even in this case, the MAX+ method provides excellent accuracy.

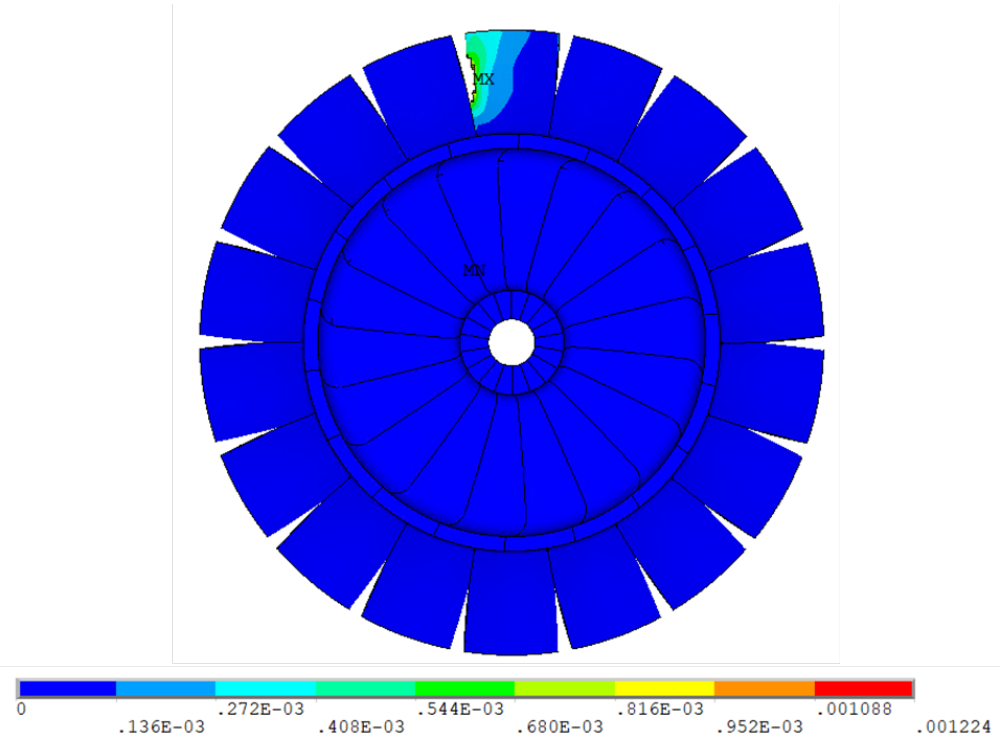

(a)

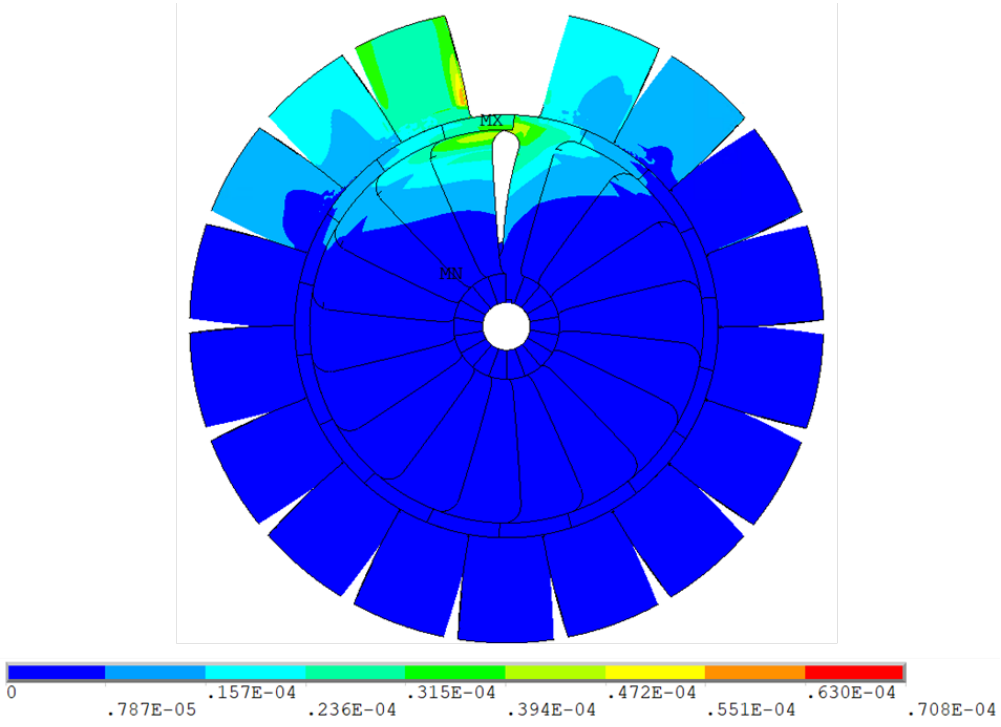

(b)

Figure 4.8: Visualization of the error metric between the prestressed *pristine* and *mistuned* stiffness $\mathbf{K}_{var}$

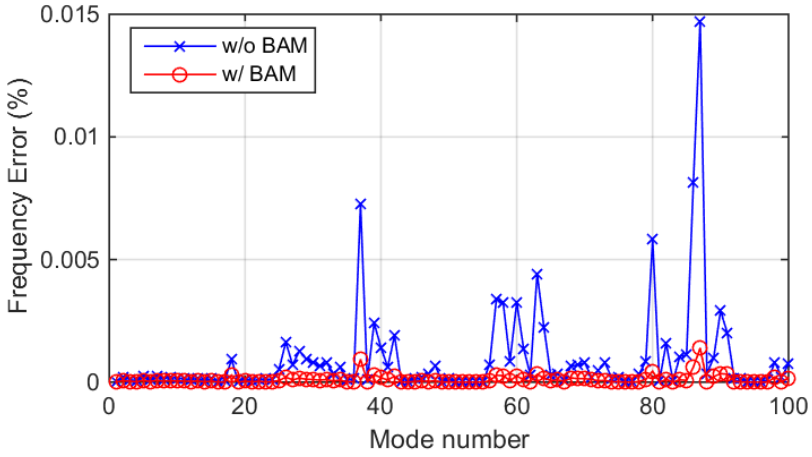

(a) Baseline results without prestress

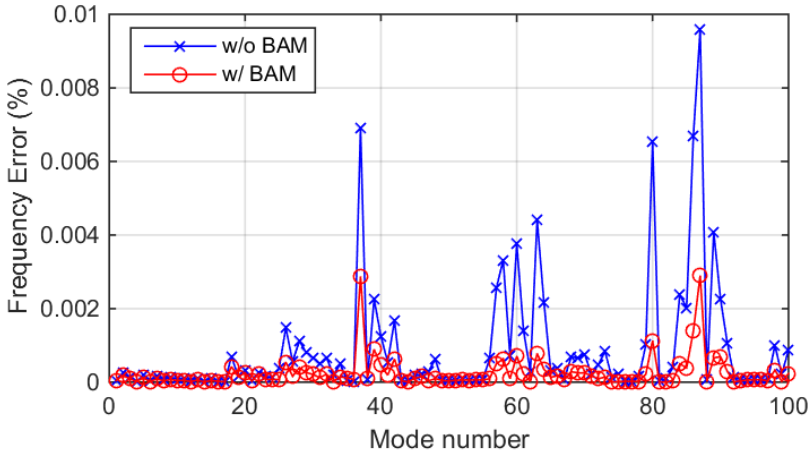

(b) MAX+ results in rotating conditions at 10000 RPM

Figure 4.9: Validation results obtained in different prestress conditions for the IBR of Figure 4.3

Next, the method was applied to the case presented in [114], which consists of the blended IBR shown in Figure 4.10a. This case presents different blends on different blades as well as different FE meshes. The results from MAX+ are reported in Figure 4.10b, and they show excellent agreement between the ROM and the full order model.

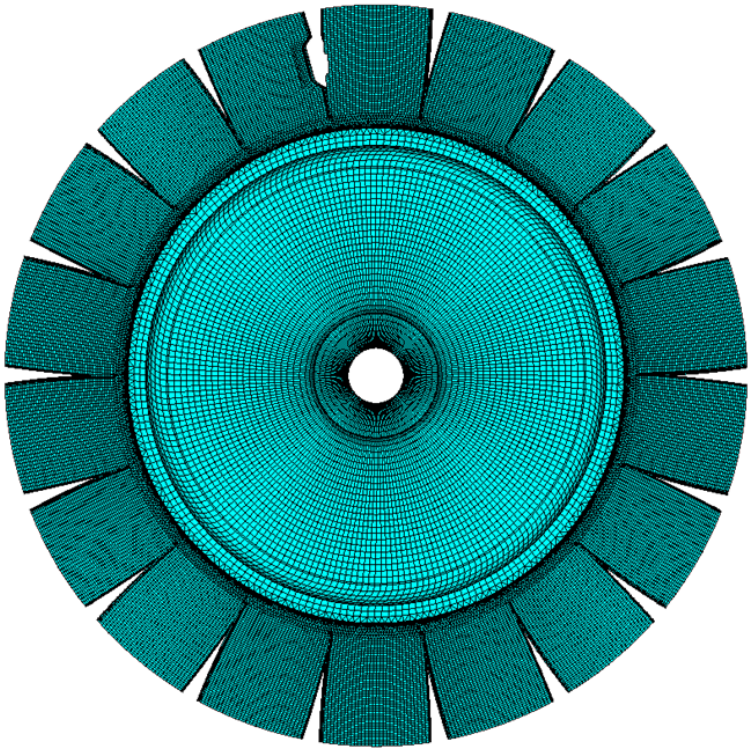

(a) Validation case using a morphed mesh [114]

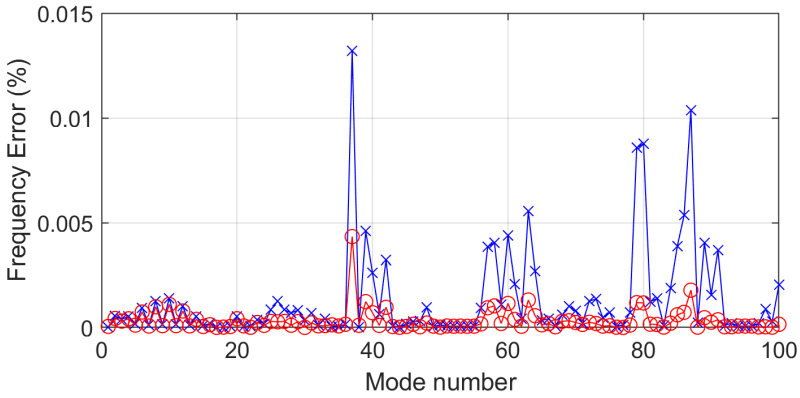

(b) MAX+ results in rotating conditions at 10000 RPM

Figure 4.10: Validation results obtained for an IBR with two distinct blends

Another feature of MAX+ that can be used to save time in the solution of problems with prestress is the use of baseline mode shapes instead of the modes at given prestress levels. The transformation matrix obtained in reference conditions can be used even for those cases when the operating conditions are different. The only variation in that case

is in the system matrices. Let us examine the case of Figure 4.6. The results for the case rotating at 10000 RPM is presented in Figure 4.11, and they show that even though the error increases significantly compared to the one shown in Figure 4.7b, the ROM still provides a good approximation. The error increase is in this case due to a change in the mode shapes.

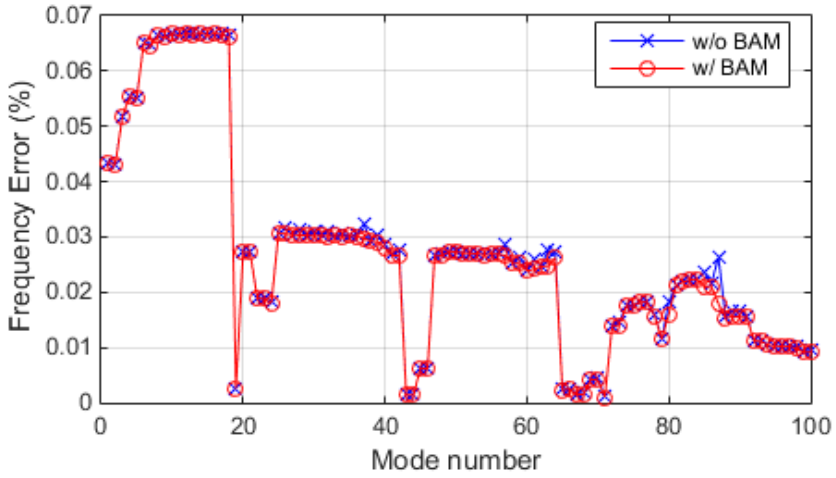

Figure 4.11: MAX+ results in rotating conditions using baseline modes for the case of Figure 4.6

4.5 Conclusions

In this paper, a novel method, MAX+, was introduced. This method extends the capabilities of MAX and allows the introduction of prestress, finite element mesh morphing, and other system characteristics in a general framework for the analysis of IBR bends. One of the enabling techniques is a method to build ROMs using only sector level matrices of quasi-cyclic structures subject to prestress. The approximation introduced in MAX+ causes little to no accuracy loss. The computational gains are significant, given that full wheel calculations are difficult for large finite element models. A metric able to quantify the error created by the approximation is proposed also. This metric addresses a significant issue in ROMs, namely knowledge of the modeling error intorduced by model reduction. This error metric was successfully applied to ROM presented in [10] built on the MAX method as well

as models built using the MAX+ method. The paper summarized the capabilities of the MAX+ method, which is a framework for the analysis of blended IBRs [112, 114]. The MAX+ method can be applied in the design process to identify optimal repair strategies. Results can be obtained quickly for different conditions, without requiring repetitive new finite element studies. The ability to accommodate the use of mesh morphing is also of paramount importance, enabling rapid creation of multiple complex geometries.

Part II

CHAPTER 5

Application of Tuned Vibration Absorber Concept to Blisk Ring Dampers: A Nonlinear Study

In this chapter, a novel design for ring dampers is proposed, where the concept of tuned vibration absorbers is leveraged to substantially increase damper effectiveness while minimizing potential stresses near the blade root. Tuned absorbers have been used in the past to reduce the forced response amplitudes of both mechanical and civil structures. The absorber natural frequency is tuned to the targeted frequency of the host structure where it is attached. The vibration reduction mechanism relies on energy transfer from the host structure to the absorber. The novel design technique proposed here uses a vibration absorber approach to achieve energy transfer from the blisk to the damper, which leads to larger damper motion. This enables energy dissipation due to friction, reducing vibrations even in blade dominated modes. An academic finite element model of a blisk with a ring damper is used to demonstrate the novel tuned damper concept and design technique. The geometric mistuning of the damper due to the presence of a gap in the ring structure is also taken into account. The results demonstrate the validity of the proposed tuned damper concept, showing a substantial vibration amplitude reduction compared to the linear baseline results, in which the damper is not tuned or absent.

5.1 Introduction

Turbomachinery bladed disks (blisks) are typically cyclically symmetric by design, however, due to manufacturing tolerances, damages, repairs, etc., the symmetry is broken in the real system. Any deviation from cyclic symmetry caused by variation in geometry or properties across blades or sectors is called mistuning, and research has shown that mistuning has a significant effect on the vibratory behavior of the system, causing vibration localization [4, 115]. Blisks may be subjected to high levels of vibration due to low damping and unintentional mistuning. The low damping is due to the absence of frictional joints at the blade-disk interface, which are instead present in conventional turbomachinery rotors. The blades of a blisk are the most vulnerable to such vibrations, which can result in high cycle fatigue and ultimately blade failure. Hence, the reduction of vibration amplitudes through an effective damping mechanism is of paramount importance.

Several damping solutions have been employed in the past, including the use of coatings [48, 49], order-tuned vibration absorbers [50], and impulse mistuning [51]. Another common approach is to use frictional contacts to dissipate energy. Typical examples are the use of shrouds and snubbers [26, 116]. Examples also include under-platform [53–55, 117–120] and ring dampers [56, 57, 62], which add nonlinear damping to the system by means of frictional dissipation. The forced response of blisks with ring dampers has been studied in the past using reduced order models (ROMs) [59–61]. The effectiveness of current damping solutions for blisks is low for the case of blade dominated modes, which are often the ones most critically affected by mistuning. In the case of ring dampers, energy dissipation and amplitude reduction occur when there is relative motion at the interface between the ring damper and the blisk. This relative motion can be difficult to obtain because the motion is typically largest in the blades, and dampers must be placed away from the blade root to avoid stress concentrations, typically in areas with small motions. Consequently, the damper

effectiveness is limited, and only modes with substantial disk participation can be targeted and damped effectively. In addition, another challenge associated with friction dampers is to ensure damper effectiveness across multiple operation regimes and frequency ranges.

A concept that has been exploited in the past for the suppression of vibrations in civil and mechanical structures is the one of tuned vibration absorbers [68, 70, 76]. Tuned vibration absorbers do not typically rely on nonlinearities, and do not require large motion at the attachment location to be effective. The effectiveness of this concept is based on the energy transfer and the frequency split that are achieved through tuning. The split in natural frequency shifts the resonance of the host structure away from the area of interest, resulting in lower amplitude response at the original frequency. Several studies have been carried out to extend the concept to multiple tuned vibration absorbers [71, 121] and multi-DOF systems [72, 73]. A good overview can also be found in [69]. Nonlinear tuned vibration absorbers systems have been studied also, and the introduction of Coulomb friction in tuned vibration absorbers has been investigated [77, 122–124]. A linear analysis on the application of this concept to cyclic structures like the one studied in this paper can be found in [73].

In this paper a novel ring damper concept for vibration reduction in bladed disks is proposed. The concept presented here combines the working principles of vibration absorbers and ring dampers to increase damper effectiveness. Nonlinear dissipation is enabled by the increase in damper motion due to tuning. This reduces the need to position the damper in a location with high relative motion between the damper and the blisk, i.e. the damper groove, because a large damper motion is ensured by damper tuning. As a result, the damper is effective for higher mode families and nodal diameters, which are characterized by blade dominated motion and are traditionally more difficult to dampen using ring dampers.

A realistic geometrically mistuned damper is used in the case study presented here to introduce the effects of mistuning in addition to nonlinearities. The ring damper geometry and material are chosen such that the structure presents the same natural frequency of the

targeted blisk mode that is damped. The forced response obtained using a tuned vibration absorber is compared to the response obtained when an equivalent non-tuned damper is used, which is used as a baseline for comparison. A substantial amplitude reduction is achieved by means of frictional dissipation by introducing the tuning concept. The effects of variations in tuned vibration absorber frequencies and nonlinear energy dissipation are investigated also. It is found that energy dissipation can change based on whether there is a perfect match between the blisk and the damper frequencies or there is a small difference. However, in all the examined cases, the damper effectiveness is increased compared to the baseline.

5.2 Methodology

In this section, the concepts used in this study are presented. First, the working principle and expected outcome of the application of the method are presented. Frictional nonlinearities and contact conditions are then introduced. Finally, the procedure used to ensure a match between the natural frequencies of the blisk targeted modes and the damper modes is presented. The blisk considered in this study is tuned.

A simple lumped-mass representation of the tuned vibration absorber concept is presented in Fig. 5.1, where a single-DOF vibration absorber is attached to a single-DOF main system. A comparatively small mass m is attached to the main mass M by means of a spring k to reduce the vibration amplitude of the original mass M. The qualitative trends shown in Fig. 5.2 represent the behavior of a single-DOF system in the presence of a vibration absorber. In general, the added mass m does not substantially affect the behavior of the system, as described by the blue line. In [68] it was shown that for the simple case of an undamped oscillator it is possible to significantly reduce the vibration response of the mass M at its natural frequency by adding a tuned vibration absorber having the same natural frequency, i.e. satisfying $\sqrt{\frac{K}{M}} = \sqrt{\frac{k}{m}}$. With a tuned vibration absorber the response in yellow is

obtained, where a shift in the natural frequencies of the system can be observed. It is important to mention that the amplitude of motion of the damper increases as a result of tuning. Energy can be dissipated by introducing a Coulomb friction elements between the two masses, with a result qualitatively similar to the orange line of Fig. 5.2, where the vibration amplitude is reduced. This concept is extended to a realistic multi-DOF system with a multi-DOF damper in the following section.

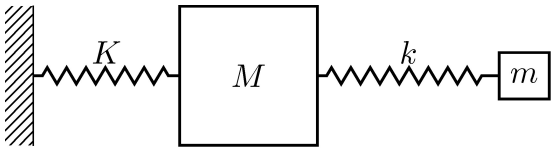

Figure 5.1: Schematic of a simple spring-mass system (K,M) representing the blisk with a smaller tuned vibration absorber attached (k,m)

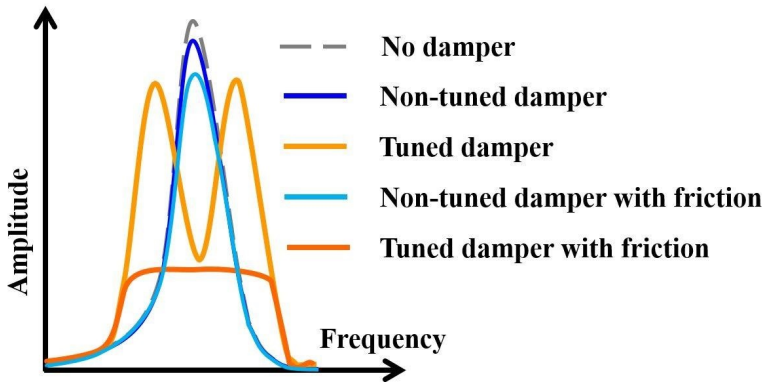

Figure 5.2: Conceptual representation of the forced response of the main mass shown in Fig. 5.1

5.2.1 Blisk EOMs and contact nonlinearities

The equations of motion (EOMs) for a blisk hosting a ring damper can be written in general form as

$$\mathbf{M}\ddot{\mathbf{x}} + \mathbf{C}\dot{\mathbf{x}} + \mathbf{K}\mathbf{x} = \mathbf{f}_e + \mathbf{f}_n(\dot{\mathbf{x}}, \mathbf{x}), \tag{5.1}$$

where $\mathbf{M}$, $\mathbf{C}$ and $\mathbf{K}$ are the mass, damping, and stiffness matrices obtained in the absence of contacts, $\mathbf{f}_e$ is the vector of external periodic forces acting on the structure, and $\mathbf{x}$ is the

vector of generalized coordinates. The vector $\mathbf{f}_n$ represents the nonlinear forces, which are due to the contacts between the damper and the blisk. Proportional damping is used, and the damping matrix can be written as $\mathbf{C} = \beta\mathbf{K}$. The mass and stiffness matrices can be written as

$$\mathbf{M} = \begin{bmatrix} \mathbf{M}_b & \mathbf{0} \\ \mathbf{0} & \mathbf{M}_d \end{bmatrix}, \quad \mathbf{K} = \begin{bmatrix} \mathbf{K}_b & \mathbf{0} \\ \mathbf{0} & \mathbf{K}_d \end{bmatrix}, \tag{5.2}$$

where the subscripts b and d refer to the blisk and the damper components respectively. Having obtained the matrices $\mathbf{K}$ and $\mathbf{M}$ without considering contacts, the connectivity between the two bodies is enforced through the forcing term $\mathbf{f}_n$.

A relative coordinate formulation is used to describe the displacement at the contact interface, similar to [26, 125]. Thus, the DOFs must be reordered, and a coordinate transformation $\mathbf{x} = \mathbf{T}\mathbf{x}_r$ between the original coordinates in $\mathbf{x}$ and the relative coordinates in $\mathbf{x}_r$ be applied. The relative coordinates can be partitioned as

$$\mathbf{x}_r = \begin{bmatrix} \mathbf{x}_2 - \mathbf{x}_1 \\ \mathbf{x}_1 \\ \mathbf{x}_0 \end{bmatrix}, \tag{5.3}$$

where $\mathbf{x}_1$ contains the contact DOFs on the blisk groove, $\mathbf{x}_2$ contains the contact DOFs on the damper, and $\mathbf{x}_0$ contains all the remaining DOFs. The DOFs in $\mathbf{x}_0$ are not directly affected by nonlinearities, thus the displacement vector $\mathbf{x}_r$ and the corresponding forcing vector $\mathbf{f}_{nr}$ can be partitioned as

$$\mathbf{x}_r = \begin{bmatrix} \mathbf{x}_n \\ \mathbf{x}_0 \end{bmatrix}, \quad \mathbf{f}_{nr} = \begin{bmatrix} \mathbf{f}_{nr,c} \\ \mathbf{0} \end{bmatrix}, \tag{5.4}$$

where $\mathbf{x}_n$ and $\mathbf{f}_{nr,c}$ contain all the DOFs affected by nonlinearities, i.e. the ones belonging to

$\mathbf{x}_1$ and $\mathbf{x}_2$. A node-to-node contact model is used, where all pairs of nodes having coincident location form a contact pair. The sets of DOFs $\mathbf{x}_1$ and $\mathbf{x}_2$ presented in Eq. 5.3 contain such contact pairs. The 1D contact model presented in [26, 61] is used to model the interaction between disk and damper.

Let us define a local coordinate system at each contact node pair, in which z represents the normal direction, and x,y represent the tangential directions. For the node i the tangential contact stiffness $k_{i,x}$,$k_{i,y}$ and normal contact stiffness $k_{i,z}$ are represented by 1D springs. Let us call $N_i(t)$ the normal contact force at the node pair i, and v_i the normal relative displacement, which is positive when the surfaces penetrate each other. The contact force $N_i(t)$ can be defined as

$$N_i(t) = \max(k_{i,z} \cdot v_i(t), 0), \tag{5.5}$$

which is thus positive when there is contact and zero in *separation*. The prestress $N_{i,z0}$ that is applied to the contact node pairs to ensure contact in static condition is implicitly included in Eq. 5.5 because the term $v_i(t)$ contains the static solution. Let us define $w_{i,x}$ and $w_{i,y}$ as the tangential slip between the contact surfaces and $u_{i,x}$ and $u_{i,y}$ as the relative displacements in the tangential directions. The tangential force $T_{i,x}(t)$ is defined as

$$\begin{cases} T_{i,x}(t) = k_{i,x} \cdot (u_{i,x}(t) - w_{i,x}(t)), & \text{stick} \\ T_{i,x}(t) = \mu N_i(t) \cdot \text{sign}(\dot{w}_{i,x}(t)), & \text{slip} \\ T_{i,x}(t) = 0, & \text{separation} \end{cases} \tag{5.6}$$

where μ is the friction coefficient. $T_{i,y}(t)$ is similarly defined by changing the subscript x to y. A more detailed explanation of this contact model can be found in [26, 126]. The contact status can be *slip*, *stick* or *separation*. The contact condition must be calculated at every time t and for every node location. *Separation* occurs when the two nodes are not in contact, i.e. there is a gap between the two surfaces. Both *slip* and *stick* conditions

occur when there is contact between the contact surfaces. If $N_i(t)$ is positive, there are two possible states for the contact. If the tangential force $T_{i,x}(t)$ or $T_{i,y}(t)$ calculated for the *stuck* case is larger than the product $\mu N_i(t)$, where μ is the coefficient of friction, the contact is in *slip* condition, otherwise it is *stuck*. This may happen in any direction x or y. *Stuck* conditions do not imply that there is no relative motion $\mathbf{x}_2 - \mathbf{x}_1$, but rather that $w_{i,x}(t)$ or $w_{i,y}(t)$ remain constant. As a result, the node pair is effectively connected by a linear spring in the corresponding direction. At any time t, the contact condition must be evaluated, and the corresponding forcing term $\mathbf{f}_n$ must be applied. This makes Eq. 5.1 highly nonlinear, resulting in a significant computational cost associated with its solution. It is important to notice that the contact condition only depends on the relative motion $\mathbf{x}_2 - \mathbf{x}_1$ between the damper and the blisk.

To increase computational efficiency, Craig-Bampton component mode synthesis (CB-CMS) [42] is used to reduce the number of linear DOFs. Only the contact nodes on the blisk and the entire set of damper nodes are preserved as master nodes, and the corresponding set of slave modes is calculated. This ROM is used to assess the effectiveness of the proposed damper concept. Equation 5.1 is solved using the harmonic balance method (HBM) [127] to obtain the steady state response to a traveling wave excitation. The combination of CB-CMS and HBM is used to substantially reduce the time required for the solution of the EOMs.

5.2.2 Damper tuning

The damper used in this study is shown in Fig. 5.3. Note that it presents a gap that makes it non-axisymmetric. The presence of the gap serves two purposes. The first one is to ensure preload at the contact interface. Centrifugal forces cause the damper to deform substantially in the radial direction, which is possible thanks to the gap. As a result contact at the interface between the damper and the blisk groove is ensured. The static equilibrium would be different if the damper was perfectly axisymmetric, with possible loss of contact

or inadequate preload. Secondly, the damper becomes mistuned, i.e. non-axisymmetric, due

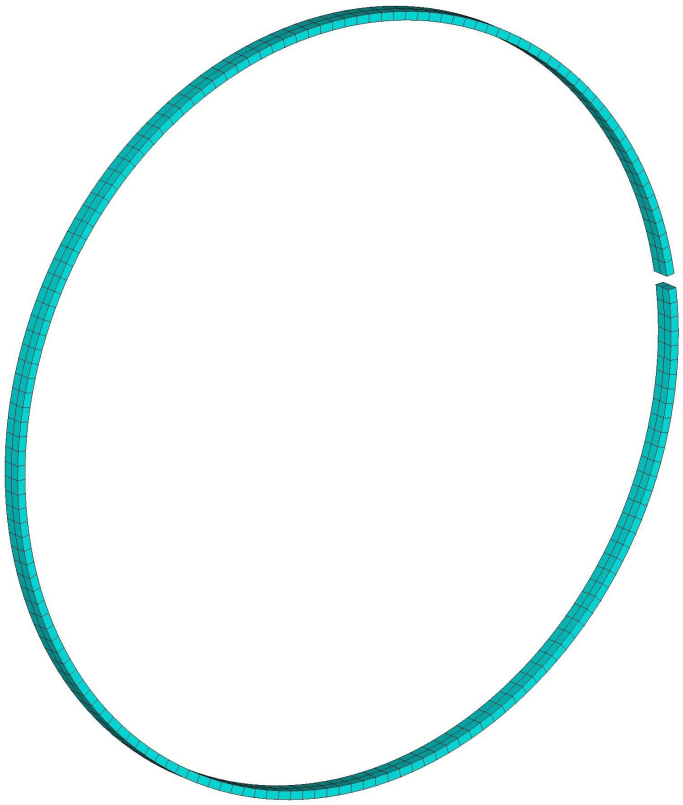

Figure 5.3: Geometry of the ring damper used in the analysis

to the presence of the gap. This results in its normal modes being mistuned. If a spatial Fourier analysis is carried out for any damper mode it would be possible to observe multiple spatial harmonics, or nodal diameter contributions. This is particularly convenient, because it allows the damper to couple with multiple blisk modes with various nodal diameters. Previous studies showed that the coupling is not possible if the system is tuned, where only few nodal diameters can be used [73]. Damper mistuning is thus beneficial because it allows to tune damper modes for multiple blisk nodal diameters. The damper position in the blisk groove is shown in Fig. 5.4. For this study, it is assumed that there is clearance between the sides of the damper and of the groove. Thus, the side nodes are always in *separation*. The

contact condition of the nodes at the top is instead determined at every time t based on the relative motion between the damper and the blisk groove $\mathbf{x}_2 - \mathbf{x}_1$.

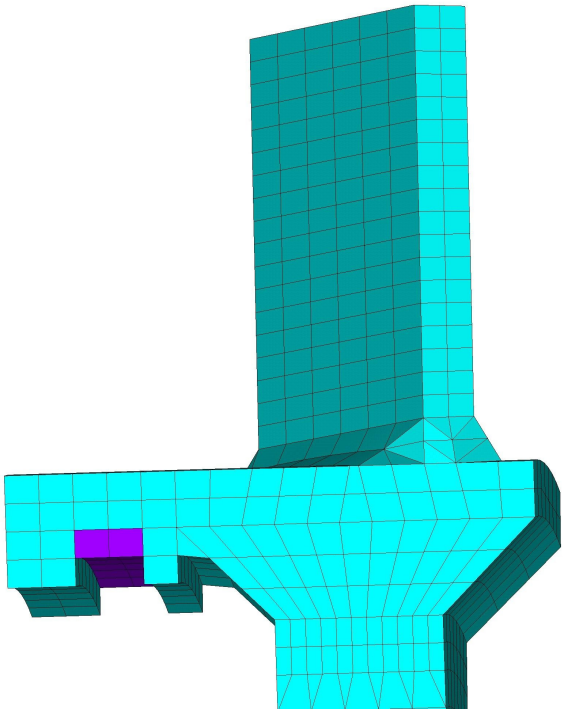

Figure 5.4: View of the damper and the blisk groove

The damper matrices presented in Eq. 5.2 are obtained for the free damper, i.e. a damper that is not constrained to the groove, because the contacts and constraints are introduced using the nonlinear forcing term. To apply the concept of a tuned vibration absorber, it is necessary to tune the damper, i.e. to ensure that one of its natural frequencies matches the blisk frequency to be damped. For the tuning of the damper, appropriate boundary conditions and contact conditions must be enforced. The *stuck* natural frequencies of the damper are used for tuning. The reason why stuck contact conditions were chosen is that the nonlinear response is expected to lie close to the linear stuck response until microslip phenomena appear. Based on previous literature, a small shift in peak frequency of the response could also occur [26, 128]. The *stuck* natural frequencies are obtained by considering

the contact node pairs in stuck conditions, i.e. connected by linear springs in all three directions. To calculate such frequencies, the blisk nodes are assumed to be fixed. Once the blisk alone natural frequencies are known, an undamped modal analysis is carried out on the constrained damper. The constrained damper mass matrix $\mathbf{M}_d$ does not change based on contact conditions. The stuck stiffness matrix $\mathbf{K}_{d,c}$ used for tuning purposes is instead dependent on the contact conditions, and it can be written as

$$\mathbf{K}_{d,c} = \mathbf{K}_d + \Delta\mathbf{K}_d, \tag{5.7}$$

where $\Delta\mathbf{K}_d$ is the matrix that enforces the presence of linear springs between the contact pairs to simulate a stuck contact and $\mathbf{K}_d$ is the matrix obtained without contacts. $\Delta\mathbf{K}_d$ has simple diagonal form because a relative co-ordinate system is used, as shown in Eq. 5.3. Thus,

$$\Delta\mathbf{K}_d = diag(k_{1,x}, k_{1,y}, k_{1,z}, \dots, k_{i,x}, k_{i,y}, k_{i,z}, 0, 0, 0, \dots), \tag{5.8}$$

which is populated with the nodal contact stiffnesses $k_{i,x}, k_{i,y}, k_{i,z}$ in the contact DOFs, and zeros elsewhere. Once the stiffness matrix $\mathbf{K}_{d,c}$ is obtained, it is possible to study the natural frequencies and normal modes of the damper. The eigenvalue problem can be written as

$$\mathbf{K}_{d,c}\mathbf{\Phi} = \mathbf{M}_d\mathbf{\Phi}\mathbf{\Lambda}_{d,c}, \tag{5.9}$$

where $\mathbf{\Phi}$ is a matrix whose columns represent the normal modes of the system, and $\mathbf{\Lambda}_{d,c} = diag(\omega_1^2, \dots, \omega_n^2)$ is a diagonal matrix containing the eigenvalues. Please note that the contact parameters have a significant impact on the tuned damper frequencies and their estimation can be particularly challenging. Studies on the identification of contact stiffness parameters can be found in [118–120].

Once the targeted mode of the blisk is chosen, its frequency Ω_t is known. The blisk

natural frequency Ω_t is obtained considering the blisk alone without the damper attached, similar to what is done in [68] for the lumped mass example shown in Fig. 5.1. In order for this damper to behave as a tuned vibration absorber, the frequency $\omega_i = \Omega_t$ must be identified. If there is no such frequency ω_i, the frequency match can be obtained by means of geometric design and material changes. As a proof of concept, in this study the material properties of the damper were changed to ensure that there exists a value of i for which $\omega_i = \Omega_t$. In particular, the stiffness of the constrained damper was increased by 78.7%. The necessary material property change is large because the damper geometry analyzed here is very simple, but this change is small enough that it may be achievable by means of a more complex geometry also.

5.3 Results

The methods presented in the previous section are applied to the case of an academic blisk with $N = 24$ blades. The blisk used in the simulation is presented in Fig. 5.5. The full wheel finite element model of the blisk comprises $51,240$ nodes and $44,424$ elements. The damper is comprised of $1,008$ nodes and 334 elements. Due to the fact that only the contact nodes at the interface between blisk and damper present nonlinearity, CB-CMS can be used to reduce the other DOFs of the system. All $1,008$ nodes of the damper finite element model were preserved. This resulted in a damper model having $3,024$ DOFs. For the blisk, only the interface nodes and two nodes per blade located at the blade tip were preserved. The blade tip nodes are used to apply the traveling wave excitation to the blades and to measure their response, and they are shown in Fig. 5.5. There are 840 interface nodes, and 48 blade nodes. There were 500 slave modes retained in the CB-CMS analysis, resulting in a blisk model with $3,164$ DOFs. The number of DOFs of the entire assembly is thus $6,188$. There are 504 interface nodes affected by the frictional nonlinearities, the others being side

nodes considered to be always in *separation* in this study. The same contact preload N_{i,z_0} is uniformly applied at all nodes. Parameter $\mu\frac{\sum_i N_{i,z_0}}{F}$ (where F is the forcing amplitude) is of interest because it was used in previous studies [26] and it captures the level of microslip present in the system. For the results shown in this paper, we used $\mu\frac{\sum_i N_{i,z_0}}{F} = 10^4$.

In this study, the blisk is tuned, and the only source of mistuning is the damper gap. The lowest natural frequencies of the damper before tuning are presented in Fig. 5.6. Note the high modal density of the damper. Figure 5.7 shows the frequency-nodal diameter plot of the blisk and the tuned damper frequencies ordered by mode index. The blisk mode targeted in this study belongs to the 1^{st} family, $ND = 5$. Such a mode was chosen to validate the concept proposed here because previous studies showed that traditional ring dampers effectiveness is low for blade dominated modes having low disk motion [63]. In contrast, the ring damper concept proposed here is effective in those conditions. The frequency of the blisk targeted mode is $f = 2,112.8$ Hz, and the 10^{th} damper mode is chosen to damp it. The damper is tuned by adjusting its material properties. Note the frequency overlap at the crossing between the two series of results shown in Fig. 5.7. The purpose of choosing the 10^{th} mode is to highlight that the proposed concept is robust and effective even in cases where the blisk nodal diameter to be damped is not dominant in the correspondent damper mode. The 10^{th} mode contains all nodal diameters, but $ND = 5$ of the mode to be damped is not dominant. There is no need to match the nodal diameter with the one of the targeted blisk mode because the damper is mistuned. However, it is important to ensure that the corresponding nodal diameter content of the damper mode is sufficiently large. First, a spatial Fourier Transform of the nodal displacements of a set of given nodes (one per each sector) along a chosen direction is carried out. The coefficients obtained from such analysis represent the participation factors of different spatial harmonics, which constitute the nodal diameter content of the mistuned mode. The nodal diameter content of the damper mode used for tuning purposes is shown in Fig. 5.8. Note that the chosen mode does not have its

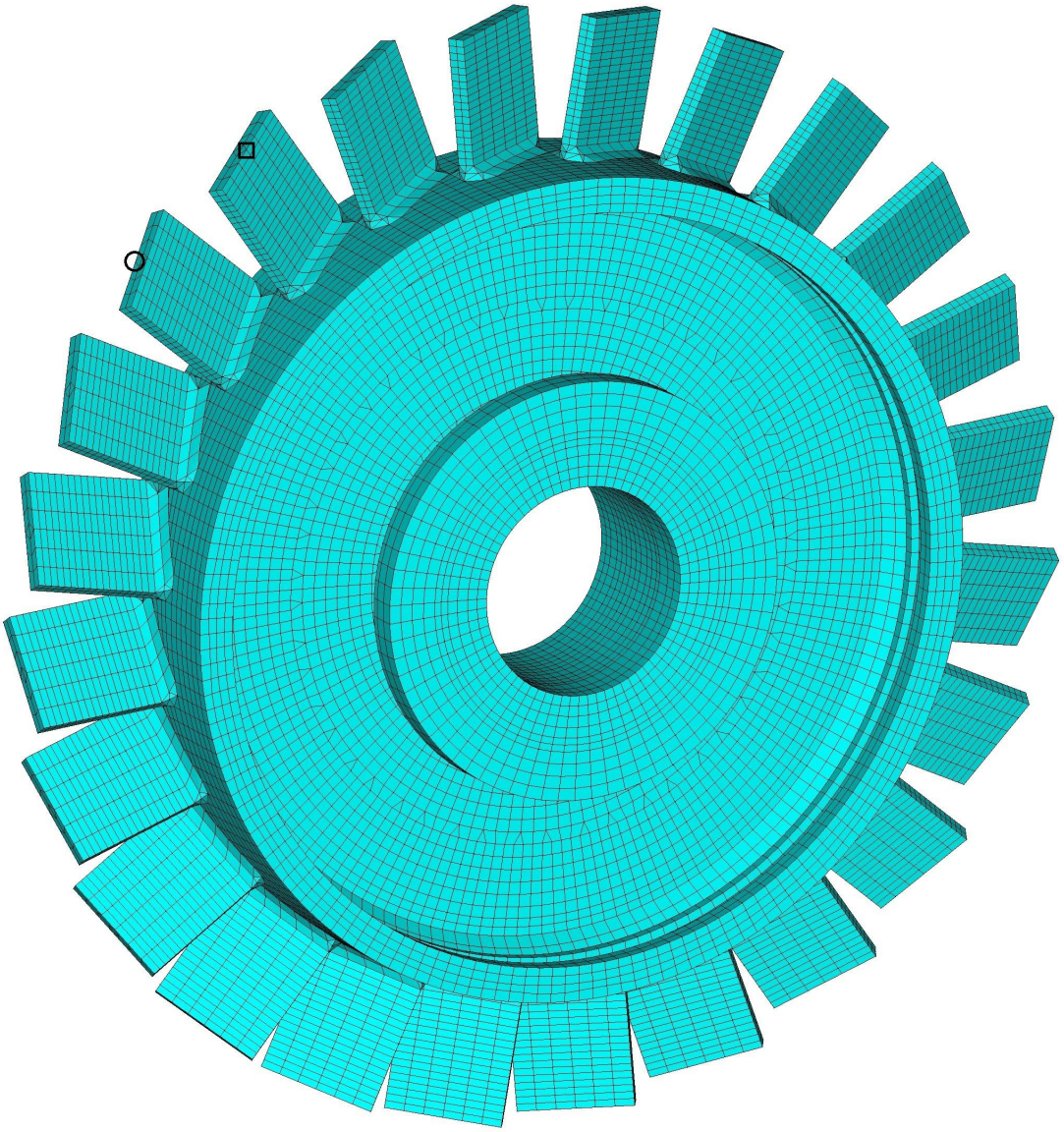

Figure 5.5: Academic blisk having $N = 24$ blades used for the study. Forcing and response data nodes are marked with a square and a circle respectively.

maximum nodal diameter component at $ND = 5$. However, the chosen mode has a relatively large $ND = 5$ component.

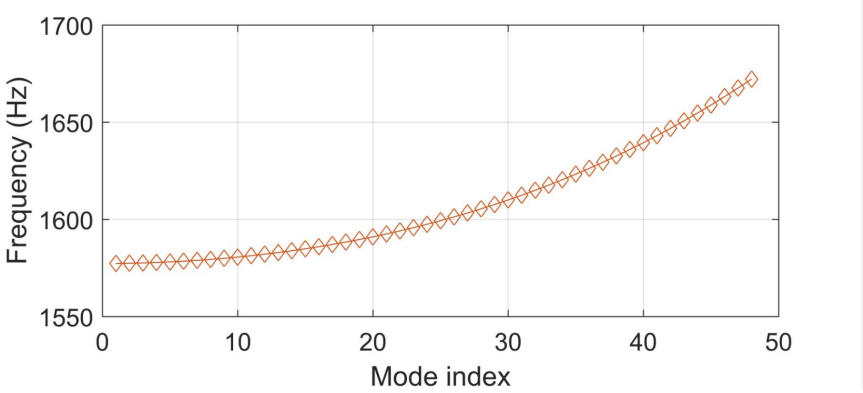

Figure 5.6: Frequency versus mode index plot for the non-tuned damper

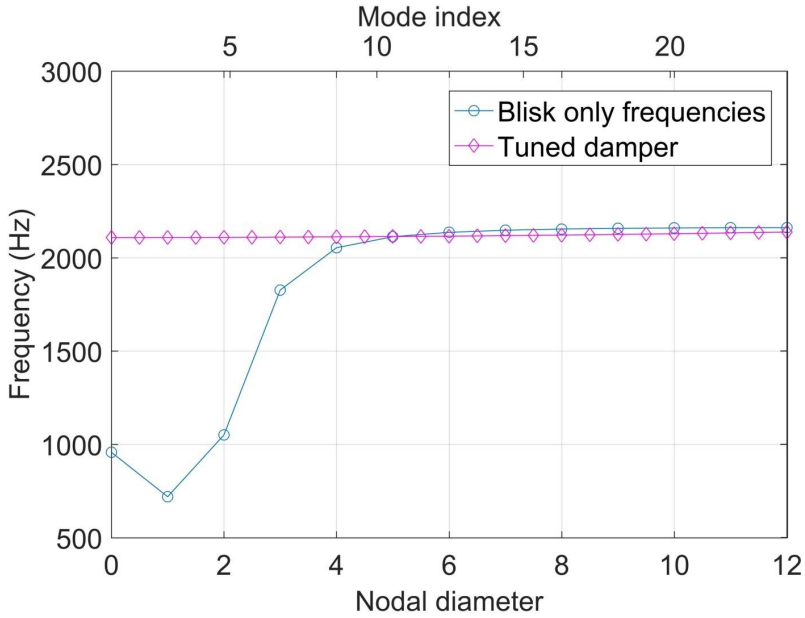

Figure 5.7: Frequency versus nodal diameter plot for the blisk and frequency versus mode index plot for the tuned damper

5.3.1 Forced response

To evaluate the effectiveness of the proposed damper concept, a forced response analysis is carried out. An $EO = 5$ traveling wave excitation is applied to the blisk. Forcing is

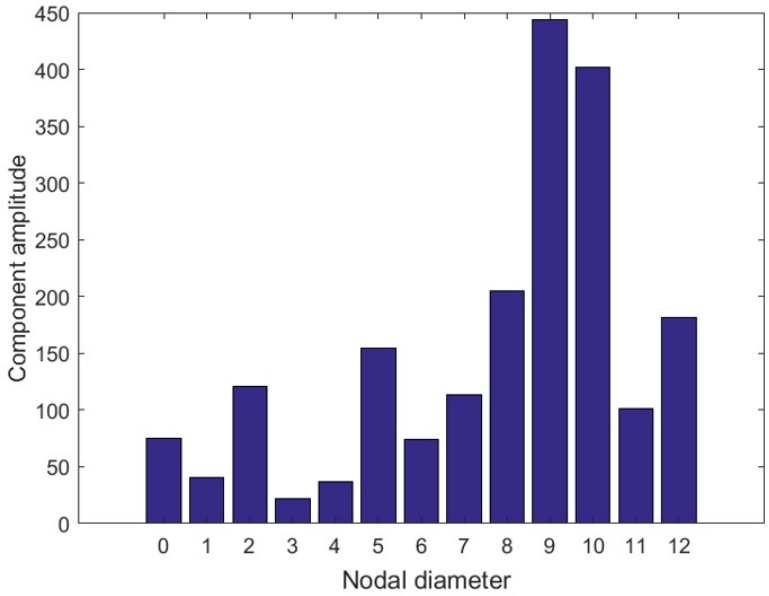

Figure 5.8: Nodal diameter content of the damper mode used to damp a blisk mode having $ND = 5$

applied on a blade node for each sector of the blisk in the axial direction. The location of the forcing and response nodes are shown in Fig. 5.5. The forcing level and the prestress forces are kept constant in this study. Only the type of ring damper used is varied.

First, the linear response is calculated for both the blisk with a tuned damper and the blisk with a non-tuned damper. The non-tuned damper is defined as a damper that does not have at least a natural frequency matching the natural frequency of the targeted blisk mode. The linear response is calculated in stuck conditions because that is the typical condition that can be found when frictional nonlinearities are not activated. Then, a nonlinear analysis is carried out to investigate the effects of the tuned damper and of the non-tuned damper. The tuned damper is expected to operate in the microslip regime, i.e. a contact condition in which contact nodes exist in both stuck and slip conditions. The results are presented in Figs. 5.9 and 5.10. Four sets of data are presented, two linear and two nonlinear. The response is calculated by taking the maximum amplitude over all blades in the axial direction.

The linear response in stuck conditions for the non-tuned damper is presented in Fig.

5.9. Note that the nonlinear results almost perfectly overlap with the linear response, which means that nonlinearities are not activated and the system is in stuck conditions and not in microslip. Activation or lack of activation of nonlinearities depends on the preload, friction and forcing conditions. Limited to the case we studied, we can conclude that in the simulated conditions of preload, friction, and forcing, a traditional ring damper is ineffective, providing no amplitude reduction. When the damper is non-tuned, the frictional nonlinearities are not activated due to the low motion amplitude at the contact, and thus there is no energy dissipation.

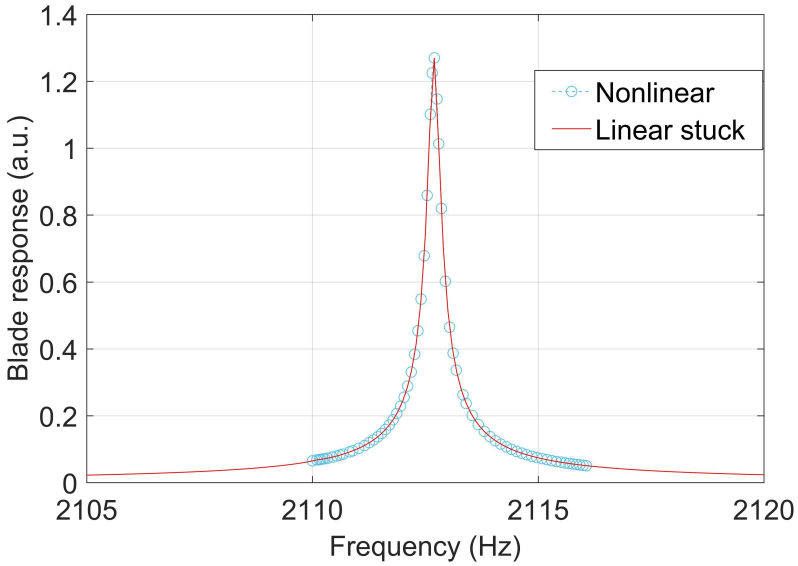

Figure 5.9: Linear and nonlinear analyses of the forced response of a system employing a non-tuned ring damper

The results obtained with a tuned damper are presented in Fig. 5.10. Note that in the tuned case there is a substantial frequency split and that many peaks are present even in the linear case. The presence of multiple peaks is due to the presence of mistuning in the damper. Several small resonance peaks that were not present for the non-tuned damper can be observed within the frequency range, due to the high modal density of the damper, as it can be seen from Fig. 5.6. Even though there is an amplitude change compared to the

linear results obtained with a non-tuned damper, this change is not substantial, as there is no significant variation of linear damping due to the use of a tuned absorber. The nonlinear results obtained using a tuned damper show instead a significant variation compared to both linear cases. Due to the simultaneous effects of friction nonlinearity and tuned damper absorber, the vibration amplitude of the blades is significantly reduced. Significant amplitude reduction can be seen in the areas corresponding to the linear resonance. Close to the linear resonance the damper motion is increased, and this results in large relative motion. As a result, slip occurs at some of the contact node pairs and energy dissipation is enabled.

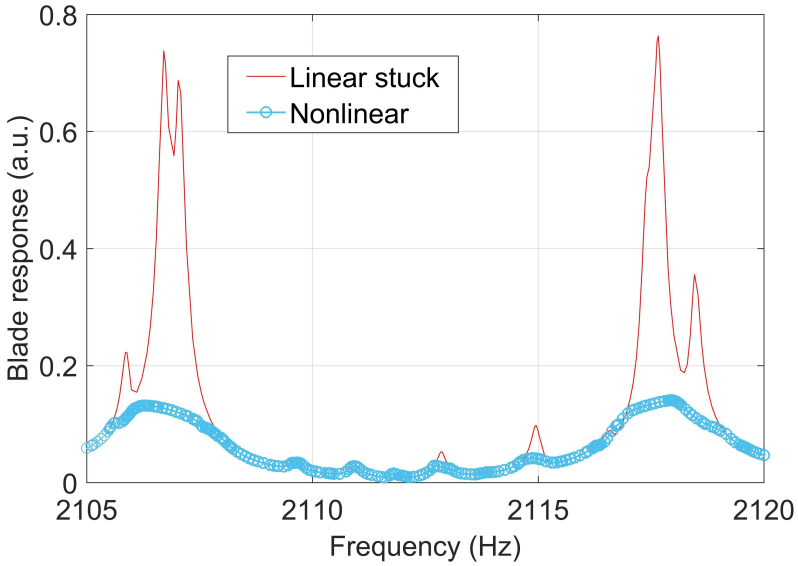

Figure 5.10: Linear and nonlinear analyses of the forced response of a system employing a tuned ring damper

The maximum blade vibration amplitude obtained with the tuned damper is 0.14. When a traditional damper is used, the blade vibration amplitude is 1.27, which means that a 90% reduction can be achieved using this damper concept. Figures 5.9 and 5.10 were obtained by using the maximum vibration amplitude over all the blades. More information about mistuning effects may be obtained by studying individual blade responses. In Fig. 5.11, the nonlinear results presented in Fig. 5.10 are plotted for each blade. The blades present

different vibration amplitudes. In general, multiple peaks appear in the response because the peak amplitudes of each blade are at distinct frequencies. This effect is mitigated by nonlinearities. Note in Fig. 5.11 that the simultaneous presence of nonlinearities and mistuning causes only relatively small amplitude variation between blades near the main peaks.

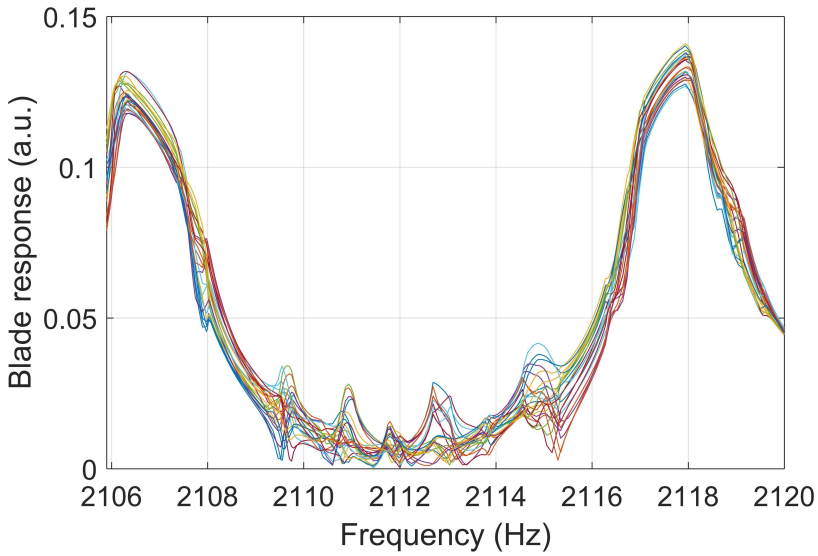

Figure 5.11: Individual blade responses for the nonlinear case shown in Fig. 5.10

5.3.2 Analysis of damper motion

To analyze the origin of energy dissipation, the motion of the damper is examined. Figures 5.12 and 5.13 show the amplitude of the damper motion at the contact interface for both the tuned and the non-tuned dampers. It is possible to observe that the motion of the damper is much larger in the tuned case, even though the blade amplitude is lower. This confirms the expected increased motion due to energy transfer. Furthermore, the peaks of the response shown in Fig. 5.12 are cut by the effects of nonlinearities, i.e. the damper shows the same behavior of the blisk blades, and both of them show signs of microslip in the same frequency range. The increased motion is shown for the axial direction because a damper mode with dominant motion along that direction was chosen and because of the presence of clearance

between the damper sides and the blisk groove.

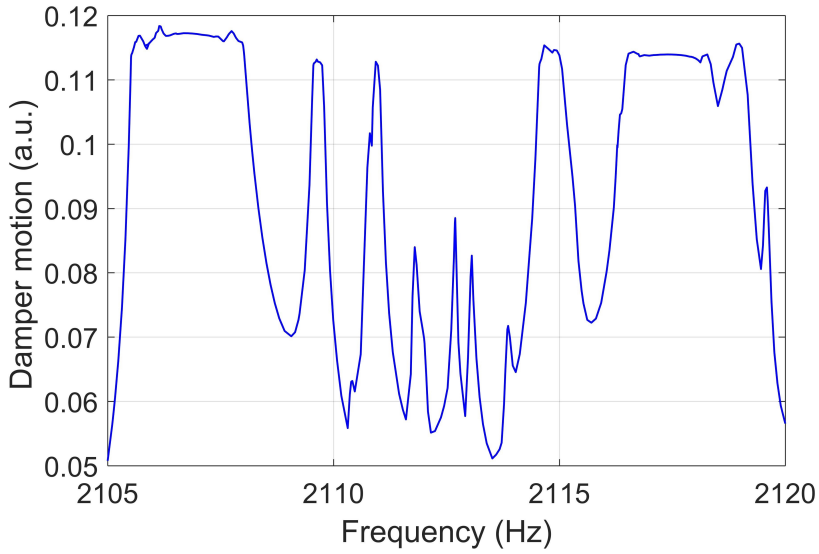

Figure 5.12: Damper response for the tuned damper corresponding to Fig. 5.10

5.3.3 Effects of detuning and damping variations

In the previous section, the effects of frictional nonlinearities were examined by comparing linear and nonlinear results for the case of a perfectly tuned damper. However, in real applications it is impossible to achieve a perfect match between damper and blisk frequencies due to geometric and material tolerances. In this section, a sensitivity analysis based on the variation of natural frequency of the damper is carried out to examine the effects of detuning on damper effectiveness. The analysis is carried out to shed light onto the energy transfer and dissipation mechanisms in the system. The targeted mode frequency is the same as before, i.e. $2,112.8$ Hz, but the damper mode that is improperly tuned has a frequency that is 21.0 Hz or 52.2 Hz above the original target frequency, which is equivalent to a 1.0% or 2.5% frequency variation. The damper frequencies are now outside the frequency range examined in the forced responses in Figs. 5.9-5.13. However, the improperly tuned damper is expected to have a diminished but non-zero effect on the blisk response due to the fact

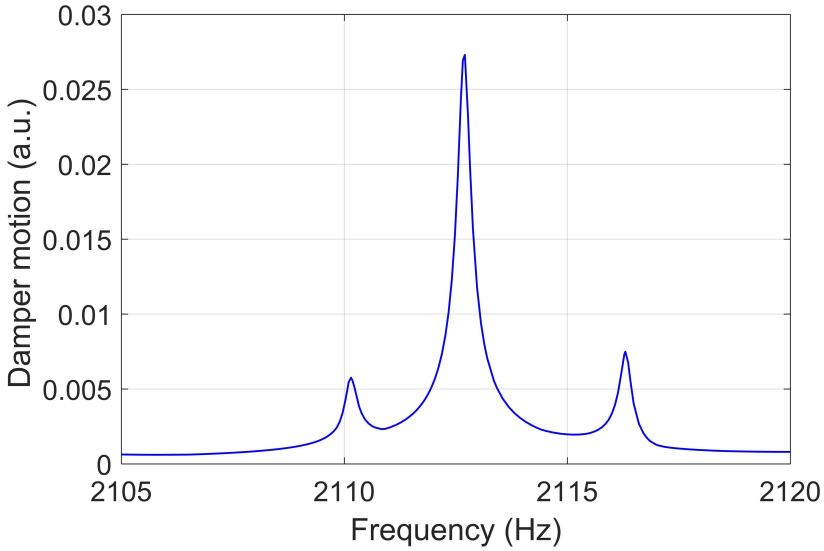

Figure 5.13: Damper response for the non-tuned damper corresponding to Fig. 5.9

that its frequencies are relatively close to those of the blisk. A larger damper motion is expected for the tuned damper compared to the non-tuned damper. This results in larger relative motion at the interface between blisk and damper, which in turn, causes more energy dissipation and thus lower blade vibration amplitudes.

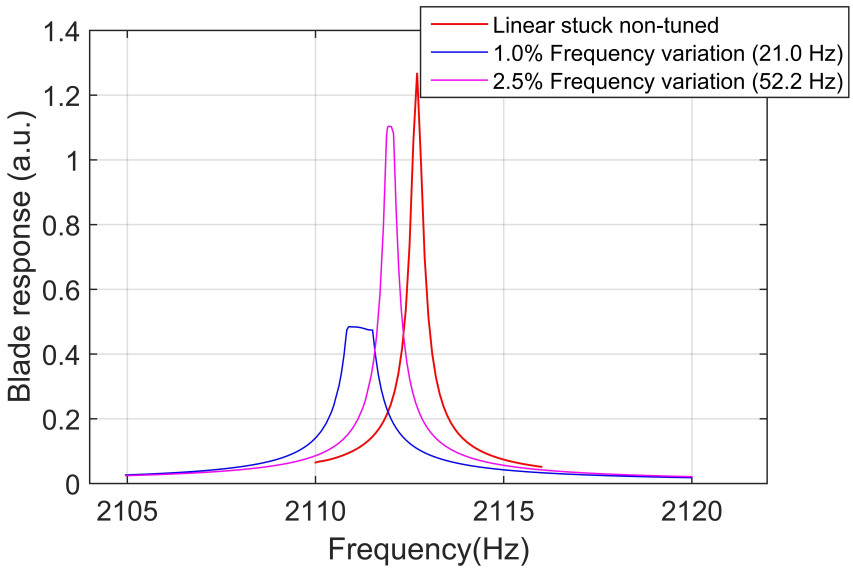

Figure 5.14: Effect of damper detuning on the response of the blisk (nonlinear)

From Fig. 5.14 it is possible to notice that the nonlinear results present a significant deviation from the ones obtained in the perfectly tuned case of Fig. 5.10. The frequency split that was observed before is not present anymore. Even if the frequency split and the mistuning are now not as visible as before, the nonlinear calculations showed a significant amplitude reduction, as well as a minor frequency shift. Both the frequency shift and the amplitude reduction are consistent with what was expected. This confirms the robustness of the approach.

5.4 Conclusions

A novel ring damper concept able to effectively damp vibration in blisks was proposed based on the tuned vibration absorber idea. A tuning method for the vibration reduction of a multi-DOF system based on the addition of a multi-DOF damper was introduced and validated. This method requires the use of a mistuned damper to preserve the ability to target any blisk modes independent of nodal diameter. The effectiveness of the proposed design was studied by calculating the forced response of the system. Linear and nonlinear results were obtained to compare the effectiveness of the proposed tuned vibration absorber to a traditional non-tuned ring damper. A significant amplitude reduction was achieved using the proposed concept. This reduction was made possible by enabling frictional nonlinearities to dissipate energy by means of increased damper motion. Damper motion was also studied to gain insight into the energy dissipation mechanism. The robustness of the approach was assessed by evaluating the response in case of an improperly tuned damper. Damper effectiveness showed a decrease compared to the case of perfect tuning. However, greater effectiveness was observed compared to the non-tuned case. The proposed concept is able to reduce the vibration level of multiple blisk modes. Even the modes that show little motion at the damper-blisk interface can be damped by using the proposed tuned vibration absorbers.

This paper demonstrated the effectiveness of a novel damper concept using a traditional damper geometry. Future work could be carried out on the exploration of different damper geometries capable of further increasing the effectiveness of such dampers. The response at different engine orders and for different mode families could be analyzed. A study on the interaction between the damper modes and the blisk modes may also be beneficial. In the design of a vibration absorption based damper for a realistic blisk, several other parameters will need to be studied, such as blisk mistuning, and the effects of prestress conditions on the nonlinear dynamics. Experimental and numerical results using airfoils and blisks with more realistic geometries could also be used for validation.

CHAPTER 6

An Experimental and Computational Study on a Tuned Mass Damper With Frictional Contacts

Turbomachinery blisks have very low damping, and for this reason, they require devices such as ring dampers to mitigate excessive vibrations. Ring dampers rely on the relative motion between a ring-like component and the blisk to dissipate energy by means of friction. Damper effectiveness is typically low due to the absence of relative motion between the damper and the blisk. Tuned mass dampers can mitigate the low relative motion and can be particularly effective when the forcing is narrow-band. Tuned mass dampers transfer vibration energy from the host structure to the damper, where this energy can be dissipated by friction. These two features are particularly useful when the host structure has very low damping and when there are stringent constraints on the position of the damper, as is the case for turbomachinery blisks. In this paper, a tuned vibration damper concept is explored. A cantilever beam is used to represent a blisk blade. The vibration reduction provided by the use of a tuned mass damper with contacts is studied both computationally and experimentally. Numerical and experimental results are compared to validate the model and to gain insight into the energy dissipation phenomena and the working principles of such dampers.

6.1 Introduction

Vibration reduction is of paramount importance in several applications in aeronautics and astronautics to ensure durability and reliability of structural components. This is particularly important for components that have to withstand a large number of cycles and could fail due to fatigue. Such examples can be found in fasteners [129] and turbomachinery blisks [4, 116].

Turbomachinery blisks are very sensitive to mistuning, i.e. any deviation from nominal properties or geometry, which can lead to vibration amplification of some of the blades in the assembly. As a result, high cycle fatigue (HCF) is a major concern for such structures [116], which makes the study of blisk vibrations particularly important. For this reason, several studies have been conducted to predict blisk vibration through the use of simulations [3, 4]. Blisks also present very low mechanical damping, which results in high levels of vibration. Hence, great efforts have been made to design and study various forms of dampers, including ring dampers [56, 57, 59–61]. Ring dampers are typically positioned in a groove manufactured in the disk portion of the blisk, and are shaped like a ring with a cut [130]. Ring dampers rely on the relative motion between the damper and the groove surface to dissipate energy. As a result, the effectiveness of ring dampers is limited because the disk region typically shows little motion, especially for blade dominated modes. Unlike other aerospace structures which are subject to random vibrations [129], turbomachinery blisks are subject to narrow band excitations with specific spatial patterns known as traveling-wave excitations [73]. This type of excitation makes tuned mass dampers (TMDs), or tuned vibration absorbers (TVAs), good candidates for vibration reduction in such structures. Several studies have been carried out in the past on TMDs in applications ranging from space structures [74] to missile launchers [75]. A general overview can also be found in [76]. Some studies focused on the use of Coulomb friction as a method to dissipate the energy that is transferred to the TMD [77, 78, 130], and most of these studies have been carried out only computation-

ally [77, 130]. A study on the application of TMDs to blisks that includes Coulomb friction and a complex geometry is presented in [130], with a focus on numerical simulations rather than experimental validation. However, due to modeling challenges such as those in contact modeling, experimental validation is necessary. The study presented by Hartung et al. [78] introduced an experimental setup for the investigation of TMDs with contacts. The experiment is designed to replicate a 2-DOF lumped mass model, as the elasticity in the system only comes from connecting springs. That study, however, does not capture the effects of the position of the TMD in realistic 3D assemblies or the role that geometry and mode shapes could play in the effectiveness of such TMD.

This paper has two main goals. The first goal is to experimentally and computationally assess the effectiveness of a friction-enhanced TMD applied to a 3D structure. The second goal is to experimentally validate a simulation tool based on the harmonic balance method that is currently used to model nonlinear vibrations in the presence of friction. A steel cantilevered beam is used to mimic the behavior of a blisk blade (Fig. 6.1). An aluminum TMD with a frictional contact is attached to its root to absorb vibration energy and reduce the overall beam vibration amplitude. This setup is proposed as a simplified representation of a TMD hosted on the disk region, far away from the blade tip, where only small motions are present. The experimental results are used to validate the predictive ability of a high-fidelity finite-element model used in combination with a harmonic balance solver.

6.2 Methodology

Experimental and computational studies are carried out using the assembly presented in Fig. 6.1. The first bending mode of the main beam is targeted. Even though the first mode shape is geometrically relatively simple, it is a useful representation of the first bending cantilevered blade mode of a blisk. The TMD is attached to the beam near its root, in

a region of low motion amplitude for the mode being targeted, to simulate the working conditions of such a TMD applied to a blisk.

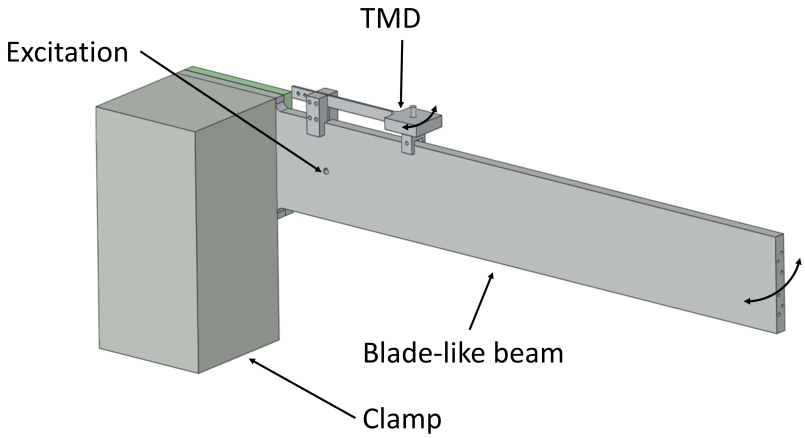

Figure 6.1: Schematic of the experimental setup

6.2.1 Experimental setup

The uniform steel cantilever beam used in the study is connected to a plate bolted on an optical table via a solid steel column. The bolted connections between the beam and the support column, as well as between the plate and the optical table, were designed to reduce frictional dissipation at the interfaces, resulting in a final assembly that shows very little damping, similar to the case of blisks. An electrodynamic shaker is used to excite the structure through a stinger connected to the beam. A view of the experimental setup can be observed in Fig. 6.2. A load cell is placed between the stinger and the beam to measure the input force, and a strain gauge is added to the damper beam to measure the contact normal force, as it can be observed in Fig. 6.4.

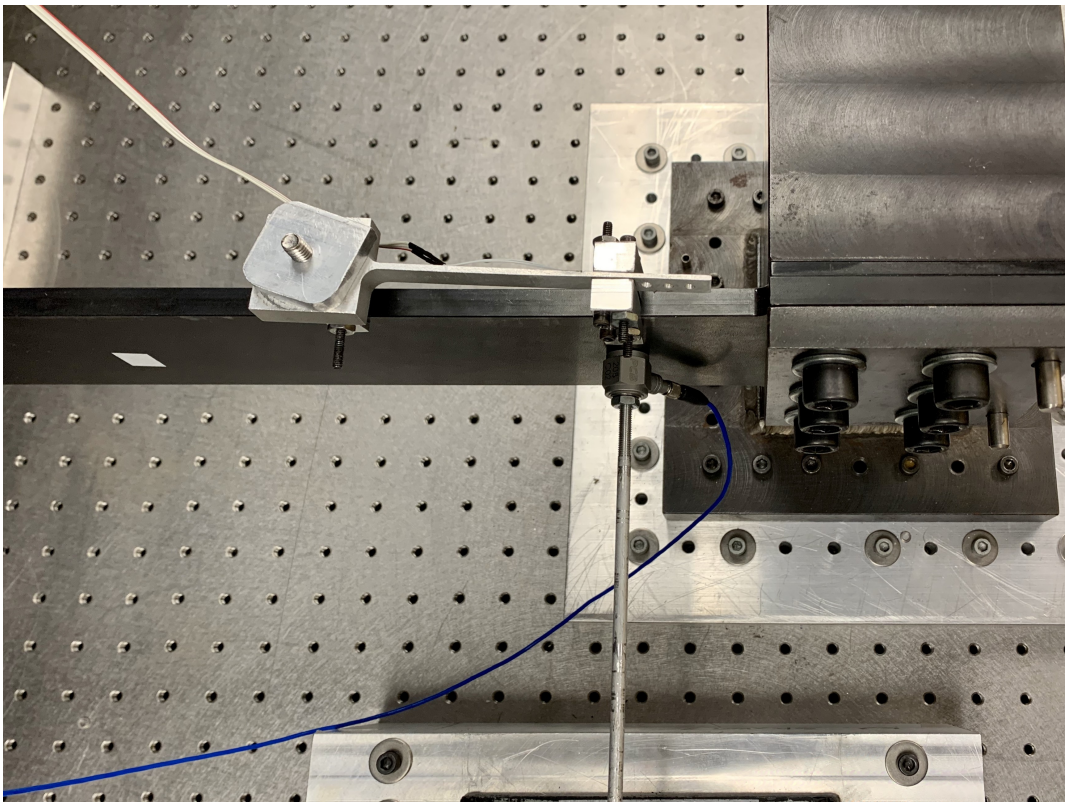

Figure 6.2: Experimental setup

The TMD was designed to have the shape of a cantilever beam (referred to as damper arm) with a tip mass (referred to as damper head), as shown in Fig. 6.4. This design allows to independently adjust the two damper parameters that regulate its natural frequency, namely the bending stiffness and the mass. The damper arm is connected to the beam (i.e., the host structure) using clamp-like mechanisms. This allows easy adjustment of the damper attachment location along the beam, as well as the adjustment of the length of the damper arm, which modulates the bending stiffness and the natural frequencies of the damper. The added mass on the damper head is connected to the damper to allow the targeting of the first bending mode of the host structure, which is close to 30 Hz. The damper head houses a contact element which is threaded onto the damper head. The contact normal load is varied by tightening or loosening the contact element, which is then locked in position by the added

mass, which is also threaded. The contact element consists of a hemispherical surface which realizes an approximate point contact. The contact element rubs against a flat clamp-like structure that can be easily positioned at different points along the beam. To demonstrate the effectiveness of this concept, the damper was clamped near the root of the beam, where there is little motion compared to the tip, with a ratio between tip motion to attachment location motion approximately equal to 70. This ensures that the damper effectiveness is driven by the tuning of the damper rather than just the motion of the beam.

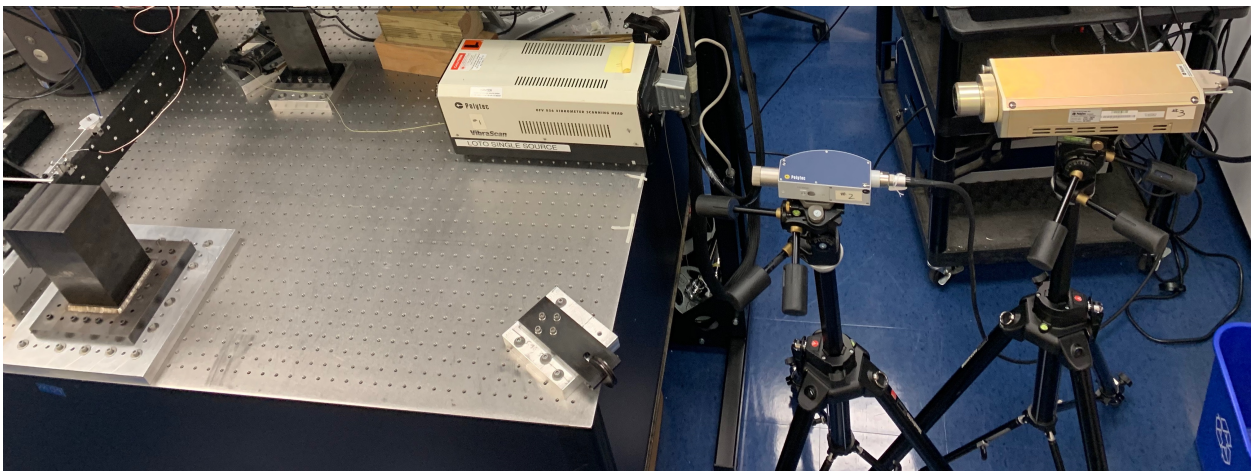

Figure 6.3: View of the 3LDV setup

The vibration amplitude is measured using three Laser Doppler Vibrometers (LDVs), positioned as shown in Fig. 6.3. As it is possible to see from Fig. 6.3, several measurement points, marked with reflective tape, are available along the beam and the damper. For simplicity, the vibration of the beam is measured at point A, which is close to the tip of the beam, in the direction orthogonal to the beam surface. The motion of the damper head is measured at point B, and the motion of the contact contact element is measured at point C, as shown in Fig. 6.4.

A sweep in the excitation frequency is typically applied to obtain the frequency response function of the assembly. Due to the very low damping of the system, the response at each frequency takes a long time to reach steady state. For this reason, a stepped sweep in

frequency is used, i.e. the forcing is kept at a constant frequency until the vibration reaches steady state, then a sample is recorded, and then the frequency is incremented. This method guarantees that the steady state response is captured in the absence of transient effects. The frequency resolution of the curve is up to 0.01 Hz in the proximity of the resonance.

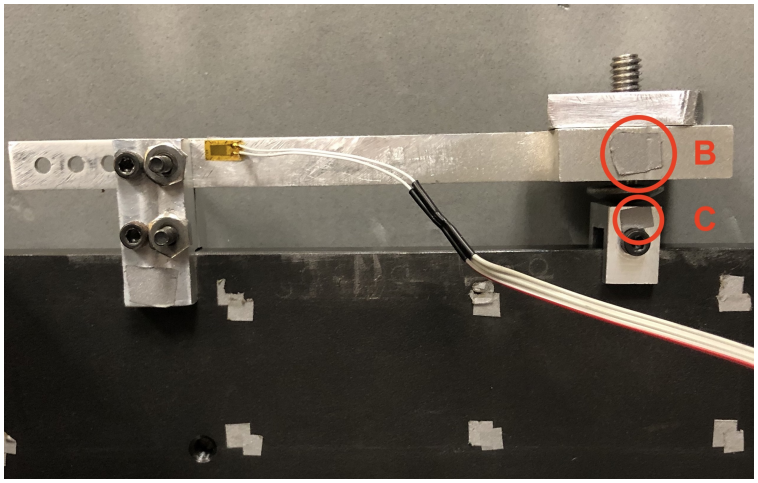

Figure 6.4: Damper showing the points used for measurement

The damper was designed to be adjustable in its length to coarsely adjust its frequency, while the mass on top of the damper head is used as to finely adjust its frequency to match the one of the beam. This is achieved through the use of a mass calibrated for that purpose.

6.2.2 Simulation model

The computational study of the experimental setup was carried out using a high-fidelity finite-element model, presented in Fig. 6.1. The assembly is modeled using bonded contacts at the interfaces between different components, with the exception of the contact interface between the damper contact element and the contact surface. The nonlinear contact, located just between point B and C in Fig. 6.4, is modeled using a Coulomb friction model, and the solution is obtained using the harmonic balance method [126, 127]. To reduce the number of DoFs and the computational cost associated with the solution of the system, Craig-Bampton component mode synthesis (CB-CMS) [42] is used. Only a few selected nodes are preserved

as master nodes, namely the contact pair, the node at the measurement location, and the forcing node, which is located where the stinger connects to the beam. The number of master DoFs retained is thus 12, and the number of slave modes is 50. As a result, the size of the model is reduced from the initial $409,278$ DoFs, and $136,426$ nodes, to only 62 DoFs. Similar to the case presented in [130], the equations of motion (EOMs) for the system can be written as

$$\mathbf{M}\ddot{\mathbf{x}} + \mathbf{C}\dot{\mathbf{x}} + \mathbf{K}\mathbf{x} = \mathbf{f}_e + \mathbf{f}_n(\dot{\mathbf{x}}, \mathbf{x}), \tag{6.1}$$

where $\mathbf{M}$, $\mathbf{C}$ and $\mathbf{K}$ are the mass, damping, and stiffness matrices obtained in the absence of contacts, $\mathbf{f}_e$ is the vector of external periodic forces acting on the structure, and $\mathbf{x}$ is the vector of generalized coordinates. The vector $\mathbf{f}_n$ represents the nonlinear forces, which are due to the contact between the two components. The damping matrix $\mathbf{C}$ is assumed to be proportional to the stiffness matrix with a proportionality factor β, as $\mathbf{C} = \beta\mathbf{K}$, where $\beta = \frac{2\zeta}{\omega}$.

6.2.2.1 Simulation model tuning

Some of the model parameters must be identified to match the experimental conditions. As it is possible to notice from Fig. 6.1 and Fig. 6.2, some of the experimental features are not present in the model. For example, the compliance of the metal plate that is used to attach the beam support to the optical table is assumed to be negligible. Some of the features of the experimental beam as well as the bolts are not modeled. Furthermore, the mass of the damper contact element and the damper tuning mass are not experimentally measured. As a result, the finite-element model initially presented a small deviation in the natural frequencies compared to the experimental measurements. To overcome this discrepancy, two model parameters are adjusted, namely the mass m_{dm} of the damper tuning mass located on the damper head, and the beam stiffness multiplier α, which effectively lowers or increases

the stiffness of the entire assembly. In addition, the damping ratio ζ must be identified. The parameter identification is carried out by comparing the computational and experimental results obtained for the two linear cases: damper completely *free* and damper completely *stuck*. The damper is said to be *free* when there is no contact engaged. The damper is said to be *stuck* when the contact is engaged and the normal load F_0 is large enough to prevent the relative motion between the contact element and the contact surface.

To minimize the effects of nonlinearities coming from the beam clamp, which could arise in the case of large vibration amplitudes, the tuning of the model was carried out at low vibration amplitudes, obtained with $F = 3.4\,\mathrm{N}$. The beam frequency response is shown in Fig. 6.5b and highlights the good agreement between computational and experimental results after the model has been tuned. Please note that the difference between the two sets of results is larger for the *free* case. This is likely because the interaction between host structure and the TMD is very sensitive to the tuning quality, i.e. the match between damper and host structure frequencies. In particular, the frequency split between the two peaks present in the *free* case is not perfectly captured. The same is observed for the damper response (point B in Fig. 6.4), which is shown in Fig. 6.5a. Because the curve fit was achieved with only two parameters, the agreement between the two curves is considered satisfactory. The parameters that were used to tune the model are presented in Table 6.1.

m_{dm}	$18\,\mathrm{g}$
α	0.936
ζ	0.09%

Table 6.1: Simulation parameters used to tune the model

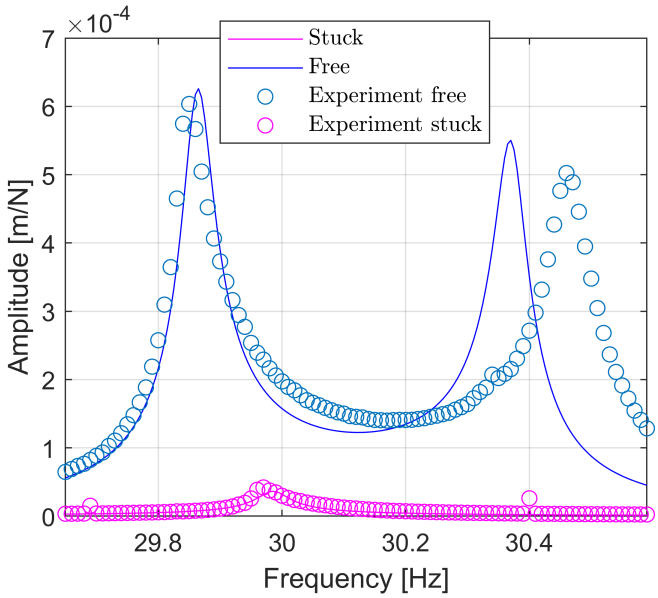

(a) Damper response

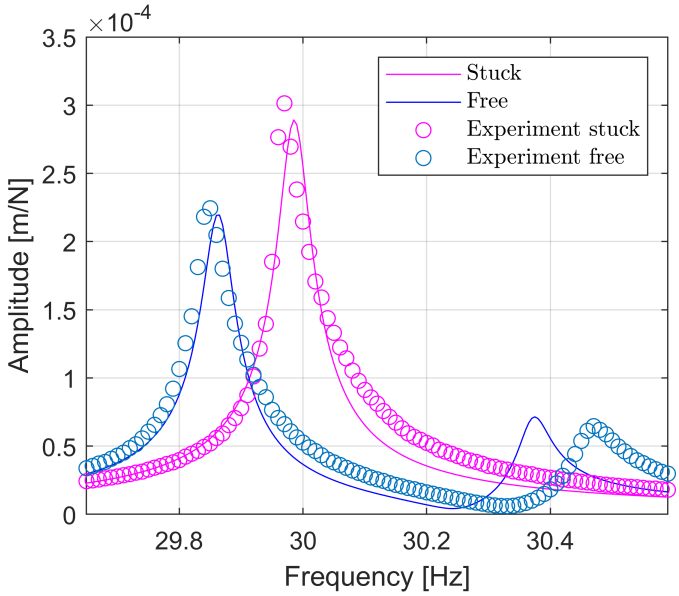

(b) Beam response

Figure 6.5: Comparison between numerical and experimental solution for the linear cases

6.3 Results and discussion

Several sets of results are presented in this section. The simulation results are ordered based on the contact normal load value F_0 used, while all other quantities are kept constant.

The Coulomb friction coefficient is assumed to be $\mu = 0.2$. The nondimensionalized vibration amplitude $\frac{|x|}{F}$, where F is the amplitude of the forcing, is used to compare the results obtained experimentally to the ones obtained through simulation.

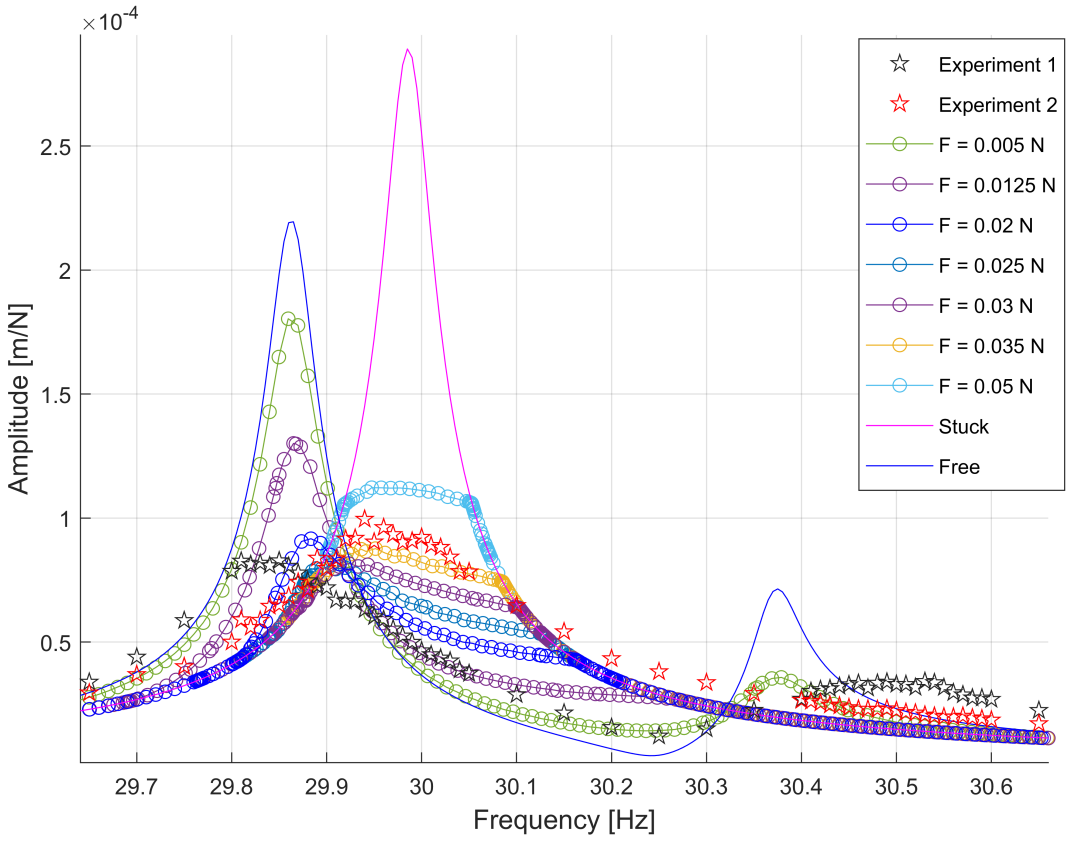

Figure 6.6: Beam response: nonlinear comparison between numerical and experimental solution

A detailed comparison between different beam responses is shown in Fig. 6.6, where it is possible to notice that the results in the presence of contact show a substantial vibration reduction compared to both the *stuck* and the *free* results. Several experiments were conducted with different normal load values. The results reported as *Experiment 1* and *Experiment 2* in Fig. 6.6 showed the most significant vibration reduction in the beam. The maximum amplitude reduction observed experimentally is 67.5% and 56.7% compared to the *stuck* and *free* results, respectively. The damper response is shown in Fig. 6.7. It can be noticed

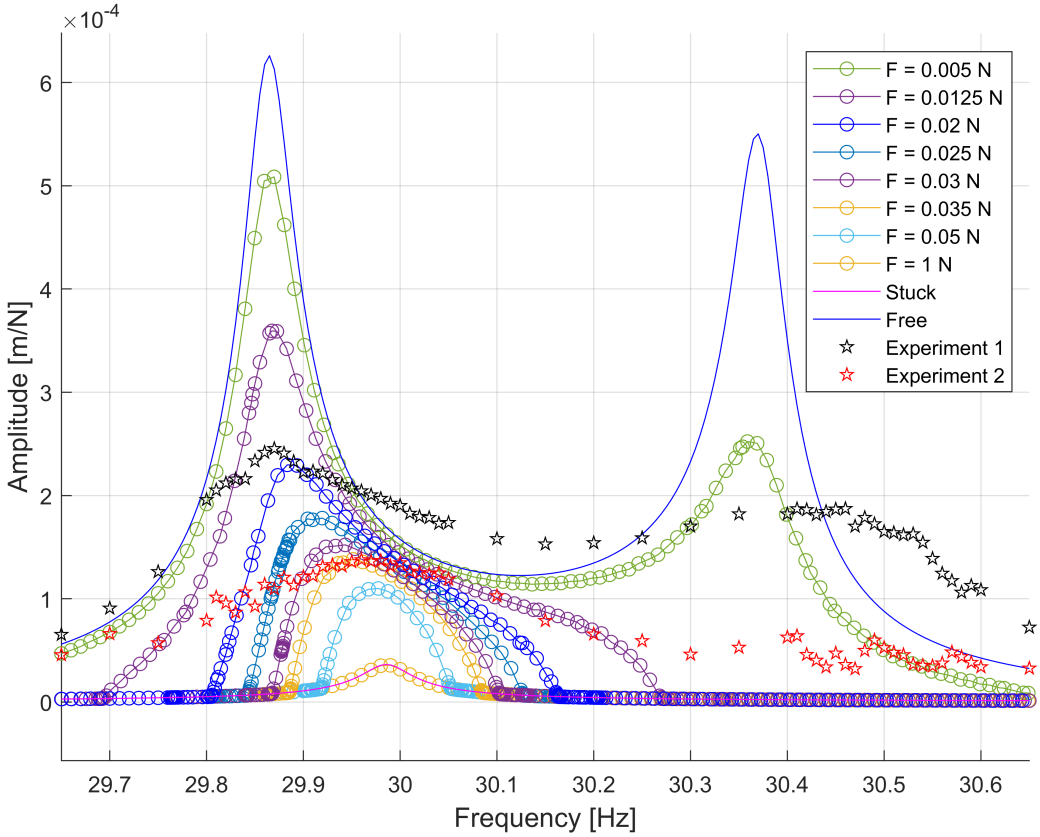

Figure 6.7: Damper response: nonlinear comparison between numerical and experimental solution

that as the contact normal load becomes smaller, the vibration amplitude of the damper increases significantly, by an order of magnitude. It is possible to notice that the simulation results are obtained for a broad range of normal load values, ranging from $F_0 = 0.005\,\mathrm{N}$ to $F_0 = 1\,\mathrm{N}$, and that the nonlinear response calculated using harmonic balance tends to match the linear response as F_0 approaches zero or becomes large. The value F_0 was not measured in experiments. Thus, a direct comparison cannot be made yet. What can be observed, however, is that there is a qualitative agreement between experimental and numerical data.

6.3.1 Contact analysis

The use of two vibrometers to measure the contact and target locations (points B and C in Fig. 6.4) is necessary to capture the contact behavior. By taking the difference of the two signals it is in fact possible to examine the relative displacement and relative velocity of the contact points. This is particularly interesting especially in those cases where irregular contact appears due to wear. The hemispherical screw head is made of steel, while the contact element is made of aluminum. This results in significant wear visible on the flat surface, as it can be seen in Fig. 6.9. The creation of ridges on the contact surface create the presence of irregularities in the relative displacement and velocity. This can be seen in Fig. 6.8a, that shows the state plot for the contact, i.e. the relative displacement and velocity $x_r, \dot{x}_r$. To limit the effect of noise, the state plot was obtained by taking the sample average over several periods of the time domain signal. The presence of an irregularity at a constant position indicates the presence of a surface defect. The time domain velocity for a period is shown in Fig. 6.8b.

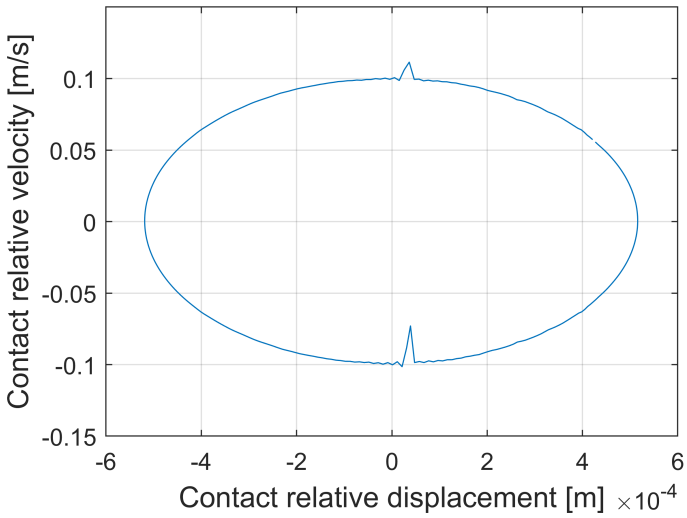

(a) State plot of the contact displacement and velocity

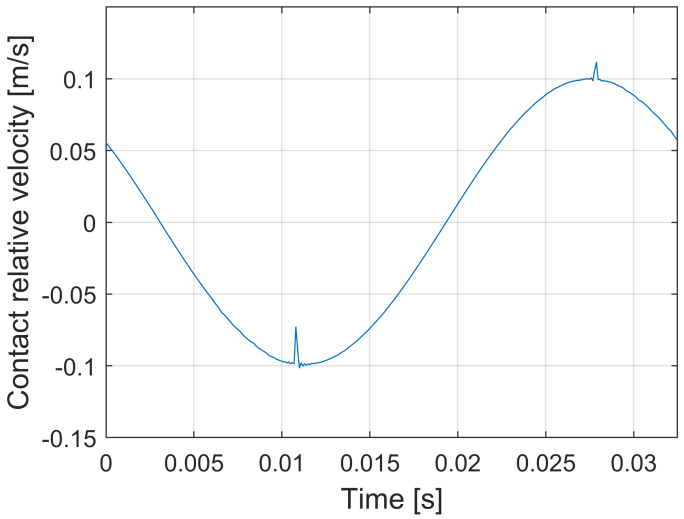

(b) Velocity signal

Figure 6.8: Contact analysis: relative motion and relative velocity

6.3.2 Effectiveness

Through the use of simulation, it is possible to investigate more in depth the effectiveness of the damper as a function of contact parameters, namely as a function of the nondimensional microslip parameter $\rho = \mu F_0/F$, which governs the behavior of the nondimensional

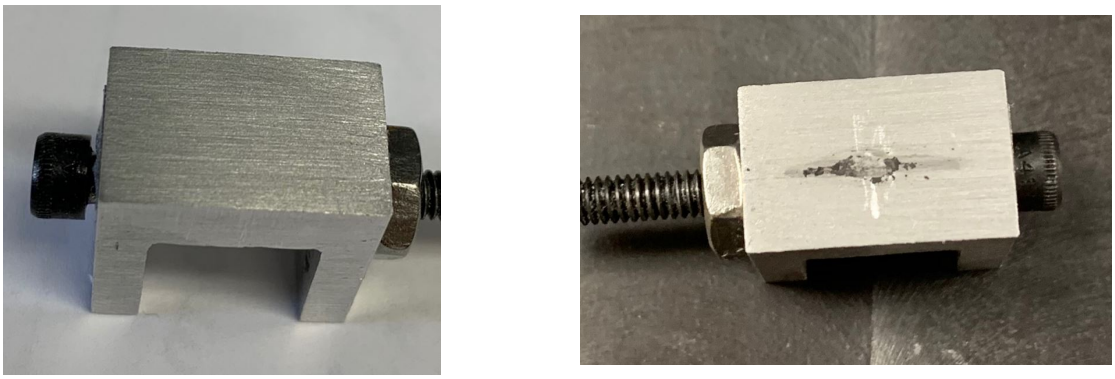

Figure 6.9: Flat contact element before use and after two days of testing

response x/F [26].

It is possible to notice from Fig. 6.10a that the minimum vibration amplitude that can be achieved is 8.1×10^{-5} m/N, which is very close to the minimum value of 8.3×10^{-5} m/N that was found experimentally. This is a very good indication of the fact that even though the contact behavior is only qualitatively captured, as it can be seen in Fig. 6.7, the predicted energy dissipation is very close to the one obtained in the experiment, as well as the beam behavior, shown in Fig. 6.6. Another interesting insight into this phenomenon is provided by examining the energy dissipation distribution, which can be divided between linear and nonlinear. As shown in Eq. 6.1, the energy dissipated per cycle by nonlinearities can be calculated as $E_{nl} = \int_0^T \mathbf{f}_n(\dot{\mathbf{x}}, \mathbf{x})^T \cdot \dot{\mathbf{x}} \, \mathrm{d}t$, and it is caused by the presence of the frictional contact. The linear component is provided by the viscous damping term $E_l = \int_0^T \dot{\mathbf{x}}^T \mathbf{C} \dot{\mathbf{x}} \, \mathrm{d}t$. The two components of the total energy dissipated are plotted as a function of the parameter F_0/F in Fig. 6.10b-c respectively. Interestingly, the maximum amplitude reduction is achieved when the ratio between E_{nl} and E_l is largest, as it can be seen from Fig. 6.10d.

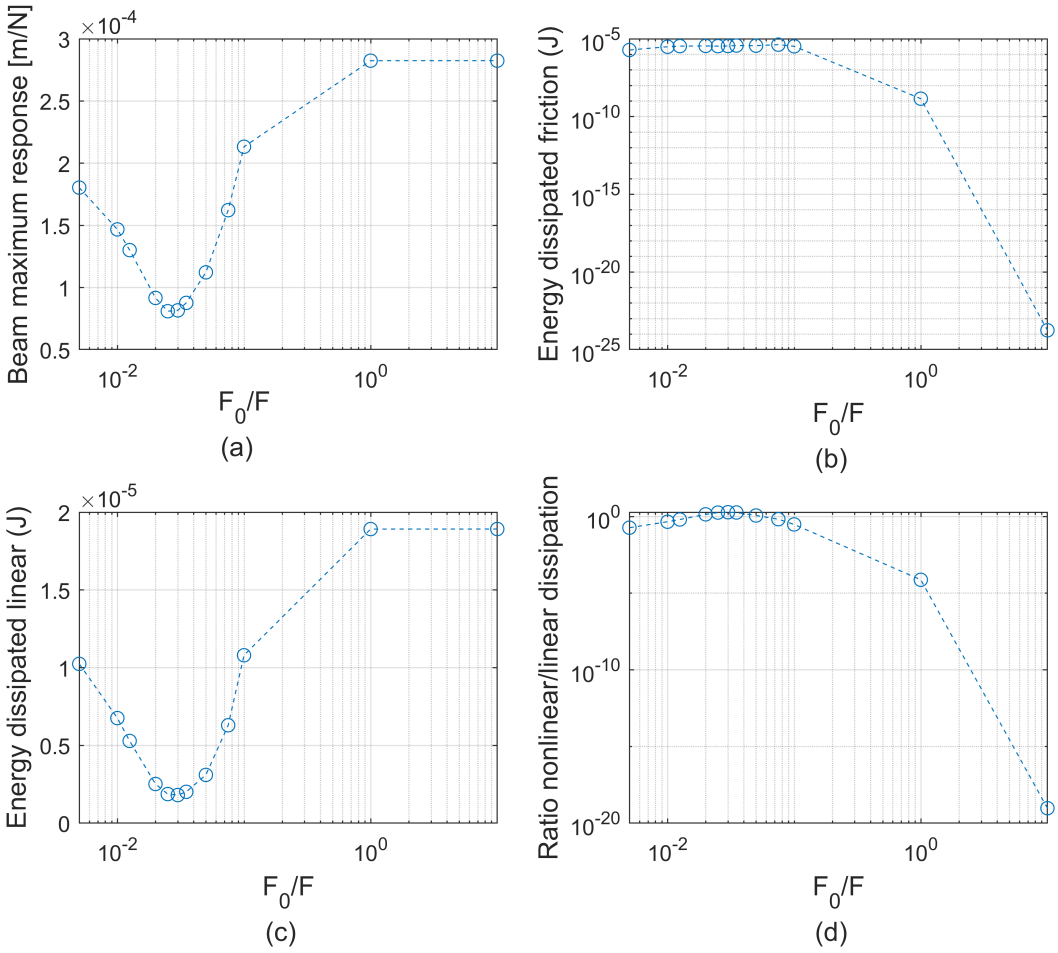

Figure 6.10: Parametric study of the maximum amplitude reduction as a function of the parameter $\frac{F_0}{F}$

6.4 Conclusions

In this paper, an experimental and numerical study was presented to assess the effectiveness of a tuned mass damper with friction contacts for damping blade-like structures. Experimental results were compared to numerical results obtained using the harmonic balance method for the solution of the nonlinear vibration problem. The experimental results obtained demonstrate that such a tuned mass damper concept could be used to effectively

lower the vibration of a lightly damped structure even if the attachment location shows little motion. Simulation results showed good qualitative agreement with experimental results, validating the simulation models and techniques used.

In future studies, the normal load F_0 present at the contact in the experiment could also be measured, with the aim of introducing a quantitative comparison between simulation and experimental results. A study on the effect of damper positioning on its effectiveness could also be carried out, to identify the minimum vibration amplitude at the attachment location that is required to obtain a significant amplitude reduction. Furthermore, more complex modes, as well as higher frequencies could be targeted to explore the range of effectiveness of the proposed damper. These studies will help clarify the direct applicability of this damper concept to blisks and other lightly damped structures in which dampers are constrained to be situated in regions of low motion.

CHAPTER 7

A Friction-Enhanced Tuned Ring Damper for Bladed Disks

This chapter introduces a new type of damper for turbomachinery blisks. The major pitfalls of the damper concepts currently employed are two: the low level of relative motion that is available at the damper attachment location, and the inability to control the preload at the frictional interface. To address these issues, the proposed damper is designed as a tuned vibration absorber, which allows energy transfer from the blades to the damper provided that the natural frequency of the damper is close to that of the host structure. Thanks to the enhanced energy transfer, the damper can experience increased relative motion. Frictional contacts are then included to dissipate the energy transferred to the damper. The control of the contact preload is also important, as the centrifugal loads acting on the damper are extremely large and could result in the damper being stuck in its groove and not dissipating energy. These two requirements result in competing priorities. The damper structure must be stiff enough to withstand centrifugal loading without affecting the preload too much. However, it also must be compliant to make sure that its natural frequencies can match the ones of the host structure. For this reason, the proposed damper involves a complex geometry that is stiff in the radial direction and softer in the circumferential direction, which is the direction of the relative motion. A model of the damper is created to damp the vibration of

a realistic blisk based on the NASA Rotor 67. The effectiveness of the damper is investigated using high fidelity finite element models. Due to the nonlinear nature of the contact, the equations of motion are solved using harmonic balance, and the size of the (linear part of the) system is reduced using Craig- Bampton component mode synthesis. The frequency response of the system is obtained to analyze the effectiveness of the proposed design. Preliminary results show the potential of this technology for structures with such low damping.

7.1 Introduction

The adoption of integrally bladed rotors, or blisks, in turbomachinery has been increasing due to improvements in performance and reduction in the number of components compared to traditional rotors [1]. In operating conditions, bladed disks must withstand large centrifugal forces, high temperatures, and blade vibrations caused by upstream flow perturbations. The presence of flow forcing is particularly dangerous because the combination of the cyclic symmetric design of blisks and their inherent mistuning (i.e., small deviations from the nominal design) makes them prone to vibration localization[4, 5]. Unlike traditional bladed disk assemblies, in which blades are connected to the disk portion using frictional joints, blisks are manufactured in one piece. The lack of frictional interfaces in blisks results in lower damping, which in turn causes larger vibration amplitudes[1, 4]. The presence of high steady stresses and vibration, combined with the large numbers of cycles that blisks blades must withstand, can lead to blade failure due to high cycle fatigue[7]. As a result, a great deal of effort has been made to study and mitigate blisk vibrations. Many studies focused on improving simulation tools to study mistuned blisks vibration response [3, 4, 112, 114]. Other studies focused on the development of different damping mechanisms for bladed disks, many of them involving friction and contacts[3, 52]. Examples include ring-like dampers[56, 57, 59, 62–64] and shrouds[26, 58], both of which dissipate energy via friction. However,

the effectiveness that ring dampers provide can be limited because they rely on the relative motion present between a damper and its groove, which can be very small when blade to disk coupling is low[62], or in blade dominated modes. As an example, the maximum vibration reduction obtained for $EO = 3$ in the study presented in [59] was 13%, much smaller than the 37.9% observed in the same study for $EO = 1$. The same concept can be found in applications involving gears [65–67]. In a recent study [65], an assessment of the effectiveness of such damper was carried out, resulting in a maximum reduction approximately equal to 9%.

To increase the relative motion present at the damper location, recent studies proposed the use of a tuned vibration absorber (TVA) concept[73, 130] to transfer energy from the blades to the damper region. TVAs are typically used in narrow-band forcing applications to shift the resonance of the structure away from the forcing frequency. TVAs effectiveness depends on the accuracy of their tuning, i.e. how close their natural frequency is to the target frequency to be damped.

In [73], the application of a tuned vibration absorber to a cyclic structure is investigated, highlighting the impact of correct nodal diameter targeting, damper location and material damping on the overall effectiveness. However, that study provides limited insight into the feasibility of the concept, because it only uses a lumped mass model. In [130], an academic blisk's finite element model is used to simulate the effect of a tuned ring damper concept on the blisk response in the presence of contact nonlinearities. That study, however, utilizes tuning obtained by artificially modifying physical parameters of the damper material, which may not be feasible. The impact of the contact preload, which varies with the rotational speed, is also not explored. The same authors also experimentally investigated the effectiveness of the friction-enhanced TVA concept using a mock-up test rig with a cantilevered beam, showing promising results[131].

The aim of this paper is to further expand the understanding of novel damping mech-

anisms for blisks, focusing in particular on dampers based on the TVA concept. First, the constraints present in the design of such dampers are explored, to lay the foundation for the design choices. Second, the blisk considered in the study is presented, to highlight its main features and the targeted modes. Finally, the simulation techniques used and the simulation results are discussed.

The blisk model used in this study was provided by The Ohio State University (OSU) Gas Turbine Laboratory (GTL). A damper based on the design presented herein is scheduled to be tested as a part of a study on mistuning and damping[79].

7.2 Methodology

In this section, the concepts used in design, as well as in simulation, are introduced and explained.

To achieve a significant level of vibration reduction through friction, it is necessary to observe the relative motion between the damper groove and the damper. However, in typical blisks, the ratio between the motion at the blade and the motion at the damper location for any given mode is very large, especially for blade dominated modes. A possible solution can be found through the use of the TVA concept, which transfers energy from the host structure to the damper, or vibration absorber. For this reason, the damper presented in this paper is designed to have one of its natural frequencies close to the ones of the blisk, which will result in high vibration amplitude levels in the damper region. The *free* damper natural frequencies, i.e. obtained in the case where the contact is not engaged, are used for tuning because those frequencies are more precisely measurable and allow for an easier targeting of the modes that require damping. In fact, the *free* frequencies are typically lower than the *stuck* frequencies, making it possible to target low frequency families. High frequency families can still be targeted by adopting a stiffer design. Furthermore, the estimation of contact

stiffness parameters can be challenging, and they potentially affect the natural frequencies of the *stuck* case, i.e. the case in which the contact is engaged and no slip is permitted, making it difficult to obtain a precise tuning. As a result, the *free* natural frequencies were chosen for tuning.

The effectiveness of friction based damping mechanisms is typically presented as a function of the nondimensional microslip parameter $\rho = \mu \frac{|\mathbf{F}_0|}{F}$, where μ is the coefficient of friction, $|\mathbf{F}_0|$ is a representative normal load magnitude defined as the sum of the magnitudes of all the contact normal forces, and F is the forcing amplitude[58]. The two parameters that exhibit the largest variation in operating conditions are F and $|\mathbf{F}_0|$, due to changes in the amplitude of the forcing and in the rotational speed. Traditional ring dampers, like the one shown in Fig. 7.1, present a cut, which allows them to expand radially as the centrifugal forces increase due to rotation. Since in operating conditions the ring would be hosted in the blisk groove and the damper is compliant, the contact forces at their interface increase with the rotational speed, leaving little to no control to the designer over the contact preload. For this reason, the damper presented here was designed in such a way that could allow preload control, as well as frequency control.

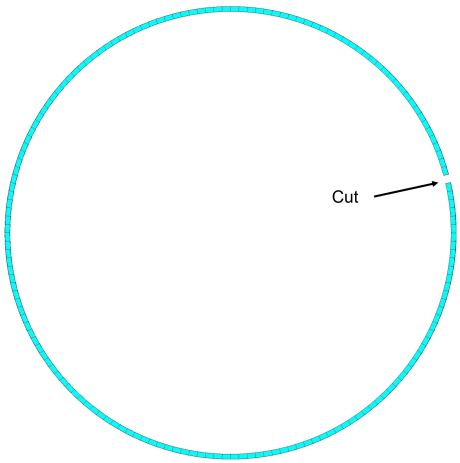

Figure 7.1: Geometry of a traditional cut ring damper

7.2.1 Design constraints and proposed solution

The damper for this study was designed for the NASA Rotor 67 model presented in[79]. A sector of the model is shown in Fig. 7.2. Note that this blisk design has large disk stiffness, provided by the presence of an arm-like protrusion on the right side, which makes it challenging for traditional ring dampers to be effective. The damper radial extension, as well as its axial dimension, are both limited by the position of the groove. The full wheel representation of the assembly can be observed in Figs. 7.4-7.5.

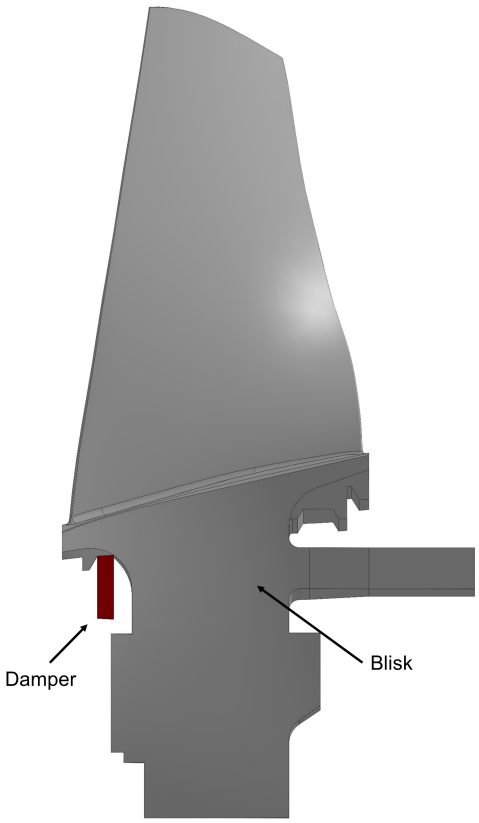

Figure 7.2: Sector level representation of the blisk considered in this study, with the damper highlighted in red

Another challenge is to preserve damper effectiveness across different operation regimes and frequency ranges, as well as nodal diameters. To ensure effectiveness at different ro-

tational speeds, the preload, which is the quantity most affected, should be kept relatively constant, or it should be changed in a controlled fashion. To target multiple nodal diameters at similar frequencies, the damper should have high modal density and show mistuning or a non-cyclic symmetric structure. It can also be useful for the damper to have a flat family, so that it can target multiple nodal diameters (ND) in blade dominated families.

A sector level view of the proposed damper is presented in Fig. 7.3. It is composed of a casing, used to hold the system in place, and a slender oscillator that rubs against its casing. The periodicity of damper oscillators and the number of blades do not have to be the same for the concept to work, but in this study we examine the case of a blisk and damper with identical number of sectors. Each oscillator is shaped as a thin beam connected to a tip mass. This design was introduced to lower as much as possible the damper frequencies so that the broadest possible range of blisk modes, and thus natural frequencies, could be targeted. The frequency of the damper can be lowered further by increasing the tip mass or lowering the thickness, and increased doing the opposite. The tip mass is also the rubbing element. The two contact surfaces, namely the oscillator and casing surfaces shown in Fig. 7.3, have been designed to maintain the preload approximately constant during the vibration of the oscillator.

The advantages that this design presents compared to traditional ring dampers are the following:

1. The design with oscillator beams makes it easy to tune the free frequencies of the damper to match the frequencies of the blisk. The tuning is possible by changing tip mass and beam length and thickness.

2. Preload variation due to change in centrifugal load, or RPM, is mitigated by the presence of the supporting oscillator beam, which is stiff in the radial direction. The preload is thus a designer choice and could be controlled by adjusting the clearance

and/or deformation due to centrifugal loads.

3. Once energy is transferred to the damper, alternative solutions could be explored to dissipate it, e.g damping coatings and impacts.

4. Contact interface wear, if present, is expected to be confined to the damper, in particular at the casing and oscillator contact interface, leaving the blisk groove in its original condition. As a result, the entire damper can be substituted once its effectiveness is lowered due to wear.

The tuning is achieved by separately tuning the damper structure shown in Fig. 7.3 to match the frequencies of the blisk. The damper interface contacting the blisk groove is considered to be fixed, i.e. with no motion, for tuning purposes.

The results after tuning are presented in Figs. 7.4-7.5. The blisk dominated mode being targeted is shown in Fig. 7.4, and the damper dominated mode is presented in Fig. 7.5. By looking at the modal analysis of the entire assembly, it is possible to notice that there is a small frequency difference $\Delta f_n = 1.8Hz$ between the two modes. The presence of a frequency split between the two is in part caused by the fact that the damper is tuned. In fact, based on the theory of the tuned vibration absorber [68, 73], it is expected to obtain two modes in lieu of the single one that was previously found in the host structure. However, it can be noticed that the mode in Fig. 7.4 shows very little motion in the damper, which potentially indicates non optimal tuning. This is due to the fact that blisk and damper natural frequencies experience a small variation once the blisk and damper are assembled together. The presence of imperfect tuning is having to do with the fact that the damper tuning was done separately without the blisk. By using a coupled approach for the tuning, it could be possible to achieve a better and more balance tuning, in which the damper participation factor is maximized.

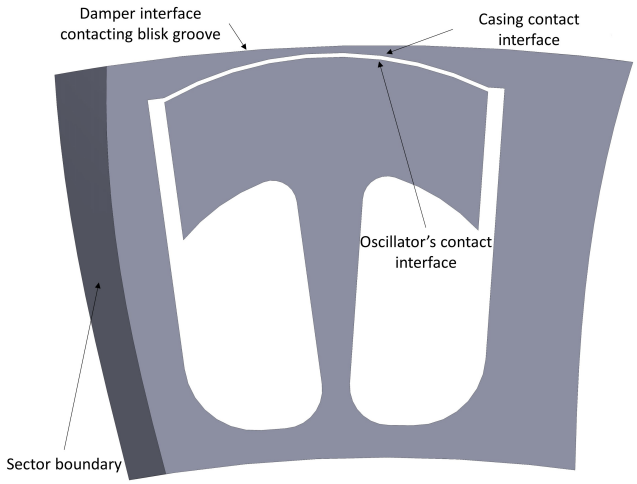

Figure 7.3: Sector level representation of the damper used in this study

7.2.2 Simulation model

In this section, the details of the simulation model used for forced response calculations is presented. The blisk is based on NASA Rotor 67, and it has $N = 22$ blades. The simulation approach is similar to the one shown in [3, 130]. A high-fidelity finite element (FE) model is created to represent the blisk-damper assembly. All calculations are carried out using the full wheel model in order to capture the effects of mistuning where presents. Due to high computational cost associated with the solution of the nonlinear simulations, the Craig-Bampton component mode synthesis (CB-CMS) [42] and the harmonic balance method [3] are used. The initial FE model with full damper and blisk has $4,297,416$ DoFs, which are significantly reduced preserving a single forcing and response nodes at the blade tip for each blade, 55 contact and target nodes for each sector, and 200 slave modes.

The equations of motion (EOMs) for the system can be written as

$$\mathbf{M}\ddot{\mathbf{x}} + \mathbf{C}\dot{\mathbf{x}} + \mathbf{K}\mathbf{x} = \mathbf{f}_e + \mathbf{f}_n(\dot{\mathbf{x}}, \mathbf{x}), \tag{7.1}$$

where $\mathbf{M}$, $\mathbf{C}$ and $\mathbf{K}$ are the mass, damping, and stiffness matrices, $\mathbf{f}_e$ is the vector of external

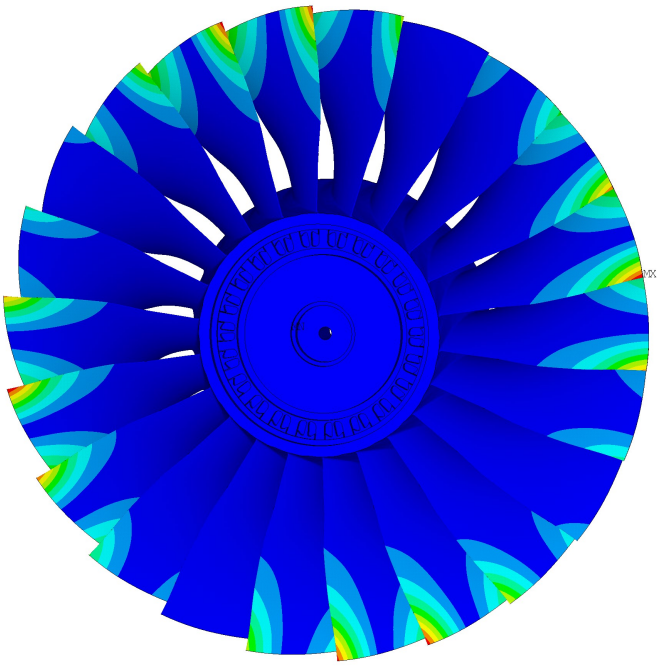

Figure 7.4: Targeted blisk mode with the damper shown in Fig. 7.13, having natural frequency $f_n = 1551.3\,\text{Hz}$

periodic forces acting on the structure, and $\mathbf{x}$ is the vector of generalized coordinates. The vector $\mathbf{f}_n$ represents the nonlinear forces, which are due to the contacts. Proportional damping is used, and the damping matrix can be written as $\mathbf{C} = \beta\mathbf{K}$, where $\beta = \frac{2\zeta}{\omega}$, ζ being the damping ratio. Since the forcing frequency ω varies in the range $[\omega_{min}\ \omega_{max}]$, β is defined using the average frequency over the excitation range, as $\beta = \frac{4\zeta}{\omega_{max}+\omega_{min}}$.

A relative coordinate formulation is used to describe the displacement at the contact interface, similar to [26, 125], and the 1D node-to-node contact model presented in [26, 61] is used, where all pairs of nodes having coincident location form a contact pair. Each contact pair i is assigned tangential contact stiffnes $k_{i,x}$,$k_{i,y}$ and normal contact stiffness $k_{i,z}$, which are essentially 1D springs in the local coordinate system. Based on normal and tangential relative displacements, the contact condition is established.

There are two linear limit cases for the contact status. The linear contact status can be *stuck* or *free*. As a reference for comparison for the nonlinear simulation results, the *stuck*

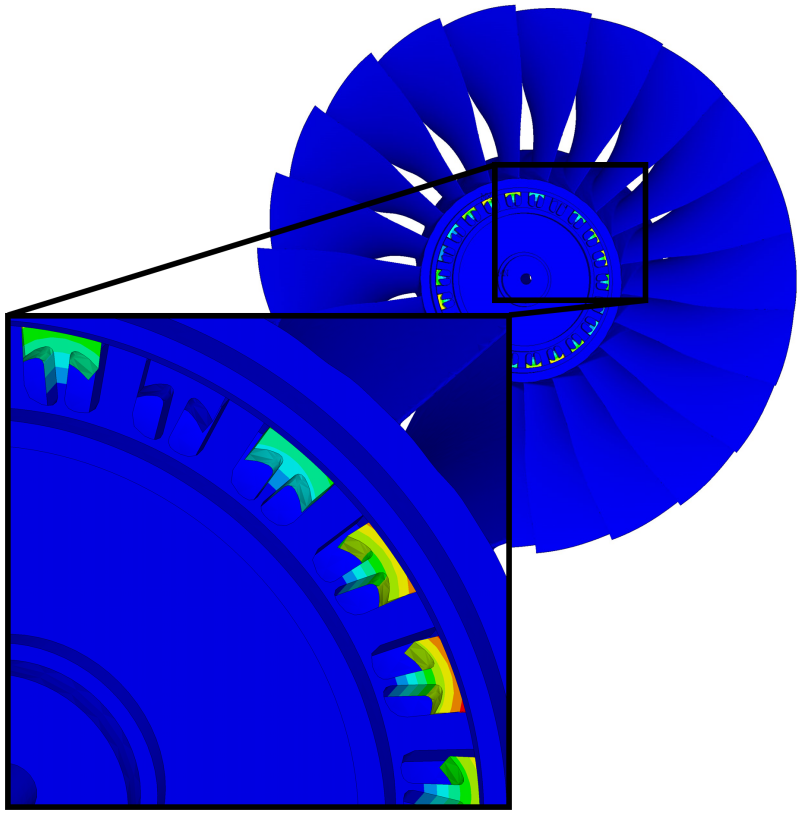

Figure 7.5: Damper mode of the damper shown in Fig. 7.13, having natural frequency $f_n = 1553.1Hz$

and *free* results are used. In the *free* case, the two contact interfaces presented in Fig. 7.3 are completely disconnected and do not interact. In the *stuck* case, each node pair on the contact surface is always connected by the springs $k_{i,x}$,$k_{i,y}$,, $k_{i,z}$. The damper interface contacting the blisk groove, shown in Fig. 7.3, is considered to be always *stuck*, i.e. connected to the groove by means of linear contact springs. This implies that there is no energy dissipation at the blisk groove, which is based on the assumption that most of the energy dissipation will happen between the oscillator and casing, also shown in Fig. 7.3, rather than at the blisk-damper interface. For a more in-depth explanation of the contact modeling please refer to [3].

The damper presented in Fig. 7.3 shows a gap between the two contact surfaces, which

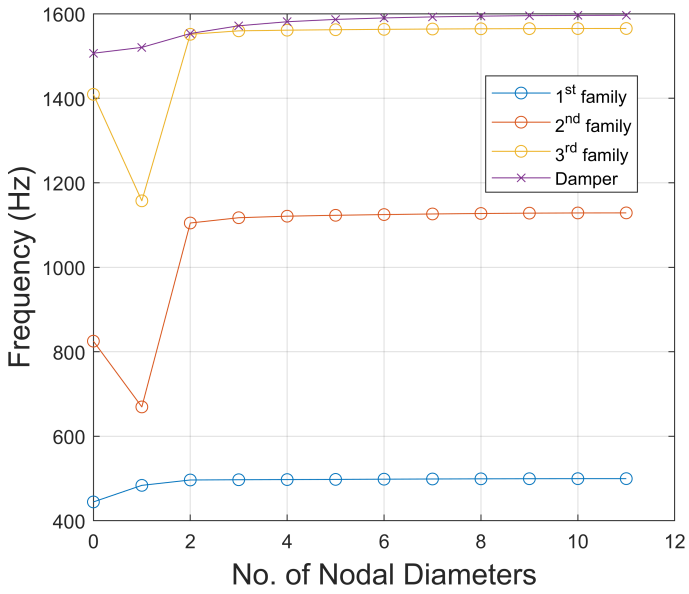

Figure 7.6: Frequency vs. nodal diameter plot for the blisk with a tuned damper

would not be present in operating condition, due to either centrifugal deformation or prestress applied in the manufacturing or assembly phase. In the computational model the gap is assumed to be absent, and the preload is then applied at each node pair in local relative coordinates in the direction normal to the contact surface. The local coordinate system varies at every node pair, and it is defined according to the contact surface geometry.

7.3 Results

To evaluate the effectiveness of the proposed damper, the model previously created is used to simulate the response of the blisk to traveling-wave excitations[3]. One node per blade is excited, and the response amplitude is calculated for the same node. The effect of nonlinearities is captured using harmonic balance (HB) [3]. Only one harmonic was preserved in the HB calculations. The mode targeted, shown in Fig. 7.4, has $ND = 2$, and it belongs to the 3^{rd} family. An excitation with $EO = 2$ is applied to the blade tips. The force applied at each node is $F = 10\,\mathrm{N}$, and the coefficient of friction used is $\mu = 0.2$. The baseline

damping considered is $\zeta = 0.03\%$. First, the case of a tuned blisk with the damper shown in Fig. 7.7 will be introduced. Such damper was obtained by removing a sector from the full ring damper that was tuned to the blisk targeted frequency, as presented in the previous section and in Figs. 7.4-7.5. The removal of a sector is necessary to allow the installation of the damper in the blisk groove. However, the absence of such sector is a source of large geometric mistuning, as will be shown by the results. Then, a study of the effect of overall damping on damper effectiveness will be introduced. It is particularly important for the proposed damper to be effective in those cases where other damping mechanisms, such as aerodynamic damping, are absent, which could be due for example, to flutter [132, 133]. A brief study will be carried out with the aim of quantifying the equivalent damping ζ_{eq} provided by friction in the proposed damper. Lastly, a study with a full damper without a missing sector will be presented to isolate the effects of the damper from the ones of mistuning.

7.3.1 Forced response results

The nonlinear blisk response is shown in Fig. 7.8, and it includes both linear limit cases in which the contact surfaces are *stuck* or completely *free*. Only the response envelope is shown, i.e. the maximum vibration level across all blades. The response in the proximity of the resonance is magnified to highlight the amplitude variation due to the change in the microslip parameter ρ. The variation of the microslip parameter ρ is obtained by varying the preload.

It is important to notice that there is a difference, or split, between the *free* and *stuck* curves, both in terms of overall shape and damped natural frequency, where the maximum response occurs. Previous studies highlighted the correlation between the difference in natural frequency and the effectiveness of the damper [64]. The presence of the split is crucial for the damper to be effective, as maximum vibration reduction is typically achieved as the

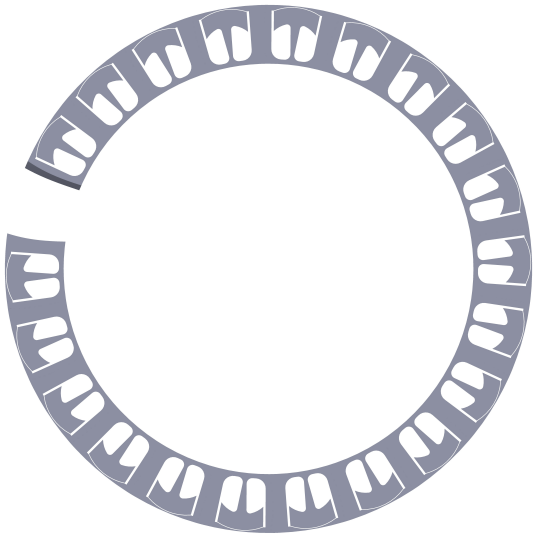

Figure 7.7: Damper with large mistuning caused by the absence of a sector

nonlinear results transition between one curve (e.g. the *stuck* response) to the other (e.g. the *free* response). This transition can be observed in the magnified response region of Fig. 7.8 as a function of the microslip parameter ρ. The maximum amplitude reduction that can be observed is 24.4% and 32.7% with respect to the *free* and *stuck* cases, respectively. The presence of mistuning is caused by the absence of an entire damper sector, as the damper used in the simulation is the one shown in Fig. 7.7. It can also be noticed that even for small values of the microslip parameter ρ, which are obtained with small preload, the nonlinear results do not trace the *free* curve. This is due to the imperfect contact kinematics, as the damper head increasingly engages the contact when its vibration amplitude is large, which is true when a low preload is present. For the preload to be kept constant across a range of oscillator vibration amplitudes, the relative motion of the contact surfaces should be always tangential to themselves. In fact, due to the presence of a normal contact stiffness at the contact, a relative motion orthogonal to the contact surface would increase, or decrease, the preload. Let us consider the oscillator first bending mode, which is the one used in this study to target the blisk mode, shown in Fig. 7.5 for $ND = 2$. As the beam deflects, the oscillator contact surface moves relative to its casing. It is possible to notice from Fig. 7.3

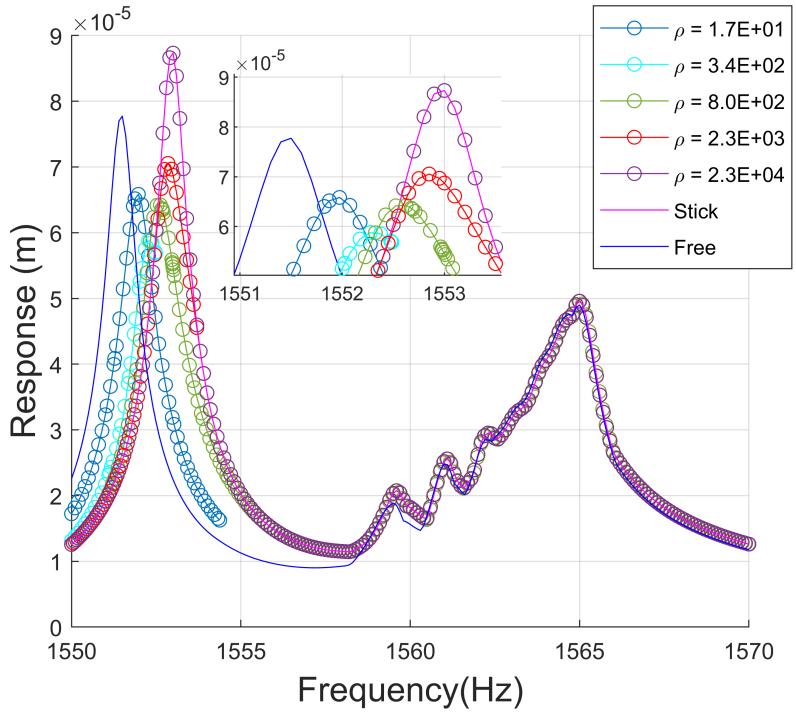

Figure 7.8: Blisk forced response for different values of the microslip parameter ρ using the mistuned damper shown in Fig. 7.7

that the contacting surfaces were designed with a hemicylindrical shape, the center of the cylinder being located at the base of the supporting beam, to minimize the motion in the direction orthogonal to the contact. However, as it can be noted from the magnified view presented in Fig. 7.5, the oscillator motion still presents a component orthogonal to the contact surface in the areas closer to the corners. Since in the simulation there is no gap between the contact interfaces, this motion creates an increase in contact pressure between the two contact interfaces, especially in the corner areas, to avoid penetration. Therefore, the nonlinear results in the presence of frictional contact will never trace the *free* curve, in which there is no constraint on the relative motion of the two surfaces, when no gap is present. This phenomenon, however, is potentially beneficial, because even for low levels of preload it is possible to observe energy dissipation and damper effectiveness, which would not be possible with a traditional damper.

Damper effectiveness is evaluated by comparing the maximum vibration amplitude across all blades over the frequency range studied. Since the microslip parameter ρ is a function of the forcing amplitude F, the normalized amplitude is used, i.e. $|\mathbf{x}|/F$. The variation of damper effectiveness as a function of the microslip parameter ρ is shown in Fig. 7.9. Please note that the vibration amplitudes obtained for linear cases are reported as horizontal lines because they do not depend on the microslip parameter ρ. It is interesting to notice that the *free* case typically shows a smaller vibration amplitude compared to the *stuck* case. This is because in *free* conditions the tuned oscillators act as a tuned vibration absorber and thus absorb some of the energy. It is possible to notice that the curves exhibit a V-shaped valley, where the depth indicates the effectiveness magnitude, and the width indicates the range of effectiveness. It is desirable for the damper effectiveness curve shown in Fig. 7.9 to be both deep and wide, which would indicate large vibration reduction and robustness to ρ variations. Variations in ρ can be due to changes in the preload, for example.

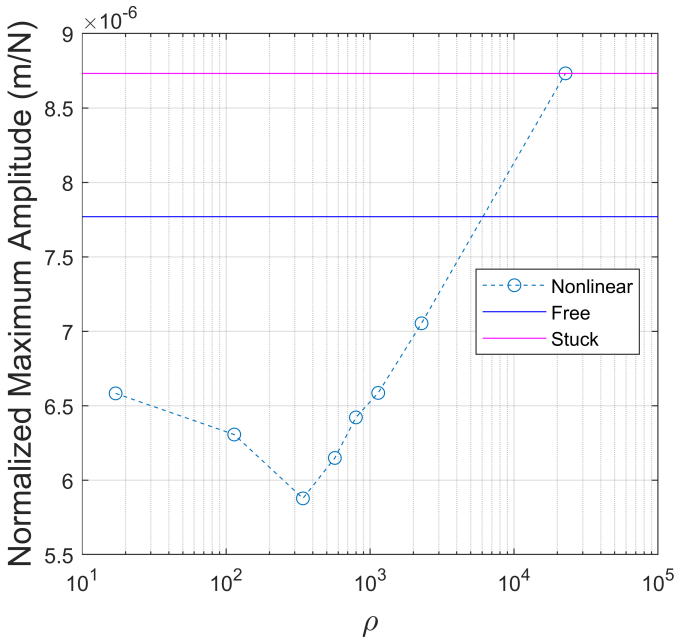

Figure 7.9: Normalized blade maximum response from the results presented in Fig. 7.8 as a function of the microslip parameter ρ

To better understand the contact behavior, the vibration amplitude envelope of the oscillators contact interface is plotted in Fig. 7.10. The *free* and *stuck* curves are plotted as references. It is possible to notice that there is a significant difference between the *free* and *stuck* cases for the oscillators, the former being almost two orders of magnitude larger than the latter. The *free* case presents an amplitude comparable to the one observed in the blade response in Fig. 7.8. For convenience, the *stuck* and nonlinear responses are magnified in Fig. 7.10. The envelope of the nonlinear response, shown for different values of the microslip parameter ρ, is very close to the *stuck* case, and does not trace the *free* curve even for very low values of ρ, in this case obtained for low values of the preload. This confirms the fact that due to the geometry of the contact surface and the contact kinematics, the damper oscillator cannot achieve large motion in the absence of a gap between the two surfaces.

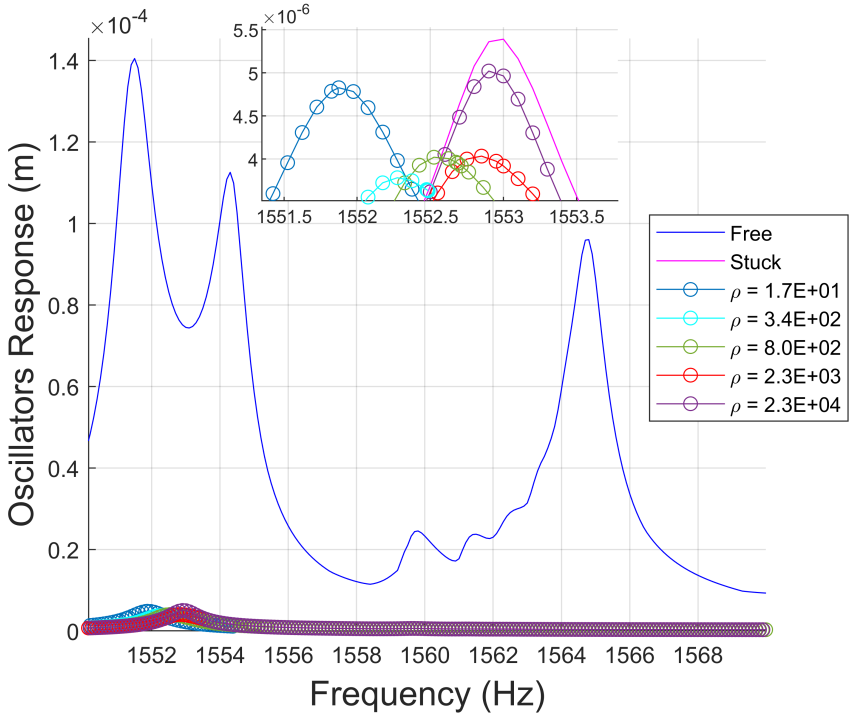

Figure 7.10: Oscillators forced response for different values of the microslip parameter ρ for the mistuned damper shown in Fig. 7.7

7.3.2 Effects of blisk damping on damper effectiveness

In this section, the effect of linear damping of the blisk on the overall effectiveness is presented. The forced response results are calculated for two different values of the damping ratio, namely $\zeta = 10^{-5}$ and $\zeta = 10^{-6}$. These two values were used to simulate the extremely low values of damping which could occur, for example, in the presence of negative aerodynamic damping. The forced response results are presented in Fig. 7.11. The amplitude achieved in the linear case for $\zeta = 10^{-6}$, presented with a dashed line, shows a different order of magnitude compared to the nonlinear cases. The nonlinear results are presented as a function of ρ and ζ. It is possible to notice that the results for $\zeta = 10^{-6}$, marked with a circle, almost match the ones obtained for $\zeta = 10^{-5}$, marked with a star. This can be observed for all ρ values examined. This is due to the fact that the energy dissipated via friction is much larger than the one dissipated by viscous damping. Once the value of ζ is low enough, it does not have much effect on the vibration amplitude when the damper is operating in a high effectiveness range. The damping due to the damper can be estimated through the use of an equivalent linear damping ζ_{eq} that gives a similar vibration amplitude. In this case, $\zeta_{eq} = 8.5 \cdot 10^{-5}$ qualitatively match the amplitude obtained with the damper, as it can be seen by observing the solid lines in Fig. 7.11.

7.3.3 Effects of damper mistuning

In this section, the case in which large damper mistuning is not present is analyzed. The results shown in Figs. 7.8-7.12 are obtained for the case of a damper with a whole sector missing, as shown in Fig. 7.7. In order to show the mistuning caused by the missing sector for that case, all the blade amplitudes are shown in Fig. 7.12. For the sake of clarity, only the linear results are reported. Both in the *stuck* and the *free* cases, mistuning is clearly present, and blades in different sectors show very different amplitudes.

In contrast to the results in Figs. 7.8-7.12, the results discussed in this section are obtained

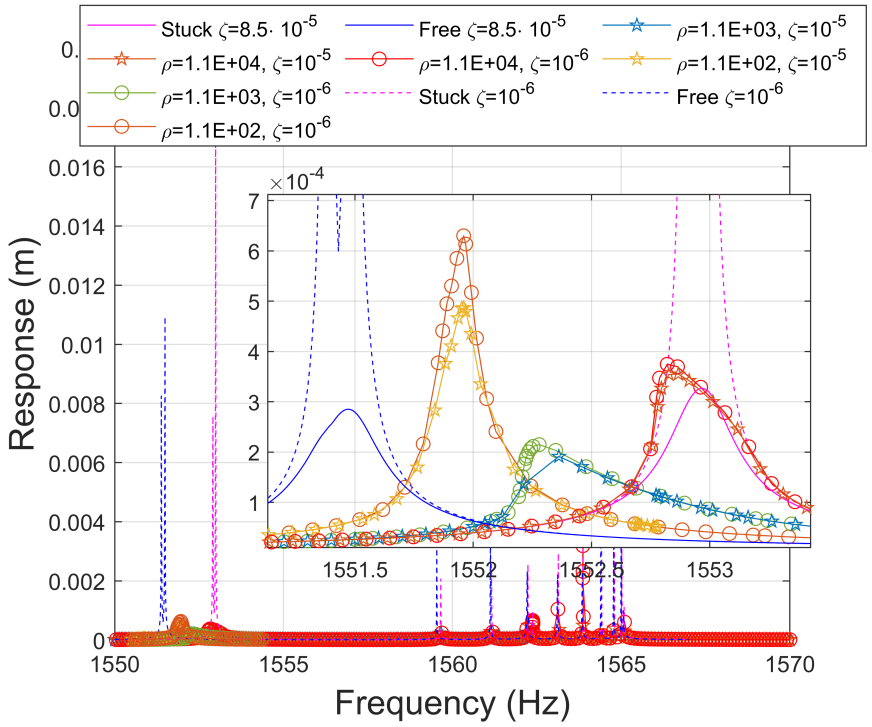

Figure 7.11: Blisk forced response as a function of the the microslip parameter ρ for $\zeta = 10^{-5}$ and $\zeta = 10^{-6}$ using the mistuned damper shown in Fig. 7.7

with a full ring damper, shown in Fig. 7.13. The blisk response obtained with a full ring damper that has no cut, and thus does not introduce mistuning, is presented in Fig. 7.14. It is possible to notice that even in this case the overall effectiveness is preserved. However, the maximum observed amplitude reduction is lower compared to the case involving the damper with a missing sector presented in Fig.7.7. With the full ring damper, we observed a 16.6% and 21.1% reduction compared to the *free* and *stuck* curves, respectively. It is also important to notice that the baseline linear response of Fig. 7.14 is lower in amplitude compared to the one of Fig. 7.8. This is due to the fact that a full ring damper does not introduce large mistuning, as it can also be seen from the results in the frequency range 1558 Hz – 1568 Hz, which do not show any peaks when the full ring damper is used.

The effectiveness curve, obtained by plotting the maximum normalized blade amplitude across the frequency range as a function of the microslip parameter ρ, is shown in Fig. 7.15.

Even in this case it can be noticed that the *free* case shows a smaller vibration amplitude compared to the *stuck* case. The nonlinear results trace a V-shaped curve, and the amplitude reduction obtained is evident.

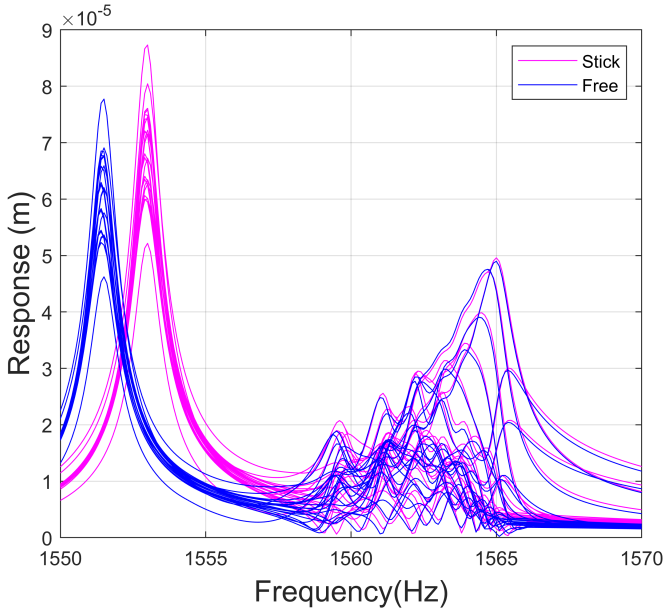

Figure 7.12: Forced response results (linear) showing the presence of mistuning using the damper shown in Fig. 7.7

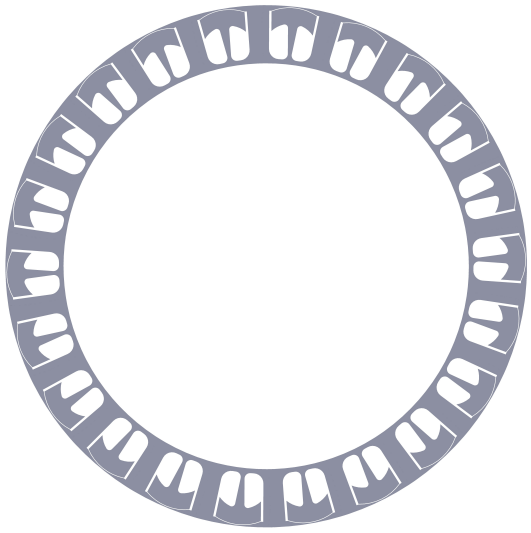

Figure 7.13: Proposed damper without cut

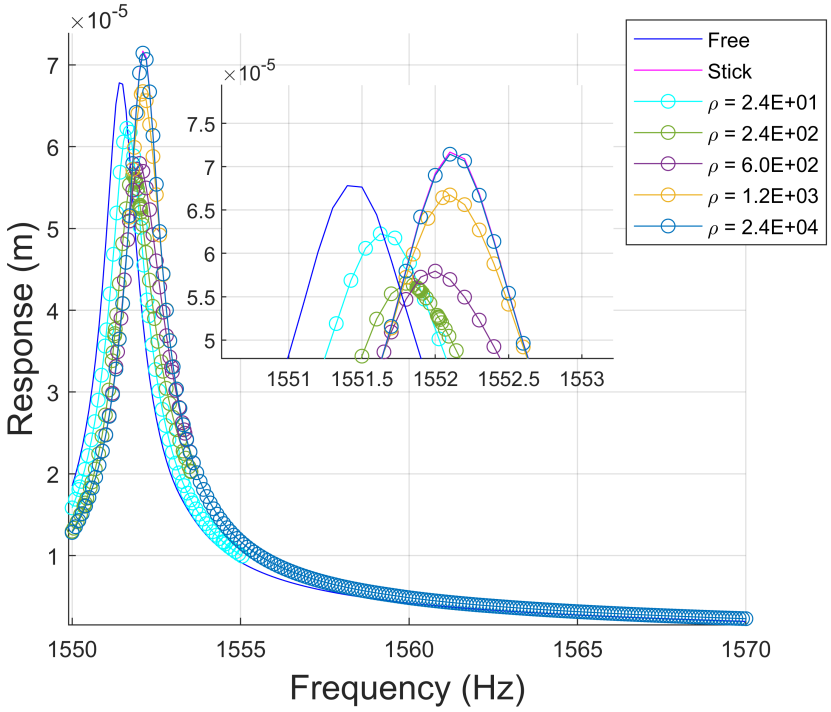

Figure 7.14: Forced response results obtained using the full ring damper shown in Fig. 7.13

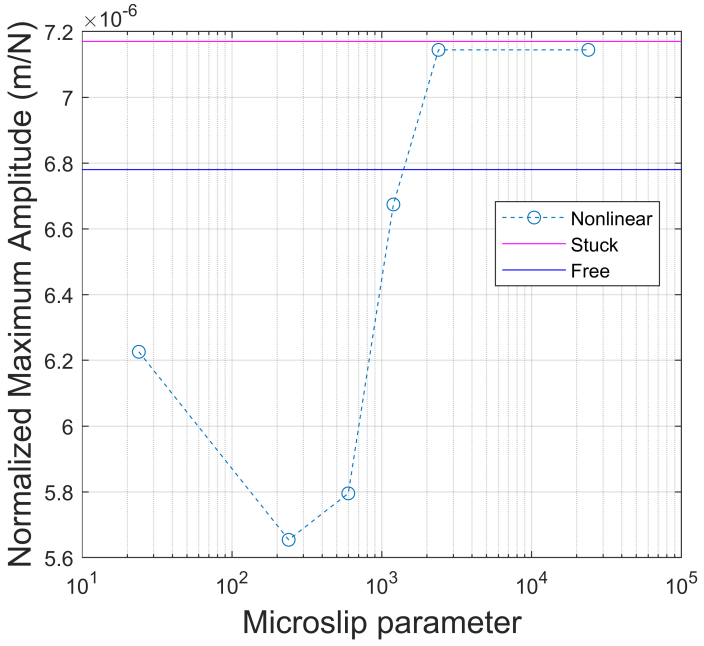

Figure 7.15: Normalized blade maximum response as a function of the microslip parameter ρ for the full ring damper shown in Fig. 7.13

7.4 Structural durability considerations

In this chapter, the focus was set on the vibration reduction offered by the proposed design. However, when designing a system that undergoes a large number of vibration cycles, its structural durability should also be taken into account. In fact, the high alternating stresses could cause the inception and propagation of a crack, that could ultimately lead to the failure of the oscillator. In this section, the areas of potential concerns are highlighted by calculating the fatigue life of a single oscillator subject to repeated 1st bending modal displacement. The shape of the modal displacement scaled by a factor of 10^{-3} is shown in Fig. 7.16. The large amplitude is chosen to better illustrate the expected motion. The fatigue life calculation was carried out using a scaling factor of the modal displacement equal to $5 \cdot 10^{-5}$, i.e. with a motion 20 times smaller than the one shown in Fig. 7.16. The fatigue life achieved considering a high yield strength steel is presented in Fig. 7.17. It can be noticed that the predicted life in the areas highlighted in red is lower than 5000 cycles, which means that future design iterations should aim at reducing the magnitude of alternating stresses to ensure reliability of the component.

Figure 7.16: Modal displacement used for the calculation of fatigue life (10^{-3} scaling factor)

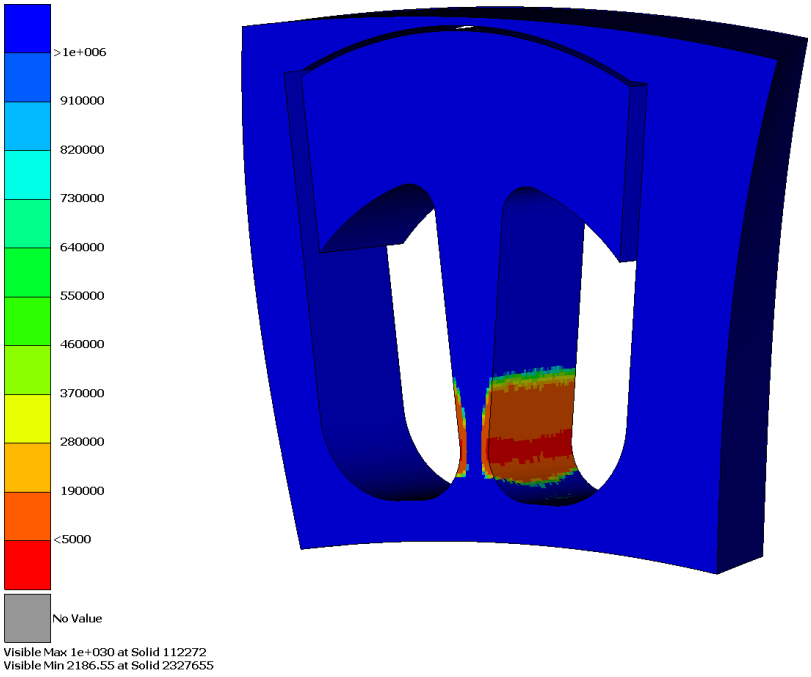

Figure 7.17: Fatigue life in number of cycles obtained using a $5 \cdot 10^{-5}$ scaling factor

7.5 Conclusions

In this study, a novel design for a tuned ring damper was proposed and analyzed using a high fidelity FE model based on the geometry of NASA Rotor 67. The results showed good effectiveness across a range of parameters, and the best amplitude reduction was observed in the presence of large geometric mistuning in the damper, caused by the absence of one of its sectors. Furthermore, the damper presented good effectiveness even if the tuning was not perfect, i.e. the damper and blisk frequencies were not exactly the same. This is a further proof of the fact that this design is robust to small frequency variations. The analysis presented in this study involved the use of a damper having the same number of sectors as the host blisk structure. Future work could be carried out on the quantitative analysis of the relationship between number of damper sectors and amplitude reduction, to establish the most suitable number of sectors to be used. The analysis was carried out at different values of

linear damping, showing that the effectiveness of the damper significantly increase for lower values of blisk damping ζ, becoming independent of ζ once the energy dissipated through nonlinearities becomes significantly larger than the one dissipated via viscous damping. It is also important to note that the damper proposed is not limited to working through frictional dissipation. It could be coupled, for example, with impact damping, or damping coatings, to dissipate the energy that has been transferred to the damper via tuning.

CHAPTER 8

Conclusion

A summary of the contributions of this work is presented in this chapter, along with their relevance. The final section is devoted to discussing the limitations of the presented results as well as future work.

8.1 Summary of contributions

Due to the nature of the work presented in this thesis, the contributions of this thesis to the field of turbomachinery can be conveniently split in two parts. The first part is about modeling, and in particular about reduced-order-modeling, and the other one about novel damping mechanisms. The main contributions to the field of turbomachinery ROMs can be summarized as follows:

- An inexpensive and flexible conditioning technique for projection-based ROMs [112].
- A computationally efficient method to accommodate mesh morphing in ROMs [114].
- A technique for quick calculation of prestress effects to be included in existing ROMs where geometric mistuning interacts with prestress [134].
- A comprehensive tool (MAX+) for the analysis of blended blisks in which the previous methods are integrated [112, 114, 134].

The contributions to the field of vibration damping mechanisms for IBRs are instead the following:

- Development and validation of a damper concept based on ring damper design and TVA concept [130].
- Experimental and computational validation of the proposed damping mechanism [131].
- Design and computational validation of a feasible design for the novel ring damper concept [135].

The detailed chapter by chapter contributions are presented below.

8.1.1 Conditioning technique for ROMs

In Chapter 2, a *post-conditioning* approach to condition projection-based reduced order models was developed. The conditioning multiplications lead to a particularly simple form of the ROM, in which the conditioned mass matrix is already diagonal, further simplifying the calculations. Both the method and the error metrics have been tested and validated using a chain of oscillators as well as ROM for a bladed disk (blisk) model. The proposed method presents a number of advantages:

1. The method directly acts in the ROM space, and so there is no need to condition a priori the projection matrix, resulting in faster calculations.
2. No explicit knowledge of the transformation matrix is required. Thus, the method can be easily applied to already existing models by adding a simple *post-conditioning* step.
3. The method can be applied to a variety of ROMs, built using any arbitrary choice of reduced order bases. Most structural dynamical systems may be treated using this approach.

4. The method preserves the physical meaning of the transformation matrix, and the meaning of the equations of motion also. This feature allows for simplifications in the ROM creation when specific types of vectors are used (e.g., normal modes).

The findings have been published in [112].

8.1.2 Integration of mesh morphing and prestress effects in ROMs

In Chapters 3-4, two methods were introduced to improve ROM efficiency and accuracy in the field of ROMs for geometrically mistuned blisks. First, a novel method able to account for the presence of multiple meshes within reduced order models for cyclic structures was presented. The formulation is simple and cost effective, without sacrificing accuracy. The method was applied to the case of an academic blisk for validation, and it outperformed the methods that are currently available. The results highlighted that the accuracy of the method presented here is superior to the one offered by previous alignment/clocking approaches. In addition, numerical issues associated with the ROM creation due to the presence of multiple meshes were solved by means of a simple correction of the ROM matrices.

Then, a comprehensive method for the study of blended blisks, MAX+, was introduced. This method extends the capabilities of MAX [10] and allows the introduction of prestress, finite element mesh morphing, and other system characteristics in a general framework for the analysis of IBR bends. One of the enabling techniques is a method to build ROMs using only sector level matrices of quasi-cyclic structures subject to prestress. The approximation introduced in MAX+ causes little to no accuracy loss. The computational gains are significant, given that full wheel calculations are cumbersome for large finite element models. The MAX+ method can be applied in the design process to identify optimal repair strategies. Results can be obtained quickly for different conditions, without requiring repetitive new finite element studies. The ability to accommodate the use of mesh morphing is also of paramount importance, enabling rapid creation of multiple complex geometries.

These findings have been published in [114, 134].

8.1.3 Novel damping mechanisms for blisks

Chapters 5-7 are entirely dedicated to the study and creation of novel damping devices to be used to mitigate excessive vibration in blisks.

As a starting point, a novel ring damper concept able to effectively damp vibration in blisks was proposed based on the tuned vibration absorber idea. The effectiveness of the proposed design was studied by calculating the forced response of the system. Linear and nonlinear results were obtained to compare the effectiveness of the proposed tuned vibration absorber to a traditional non-tuned ring damper. A significant amplitude reduction was achieved using the proposed concept. This reduction was made possible by enabling frictional nonlinearities to dissipate energy by means of increased damper motion. The robustness of the approach was assessed by evaluating the response in case of an improperly tuned damper. Damper effectiveness showed a decrease compared to the case of perfect tuning. However, greater effectiveness was observed compared to the non-tuned case. This preliminary study demonstrated the effectiveness of a novel damper concept using a traditional damper geometry.

Then, an experimental and numerical study was presented to assess the effectiveness of a tuned mass damper with frictional contacts for damping blade-like structures. The experimental results obtained demonstrate that such a tuned mass damper concept could be used to effectively lower the vibration of a lightly damped structure even if the attachment location shows little motion. Simulation results showed good qualitative agreement with experimental results, validating the simulation models and techniques used.

Finally, a novel design for a tuned ring damper was proposed and analyzed using a high fidelity FE model based on the geometry of NASA Rotor 67. The results showed good effectiveness across a large range of parameters, and the best amplitude reduction was

observed in the presence of large geometric mistuning in the damper, caused by the absence of one of its sectors. Furthermore, the damper presented good effectiveness even if the tuning was not perfect, i.e. the damper and blisk frequencies were not exactly the same. This is a further proof of the fact that this design is robust to small frequency variations. The analysis was carried out at different values of linear damping, showing that the effectiveness of the damper significantly increase for lower values of blisk damping ζ, becoming independent of ζ once the energy dissipated through nonlinearities becomes significantly larger than the one dissipated via viscous damping. It is also important to note that the damper proposed is not limited to working through frictional dissipation. It could be coupled, for example, with impact damping, or damping coatings, to dissipate the energy that has been transferred to the damper via tuning.

The findings presented in this section have been published in [73, 130, 131, 135].

8.2 Future work

The work presented in this thesis could be further extended in the future to answer some of the questions that arose during the research process.

The conditioning technique introduced in Chapter 2 was only tested on ROMs for structural dynamics. However, its formulation is so general and broad that in the future it could be applied to completely different systems. In fact, even though the formulation presented targeted Galerkin ROMs, this conditioning idea can be extended to the general case in which Petrov-Galerkin projection is used. Further work can also be done to extend this formulation to the more general case of nonlinear dynamical systems.

The mesh morphing method presented in Chapter 3 could be used to reduce the computational cost in the calculation of mistuned normal modes also. In fact, when small geometric mistuning is present, the forced response could appropriately capture the mistuned modes,

further reducing the computational time and cost. The MAX+ method, from Chapter 4, could be directly compared against other ROMs to quantify the gains introduced by the simplified prestress calculations as well as treatment of mesh morphing. The method could be implemented in an toolbox for the optimization of blend shape and location to better inform designers in the repair and maintenance phase.

The effectiveness of the proposed ring damper mechanism was demonstrated using a single example in Chapter 5. Future work could be carried out on the exploration of different damper geometries capable of further increasing the effectiveness of such dampers. The response at different engine orders and for different mode families could be analyzed, as well as the interaction between the damper modes and the blisk modes.

The experiment introduced in Chapter 6 could be further improved by measuring the normal load F_0 present at the contact in the experiment, with the aim of introducing a quantitative comparison between simulation and experimental results. A study on the effect of damper positioning on its effectiveness could also be carried out, to identify the minimum vibration amplitude at the attachment location that is required to obtain a significant amplitude reduction. Furthermore, more complex modes, as well as higher frequencies could be targeted to explore the range of effectiveness of the proposed damper. These studies will help clarify the direct applicability of this damper concept to blisks and other lightly damped structures in which dampers are constrained to be situated in regions of low motion.

Finally, the damper design presented in Chapter 7, which was analyzed only in terms of vibration reduction offered, should be studied in depth both in terms of structural durability and machining. The complex contact surface geometry could be optimized to achieve the optimal contact condition, potentially further improving damper effectiveness. Future work could also be carried out on the quantitative analysis of the relationship between number of damper sectors and amplitude reduction, to establish the most suitable number of sectors to be used.

BIBLIOGRAPHY

[1] James Min, Donald Harris, and Joseph Ting. Advances in ceramic matrix composite blade damping characteristics for aerospace turbomachinery applications. In *52nd AIAA/ASME/ASCE/AHS/ASC Structures, Structural Dynamics and Materials Conference 19th AIAA/ASME/AHS Adaptive Structures Conference 13t*, page 1784, 2011.

[2] D. L. Thomas. Dynamics of rotationally periodic structures. *International Journal for Numerical Methods in Engineering*, 14(1):81–102, 1979.

[3] Mainak Mitra and Bogdan I Epureanu. Dynamic modeling and projection-based reduction methods for bladed disks with nonlinear frictional and intermittent contact interfaces. *Applied Mechanics Reviews*, 2019.

[4] M.P. Castanier and C. Pierre. Modeling and analysis of mistuned bladed disk vibration: Current status and emerging directions. *Journal of Propulsion and Power*, 22(2):384–396, 2006.

[5] Christophe Pierre, Todd E Smith, and Durbha V Murthy. Localization of aeroelastic modes in mistuned high-energy turbines. *Journal of Propulsion and Power*, 10(3):318–328, 1994.

[6] D. S. Whitehead. The maximum factor by which forced vibration of blades can increase due to mistuning. *Journal of Engineering for Gas Turbines and Power-Transactions of the ASME*, 120(1):115–119, 1998.

[7] Matthias Hüls, Lars Panning-von Scheidt, and Jörg Wallaschek. Influence of geometric design parameters onto vibratory response and high-cycle fatigue safety for turbine blades with friction damper. *Journal of Engineering for Gas Turbines and Power*, 141(4):041022, 2019.

[8] Sang-Ho Lim, Matthew Castanier, and Christophe Pierre. Vibration modeling of bladed disks subject to geometric mistuning and design changes. In *45th AIAA/ASME/ASCE/AHS/ASC Structures, Structural Dynamics & Materials Conference*, page 1686, 2004.

[9] Seunghun Baek and B. I. Epureanu. Reduced-order models of blisks with small geometric mistuning. *Journal of Vibration and Acoustics*, 139(4):041003–041003–10, 2017.

[10] Y. Q. Gan, J. L. Mayer, K. X. D'Souza, and B. I. Epureanu. A mode-accelerated xxr (max) method for complex structures with large blends. *Mechanical Systems and Signal Processing*, 93:1–15, 2017.

[11] A. Madden, B. I. Epureanu, and S. Filippi. Reduced-order modeling approach for blisks with large mass, stiffness, and geometric mistuning. *AIAA Journal*, 50(2):366–374, 2012.

[12] Moustapha Mbaye, Christian Soize, and Jean-Philippe Ousty. A Reduced-Order Model of Detuned Cyclic Dynamical Systems With Geometric Modifications Using a Basis of Cyclic Modes. *Journal of Engineering for Gas Turbines and Power*, 132(11):112502–112502–9, August 2010.

[13] W. Tang, B. I. Epureanu, and S. Filippi. Models for blisks with large blends and small mistuning. *Mechanical Systems and Signal Processing*, 87:161–179, 3 2017.

[14] G. Kerschen, J. C. Golinval, A. F. Vakakis, and L. A. Bergman. The method of

proper orthogonal decomposition for dynamical characterization and order reduction of mechanical systems: An overview. *Nonlinear Dynamics*, 41(1-3):147–169, 2005.

[15] B. Besselink, U. Tabak, A. Lutowska, N. van de Wouw, H. Nijmeijer, D.J. Rixen, M.E. Hochstenbach, and W.H.A. Schilders. A comparison of model reduction techniques from structural dynamics, numerical mathematics and systems and control. *Journal of Sound and Vibration*, 332(19):4403 – 4422, 2013.

[16] Clarence W Rowley. Model reduction for fluids, using balanced proper orthogonal decomposition. *International Journal of Bifurcation and Chaos*, 15(03):997–1013, 2005.

[17] Zhaojun Bai. Krylov subspace techniques for reduced-order modeling of large-scale dynamical systems. *Applied Numerical Mathematics*, 43(1):9 – 44, 2002.

[18] D de Klerk, Daniel J Rixen, and SN Voormeeren. General framework for dynamic substructuring: history, review and classification of techniques. *AIAA journal*, 46(5):1169–1181, 2008.

[19] Irina Kalashnikova, Matthew F. Barone, Srinivasan Arunajatesan, and Bart G. van Bloemen Waanders. Construction of energy-stable projection-based reduced order models. *Applied Mathematics and Computation*, 249:569 – 596, 2014.

[20] Peter Benner, Serkan Gugercin, and Karen Willcox. A survey of projection-based model reduction methods for parametric dynamical systems. *SIAM review*, 57(4):483–531, 2015.

[21] Irina Kalashnikova, Bart van Bloemen Waanders, Srinivasan Arunajatesan, and Matthew Barone. Stabilization of projection-based reduced order models for linear time-invariant systems via optimization-based eigenvalue reassignment. *Computer Methods in Applied Mechanics and Engineering*, 272:251 – 270, 2014.

[22] David Amsallem and Charbel Farhat. Stabilization of projection-based reduced-order models. *International Journal for Numerical Methods in Engineering*, 91(4):358–377, 2012.

[23] Bradley N. Bond and Luca Daniel. Guaranteed stable projection-based model reduction for indefinite and unstable linear systems. In *Proceedings of the 2008 IEEE/ACM International Conference on Computer-Aided Design*, ICCAD '08, pages 728–735, Piscataway, NJ, USA, 2008. IEEE Press.

[24] Sung-Kwon Hong, Bogdan I Epureanu, Matthew P Castanier, and David J Gorsich. Parametric reduced-order models for predicting the vibration response of complex structures with component damage and uncertainties. *Journal of sound and vibration*, 330(6):1091–1110, 2011.

[25] S. K. Hong, B. I. Epureanu, and M. P. Castanier. Next-generation parametric reduced-order models. *Mechanical Systems and Signal Processing*, 37(1-2):403–421, 2013.

[26] M. Mitra, S. Zucca, and B. I. Epureanu. Adaptive microslip projection for reduction of frictional and contact nonlinearities in shrouded blisks. *Journal of Computational and Nonlinear Dynamics*, 11(4), 7 2016.

[27] Stijn Donders, Bert Pluymers, Patrik Ragnarsson, Rabah Hadjit, and Wim Desmet. The wave-based substructuring approach for the efficient description of interface dynamics in substructuring. *Journal of Sound and Vibration*, 329(8):1062–1080, 2010.

[28] Matthew Brand. Fast low-rank modifications of the thin singular value decomposition. *Linear algebra and its applications*, 415(1):20–30, 2006.

[29] Benjamin Peherstorfer and Karen Willcox. Dynamic data-driven reduced-order models. *Computer Methods in Applied Mechanics and Engineering*, 291:21–41, 2015.

[30] S. H. Lim, R. Bladh, M. P. Castanier, and C. Pierre. Compact, generalized component mode mistuning representation for modeling bladed disk vibration. *AIAA Journal*, 45(9):2285–2298, 2007.

[31] Alexander A Kaszynski, Joseph A Beck, and Jeffrey M Brown. Automated finite element model mesh updating scheme applicable to mistuning analysis. In *ASME Turbo Expo 2014: Turbine Technical Conference and Exposition*, pages V07BT33A025–V07BT33A025. American Society of Mechanical Engineers, 2014.

[32] Thomas Maywald, Thomas Backhaus, Sven Schrape, and Arnold Kühhorn. Geometric model update of blisks and its experimental validation for a wide frequency range. In *ASME Turbo Expo 2017: Turbomachinery Technical Conference and Exposition*, pages V07AT30A001–V07AT30A001. American Society of Mechanical Engineers, 2017.

[33] P Jafarali, Dmitry Krikunov, Amir Mujezinović, and Nicholas A Tisenchek. Probabilistic analysis of turbine blade tolerancing and tip shroud gap. In *ASME Turbo Expo 2012: Turbine Technical Conference and Exposition*, pages 469–476. American Society of Mechanical Engineers, 2012.

[34] Luigi Carassale, Silvia Bruzzone, Andrea Cavicchi, and Michela Marrè Brunenghi. Representation and analysis of geometric uncertainties in rotor blades. In *ASME Turbo Expo 2018: Turbomachinery Technical Conference and Exposition*, pages V07CT35A025–V07CT35A025. American Society of Mechanical Engineers, 2018.

[35] M Nikolic, EP Petrov, and DJ Ewins. Coriolis forces in forced response analysis of mistuned bladed disks. *Journal of turbomachinery*, 129(4):730–739, 2007.

[36] P Marugabandhu and JH Griffin. A reduced-order model for evaluating the effect of rotational speed on the natural frequencies and mode shapes of blades. *Journal of turbomachinery*, 125(3):772–776, 2003.

[37] Arnaud Sternchüss. *Multi-level parametric reduced models of rotating bladed disk assemblies*. PhD thesis, Ecole Centrale Paris, 2009.

[38] Zhijiang He, Bogdan I Epureanu, and Christophe Pierre. Fluid-structural coupling effects on the dynamics of mistuned bladed disks. *AIAA journal*, 45(3):552–561, 2007.

[39] Nicolas Guérin, Anders Thorin, Fabrice Thouverez, Mathias Legrand, and Patricio Almeida. Thermomechanical model reduction for efficient simulations of rotor-stator contact interaction. In *ASME Turbo Expo 2018: Turbomachinery Technical Conference and Exposition*, Oslo, Norway, June 2018. American Society of Mechanical Engineers.

[40] Eric Chatelet, Flavio DAmbrosio, and Georges Jacquet-Richardet. Toward global modelling approaches for dynamic analyses of rotating assemblies of turbomachines. *Journal of Sound and Vibration*, 282(1):163 – 178, 2005.

[41] G. Jacquet-Richardet, G. Ferraris, and P. Rieutord. Frequencies and modes of rotating flexible bladed disc-shaft assemblies: A global cyclic symmetry approach. *Journal of Sound and Vibration*, 191(5):901 – 915, 1996.

[42] R. R. Craig and M. C. C. Bampton. Coupling of substructures for dynamic analyses. *AIAA Journal*, 6(7):1313–1319, 1968.

[43] Arnaud Sternchüss and Etienne Balmes. On the reduction of quasi-cyclic disk models with variable rotation speeds. In *Proceedings of the International Conference on Advanced Acoustics and Vibration Engineering (ISMA)*, page 39253939, 2006.

[44] J.H. Kuang and B.W. Huang. The effect of blade crack on mode localization in rotating bladed disks. *Journal of Sound and Vibration*, 227(1):85 – 103, 1999.

[45] B.W. Huang and J.H. Kuang. Mode localization in a rotating mistuned turbo disk

with coriolis effect. *International Journal of Mechanical Sciences*, 43(7):1643 – 1660, 2001.

[46] Ferhat Kaptan, Lars Panning-von Scheidt, and Jörg Wallaschek. The vibrational behavior of coupled bladed disks with variable rotational speed. *PAMM*, 15(1):255–256, 2015.

[47] Sung-Kwon Hong, Bogdan I. Epureanu, and Matthew P. Castanier. Parametric reduced-order models of battery pack vibration including structural variation and prestress effects. *Journal of Power Sources*, 261:101 – 111, 2014.

[48] S. Patsias, C. Saxton, and M. Shipton. Hard damping coatings: an experimental procedure for extraction of damping characteristics and modulus of elasticity. *Materials Science and Engineering: A*, 370(1):412–416, 2004.

[49] KR Cross, WR Lull, RL Newman, and andJ R Cavanagh. Potential of graded coatings in vibration damping. *Journal of Aircraft*, 10(11):689–691, 1973.

[50] Brian J Olson, Steve W Shaw, and Christophe Pierre. Order-tuned vibration absorbers for cyclic rotating flexible structures. In *ASME 2005 International Design Engineering Technical Conferences and Computers and Information in Engineering Conference*, pages 2475–2484. American Society of Mechanical Engineers, 2005.

[51] A. Hartung, U. Retze, and H. Hackenberg. Impulse mistuning of blades and vanes. *J. Eng. Gas Turbines Power*, 139(7), 2017.

[52] D. J. Ewins. Control of vibration and resonance in aero engines and rotating machinery - An overview. *International Journal of Pressure Vessels and Piping*, 87(9):504–510, 2010.

[53] B. D. Yang and C. H. Menq. Characterization of contact kinematics and application to the design of wedge dampers in turbomachinery blading: Part 1 - Stick-slip contact kinematics. *Journal of Engineering for Gas Turbines and Power-Transactions of the ASME*, 120(2):410–417, 1998.

[54] B. D. Yang and C. H. Menq. Characterization of contact kinematics and application to the design of wedge dampers in turbomachinery blading: Part 2 - Prediction of forced response and experimental verification. *Journal of Engineering for Gas Turbines and Power-Transactions of the ASME*, 120(2):418–423, 1998.

[55] C. M. Firrone, S. Zucca, and M. M. Gola. The effect of underplatform dampers on the forced response of bladed disks by a coupled static/dynamic harmonic balance method. *International Journal of Non-Linear Mechanics*, 46(2):363–375, 2011.

[56] D. Laxalde, F. Thouverez, J.J. Sinou, and J.P. Lombard. Qualitative analysis of forced response of blisks with friction ring dampers. *European Journal of Mechanics - A/Solids*, 26(4):676–687, 2007.

[57] D. Laxalde and F. Thouverez. Non-linear vibrations of multi-stage bladed disks systems with friction ring dampers. *Proceedings of the Asme International Design Engineering Technical Conferences and Computers and Information in Engineering Conference 2007, Vol 5, Pts a-C,*, pages 3–10, 2008.

[58] Mainak Mitra, Stefano Zucca, and Bogdan I Epureanu. Effects of contact mistuning on shrouded blisk dynamics. In *ASME Turbo Expo 2016: Turbomachinery Technical Conference and Exposition*. American Society of Mechanical Engineers Digital Collection.

[59] W. H. Tang and B. I. Epureanu. Nonlinear dynamics of mistuned bladed disks with ring dampers. *International Journal of Non-Linear Mechanics*, 97:30–40, 2017.

[60] W. Tang, S. Baek, and B. I. Epureanu. Reduced-order models for blisks with small and large mistuning and friction dampers. *Journal of Engineering for Gas Turbines and Power*, 139(1), 1 2017.

[61] Seunghun Baek and B. I. Epureanu. Reduced order modeling of bladed disks with friction ring dampers. *Journal of Vibration and Acoustics*, 2017.

[62] Denis Laxalde, Claude Gibert, and Fabrice Thouverez. Experimental and numerical investigations of friction rings damping of blisks. In *ASME Turbo Expo 2008: Power for Land, Sea, and Air*, pages 469–479. American Society of Mechanical Engineers, 2008.

[63] Denis Laxalde, Fabrice Thouverez, and Jean-Pierre Lombard. Forced response analysis of integrally bladed disks with friction ring dampers. *Journal of Vibration and Acoustics*, 132(1):011013, 2010.

[64] Weihan Tang and Bogdan I Epureanu. Geometric optimization of dry friction ring dampers. *International Journal of Non-Linear Mechanics*, 109:40–49, 2019.

[65] Yanrong Wang, Hang Ye, Xianghua Jiang, and Aimei Tian. A prediction method for the damping effect of ring dampers applied to thin-walled gears based on energy method. *Symmetry*, 10(12):677, 2018.

[66] C. M. Firrone and S. Zucca. Passive control of vibration of thin-walled gears: advanced modelling of ring dampers. *Nonlinear Dynamics*, 76(1):263–280, Apr 2014.

[67] Stefano Zucca, Christian Maria Firrone, and Marco Facchini. A method for the design of ring dampers for gears in aeronautical applications. *Journal of Mechanical Design*, 134(9):091003, 2012.

[68] Jacob Pieter Den Hartog. *Mechanical vibrations*. Courier Corporation, 1985.

[69] Said Elias and Vasant Matsagar. Research developments in vibration control of structures using passive tuned mass dampers. *Annual Reviews in Control*, 44:129 – 156, 2017.

[70] Mariantonieta Gutierrez Soto and Hojjat Adeli. Tuned mass dampers. *Archives of Computational Methods in Engineering*, 20(4):419–431, Dec 2013.

[71] T Igusa and K Xu. Vibration control using multiple tuned mass dampers. *Journal of sound and vibration*, 175(4):491–503, 1994.

[72] Mehmet Bulent Ozer and Thomas J Royston. Extending den hartogs vibration absorber technique to multi-degree-of-freedom systems. *Journal of Vibration and Acoustics*, 127(4):341–350, 2005.

[73] M. Mitra, A. Lupini, and B. I. Epureanu. A study on the application of tuned vibration absorbers to nominally cyclic structures. In *ASME Turbo Expo 2019: Turbine Technical Conference and Exposition*, pages GT2019–90167. ASME, 2019.

[74] Y. Q. Guo and W. Q. Chen. Dynamic analysis of space structures with multiple tuned mass dampers. *Engineering Structures*, 29(12):3390–3403, 2007. Cited By :57.

[75] Tuğrul Aksoy, Bülent Acar, and Gökhan O Özgen. A novel method for the vibration reduction of an air vehicle missile launcher. In *AIAA Scitech 2019 Forum*, page 0494, 2019.

[76] JQ Sun, M Re Jolly, and MA Norris. Passive, adaptive and active tuned vibration absorbersa survey. *Journal of mechanical design*, 117(B):234–242, 1995.

[77] Alka Y. Pisal and R. S. Jangid. Dynamic response of structure with tuned mass friction damper. *International Journal of Advanced Structural Engineering*, 8(4):363–377, Dec 2016.

[78] A Hartung, H Schmieg, and P Vielsack. Passive vibration absorber with dry friction. *Archive of applied mechanics*, 71(6-7):463–472, 2001.

[79] Kiran DSouza, Mike Dunn, and Bogdan I. Epureanu. Mistuning and Damping Experiments at Design Speed Combined With Computational Tools. volume 7B: Structures and Dynamics of *Turbo Expo: Power for Land, Sea, and Air*, 06 2017.

[80] J. M. Varah. On the numerical solution of ill-conditioned linear systems with applications to ill-posed problems. *SIAM Journal on Numerical Analysis*, 10(2):257–267, 1973.

[81] G Fix and R Heiberger. An algorithm for the ill-conditioned generalized eigenvalue problem. *SIAM Journal on Numerical Analysis*, 9(1):78–88, 1972.

[82] Gilbert W Stewart. On the sensitivity of the eigenvalue problem Ax=λ Bx. *SIAM Journal on Numerical Analysis*, 9(4):669–686, 1972.

[83] Randall J Allemang. The modal assurance criterion–twenty years of use and abuse. *Sound and vibration*, 37(8):14–23, 2003.

[84] Daniel Sieger, Sergius Gaulik, Jascha Achenbach, Stefan Menzel, and Mario Botsch. Constrained space deformation techniques for design optimization. *Computer-Aided Design*, 72:40–51, 2016.

[85] Daniel Sieger, Stefan Menzel, and Mario Botsch. On shape deformation techniques for simulation-based design optimization. In *New Challenges in Grid Generation and Adaptivity for Scientific Computing*, pages 281–303. Springer, 2015.

[86] Travis Carrigan, Mark Landon, and Claudio Pita. Meshing considerations for automotive shape design optimization. Technical report, SAE Technical Paper, 2016.

[87] Daniel Sieger, Stefan Menzel, and Mario Botsch. RBF morphing techniques for simulation-based design optimization. *Engineering with Computers*, 30(2):161–174, April 2014.

[88] Radhika Vurputoor, Nilanjan Mukherjee, Jean Cabello, and Michael J. Hancock. A Mesh Morphing Technique For Geometrically Dissimilar Tessellated Surfaces. In *Proceedings of the 16th International Meshing Roundtable, IMR 2007*, pages 315–334, January 2007.

[89] Matthew L. Staten, Steven J. Owen, Suzanne M. Shontz, Andrew G. Salinger, and Todd S. Coffey. A Comparison of Mesh Morphing Methods for 3d Shape Optimization. In *Proceedings of the 20th International Meshing Roundtable*, pages 293–311. Springer, Berlin, Heidelberg, 2011.

[90] F Salmoiraghi, F Ballarin, G Corsi, A Mola, M Tezzele, G Rozza, et al. Advances in geometrical parametrization and reduced order models and methods for computational fluid dynamics problems in applied sciences and engineering: overview and perspectives. In *ECCOMAS 2016, VII European Congress on Computational Methods in Applied Sciences and Engineering*, volume 1, pages 1013–1031, 2016.

[91] Filippo Salmoiraghi, Francesco Ballarin, Luca Heltai, and Gianluigi Rozza. Isogeometric analysis-based reduced order modelling for incompressible linear viscous flows in parametrized shapes. *Advanced Modeling and Simulation in Engineering Sciences*, 3(1):21, 2016.

[92] George Anderson, Michael Aftosmis, and Marian Nemec. Parametric deformation of discrete geometry for aerodynamic shape design. In *50th AIAA Aerospace Sciences Meeting including the New Horizons Forum and Aerospace Exposition*, page 965, 2012.

[93] Andrea Manzoni, Alfio Quarteroni, and Gianluigi Rozza. Shape optimization for viscous flows by reduced basis methods and free-form deformation. *International Journal for Numerical Methods in Fluids*, 70(5):646–670, 2012.

[94] Martyna Czarniewska, Grzegorz Fotyga, and Michał Mrozowski. Local mesh deformation for accelerated parametric studies based on the finite element method. In *2017 IEEE MTT-S International Conference on Numerical Electromagnetic and Multiphysics Modeling and Optimization for RF, Microwave, and Terahertz Applications (NEMO)*, pages 284–286. IEEE, 2017.

[95] Adam Lamecki. A mesh deformation technique based on solid mechanics for parametric analysis of high-frequency devices with 3-d fem. *IEEE Transactions on Microwave Theory and Techniques*, 64(11):3400–3408, 2016.

[96] Stefan Burgard, Ortwin Farle, and Romanus Dyczij-Edlinger. A novel parametric model order reduction approach with applications to geometrically parameterized microwave devices. *COMPEL: The International Journal for Computation and Mathematics in Electrical and Electronic Engineering*, 32(5):1525–1538, 2013.

[97] Wei Wang and Marinos N Vouvakis. Mesh morphing strategies for robust geometric parameter model reduction. In *Antennas and Propagation Society International Symposium (APSURSI), 2012 IEEE*, pages 1–2. IEEE, 2012.

[98] Stefano Porziani, Corrado Groth, and Marco Evangelos Biancolini. Automatic shape optimization of structural components with manufacturing constraints. *Procedia Structural Integrity*, 12:416–428, 2018.

[99] Maryam Asghari Mooneghi and Ramtin Kargarmoakhar. Aerodynamic mitigation and shape optimization of buildings. *Journal of building engineering*, 6:225–235, 2016.

[100] Wei Liu and Yuying Yang. Multi-objective optimization of an auto panel drawing die face design by mesh morphing. *Computer-Aided Design*, 39(10):863–869, October 2007.

[101] Herman Van der Auweraer, T Van Langenhove, M Brughmans, I Bosmans, Najy Masri, and Stijn Donders. Application of mesh morphing technology in the concept phase of vehicle development. *Int. J. of Vehicle Design*, 43:281–305, January 2007.

[102] Bogdan I Epureanu, Liaosha S Tang, and Michael P Paıdoussis. Coherent structures and their influence on the dynamics of aeroelastic panels. *International Journal of Non-Linear Mechanics*, 39(6):977–991, 2004.

[103] BI Epureanu, EH Dowell, and KC Hall. Reduced-order models of unsteady transonic viscous flows in turbomachinery. *Journal of Fluids and Structures*, 14(8):1215–1234, 2000.

[104] D. Xiao, F. Fang, A.G. Buchan, C.C. Pain, I.M. Navon, J. Du, and G. Hu. Non-linear model reduction for the navierstokes equations using residual deim method. *Journal of Computational Physics*, 263:1 – 18, 2014.

[105] D Xiao, P Yang, F Fang, J Xiang, CC Pain, and IM Navon. Non-intrusive reduced order modelling of fluid–structure interactions. *Computer Methods in Applied Mechanics and Engineering*, 303:35–54, 2016.

[106] S. Chaturantabut and D. Sorensen. Nonlinear model reduction via discrete empirical interpolation. *SIAM Journal on Scientific Computing*, 32(5):2737–2764, 2010.

[107] Gianluigi Rozza, Dinh Bao Phuong Huynh, and Anthony T Patera. Reduced basis approximation and a posteriori error estimation for affinely parametrized elliptic coercive partial differential equations. *Archives of Computational Methods in Engineering*, 15(3):1, 2007.

[108] Dumitru I. Caruntu and Israel Martinez. Reduced order model of parametric resonance of electrostatically actuated mems cantilever resonators. *International Journal of Non-Linear Mechanics*, 66:28 – 32, 2014. 4th Canadian Conference on Non-linear Solid Mechanics.

[109] Laura Ruzziconi, Ahmad M Bataineh, Mohammad I Younis, Weili Cui, and Stefano Lenci. Nonlinear dynamics of an electrically actuated imperfect microbeam resonator: experimental investigation and reduced-order modeling. *Journal of micromechanics and microengineering*, 23(7):075012, 2013.

[110] Laura Ruzziconi, Mohammad I Younis, and Stefano Lenci. An efficient reduced-order model to investigate the behavior of an imperfect microbeam under axial load and electric excitation. *Journal of Computational and Nonlinear Dynamics*, 8(1):011014, 2013.

[111] A Scardigli, R Arpa, A Chiarini, and H Telib. Enabling of large scale aerodynamic shape optimization through pod-based reduced-order modeling and free form deformation. In *Advances in Evolutionary and Deterministic Methods for Design, Optimization and Control in Engineering and Sciences*, pages 49–63. Springer, 2019.

[112] Andrea Lupini and Bogdan I Epureanu. A conditioning technique for projection-based reduced order models. *Computer Methods in Applied Mechanics and Engineering*, 349:251–265, 2019.

[113] B. J. Olson, S. W. Shaw, C. Z. Shi, C. Pierre, and R. G. Parker. Circulant matrices and their application to vibration analysis. *Applied Mechanics Reviews*, 66(4), 2014.

[114] Andrea Lupini and Bogdan I Epureanu. On the use of mesh morphing techniques in reduced order models for the structural dynamics of geometrically mistuned blisks. *Mechanical Systems and Signal Processing*, 127:262–275, 2019.

[115] S-T Wei and C Pierre. Localization phenomena in mistuned assemblies with cyclic symmetry part ii: Forced vibrations. *Journal of Vibration, Acoustics, Stress, and Reliability in Design*, 110(4):439–449, 1988.

[116] Matthias Hüls, Lars Panning-von Scheidt, and Jörg Wallaschek. Combined airfoil and snubber design optimization of turbine blades with respect to friction damping. *Journal of Turbomachinery*, 140(8):081007, 2018.

[117] Luca Pesaresi, Loic Salles, Adrian Jones, JS Green, and CW Schwingshackl. Modelling the nonlinear behaviour of an underplatform damper test rig for turbine applications. *Mechanical Systems and Signal Processing*, 85:662–679, 2017.

[118] Chiara Gastaldi and Muzio M Gola. Criteria for best performance of pre-optimized solid dampers. *Journal of Engineering for Gas Turbines and Power*, 141(4):042502, 2019.

[119] Christian Siewert, Lars Panning, Annika Schmidt-Fellner, and Andreas Kayser. The estimation of the contact stiffness for directly and indirectly coupled turbine blading. In *ASME Turbo Expo 2006: Power for Land, Sea, and Air*, pages 841–853. American Society of Mechanical Engineers, 2006.

[120] C. Gastaldi and M. M. Gola. A random sampling strategy for tuning contact parameters of underplatform dampers. *Proceedings of the Asme Turbo Expo: Turbine Technical Conference and Exposition, 2015, Vol 7b*, 2015.

[121] RS Jangid. Dynamic characteristics of structures with multiple tuned mass dampers. *Structural Engineering and Mechanics*, 3(5):497–509, 1995.

[122] Jose A Inaudi and James M Kelly. Mass damper using friction-dissipating devices. *Journal of Engineering Mechanics*, 121(1):142–149, 1995.

[123] Jos L. Almazn, Juan C. De la Llera, Jos A. Inaudi, Diego Lpez-Garca, and Luis E. Izquierdo. A bidirectional and homogeneous tuned mass damper: A new device for passive control of vibrations. *Engineering Structures*, 29(7):1548 – 1560, 2007.

[124] Zeng Gewei and Biswajit Basu. A study on friction-tuned mass damper: harmonic solution and statistical linearization. *Journal of Vibration and Control*, 17(5):721–731, 2011.

[125] O. Marinescu, B. I. Epureanu, and M. Banu. Reduced order models of mistuned cracked bladed disks. *Journal of Vibration and Acoustics-Transactions of the ASME*, 133(5), 2011.

[126] C. M. Firrone and S. Zucca. *Modelling Friction Contacts in Structural Dynamics and its Application to Turbine Bladed Disks*, chapter 14, pages 301–334. InTech, 2011.

[127] A. Cardona, T. Coune, A. Lerusse, and M. Geradin. A multiharmonic method for non-linear vibration analysis. *International Journal for Numerical Methods in Engineering*, 37(9):1593–1608, 1994.

[128] C. H. Menq, J. H. Griffin, and J. Bielak. The influence of microslip on vibratory response, part ii: A comparison with experimental results. *Journal of Sound and Vibration*, 107(2):295 – 307, 1986.

[129] Michael R Ross, Andrew Murphy, and Brian Stevens. Bolt modeling effects on fatigue predictions for mock hardware in a random vibration environment. In *AIAA Scitech 2019 Forum*, page 0490, 2019.

[130] Andrea Lupini, Mainak Mitra, and Bogdan I Epureanu. Application of tuned vibration absorber concept to blisk ring dampers: A nonlinear study. *Journal of Engineering for Gas Turbines and Power*, 141(10), 2019.

[131] Andrea Lupini, Justin Shim, and Bogdan Epureanu. An experimental and computational study on a tuned damper with frictional contact for rotor blade-like structures. In *AIAA Scitech Forum 2020*, 2020.

[132] Alok Sinha and JH Griffin. Friction damping of flutter in gas turbine engine airfoils. *Journal of Aircraft*, 20(4):372–376, 1983.

[133] Alok Sinha and JH Griffin. Effects of friction dampers on aerodynamically unstable rotor stages. *AIAA journal*, 23(2):262–270, 1985.

[134] Andrea Lupini and Bogdan I Epureanu. Max modeling of integrally bladed rotors with blends, mistuning, and prestress. In *8th European Conference for Aeronautics and Aerospace Sciences (EUCASS)*, 2019.

[135] Andrea Lupini and Bogdan I Epureanu. A friction-enhanced tuned ring damper for bladed disks. In *ASME Turbo Expo 2020: Turbine Technical Conference and Exposition*, pages GT2020–14815. ASME, 2020.